

# Plasma Enhanced Growth of GaN Single Crystalline Layers from Vapour Phase

Von der Fakultät für Mathematik,  
Naturwissenschaften und Informatik  
der Brandenburgischen Technischen Universität Cottbus-Senftenberg

zur Erlangung des akademischen Grades

Doktor der Naturwissenschaften

(Dr. rer. nat.)

genehmigte Dissertation

vorgelegt von

**MSc in Eng.**

**Radosław Piotr Zwierz**

geboren am 18.01.1985 in Racibórz, Polen

**Gutachter:** Prof. Dr. Holger Kersten

**Gutachter:** Prof. Dr. Jürgen Reif

**Gutachter:** apl. Prof. Dr. Dietmar Siche

Tag der mündlichen Prüfung: 7. Juli 2014

Cottbus 2014



”What is the point of being alive if you don’t at least try to do something remarkable?”

*John Green, An Abundance of Katherines*



## Abstract

Gallium nitride (GaN) is a III-V semiconductor, characterised by direct, wide band gap of 3.4 eV at RT. As a material of particular interest for opto- and power electronics applications, it has been thoroughly studied in recent years. Utilisation of GaN homoepitaxy in manufacturing of laser diodes (LDs), light-emitting diodes (LEDs), power devices, etc. would be beneficial in terms of reducing defect density, thus improving their lifetime and performance. Yet cost-effective process for providing native GaN substrates has not been established so far.

The focus of this work is put on development of a new method to grow single crystalline GaN layers from Ga vapour. Our approach exploits microwave (MW) plasma as a source of excited nitrogen species, in contrast to classical physical vapour transport (PVT)-based technique, in which ammonia ( $\text{NH}_3$ ) serves as a source of reactive nitrogen. Novelty of MW plasma enhanced growth of GaN from vapour lies in MW nitrogen plasma formation in the vicinity of the seed, at moderate pressure (200 – 800 mbar range), and concurrent physical vapour transport of Ga to the growth zone.

Simulations of the growth setup (HEpiGaN software) and of the MW plasma source (CST Microwave software) have followed the extensive investigations of material properties. The growth setup and the MW plasma source, with the resonance cavity being its crucial part, have been constructed and implemented into the existing growth reactor. The stability of MW plasma in function of temperature and pressure has been studied along with its influence on the seed temperature, and thus on the growth conditions. Furthermore, optical emission spectroscopy (OES) has been utilised for in-situ characterisation of the growth atmosphere. Studies on the interaction of Ga vapour with the nitrogen discharge were interpreted on the basis of the level structure of lower excited states of Ga.

Deposition experiments have been conducted, using sapphire seeds, GaN, AlN and AlGaIn templates, while GaN single crystalline layers have been grown on sapphire and

GaN templates. Characterisation of GaN layers have been done by various methods, i.e. structure of layers by scanning electron microscopy (SEM), their composition by energy-dispersive X-ray spectroscopy (EDX) and secondary ion mass spectrometry (SIMS), and crystal quality by high resolution X-ray diffraction (HRXRD). Results of the characterisation together with outcome of OES measurements revealed importance of carbon for the sub-atmospheric MW plasma enhanced growth of GaN from vapour. In addition, this fact was confirmed by experiments in the setup with reduced carbon content. Possible routes for GaN synthesis have been discussed, with the most probable being CN-assisted GaN formation. While CN was detected in the plasma spectra, there was no evidence for the existence of GaN molecules in vapour phase.

## Kurzfassung

Galliumnitrid (GaN) ist ein III-V-Halbleiter, der durch seine direkte, breite Bandlücke von 3.4 eV bei Raumtemperatur gekennzeichnet ist. Als Material von besonderem Interesse für Anwendungen in der Opto- und Leistungselektronik, wurde es in den letzten Jahren umfangreich untersucht. Die Verwendung der GaN-Homoepitaxie in der Herstellung von Laserdioden (LDs), Leuchtdioden (LEDs), Leistungsbau-elementen etc. wäre günstig bezüglich der Verringerung der Defektdichte, um ihre Lebensdauer und Leistung zu verbessern. Ein kostengünstiges Verfahren zur Bereitstellung von GaN-Eigen-substraten wurde jedoch bisher nicht etabliert.

Der Schwerpunkt dieser Arbeit ist die Entwicklung einer neuen Züchtungsmethode um einkristalline GaN-Schichten herzustellen. Unsere Vorgehensweise nutzt Mikrowellen (MW)-Plasma als Quelle angeregter Stickstoff-Spezies, im Gegensatz zu dem klassischen physikalischen Gasphasentransport (PVT) basierten Verfahren, in dem Ammoniak ( $\text{NH}_3$ ) als Quelle für reaktiven Stickstoff dient. Die Neuheit des MW-Plasmas gestützten Wachstums von GaN aus Gallium(Ga)-Dampf liegt in der MW-Plasmaerzeugung in der Nähe des Keims bei mittlerem Druck (200 - 800 mbar) und gleichzeitigen physikalischen Transport von Ga-Dampf in die Wachstumszone.

Den Simulationen des Aufbaus (HEpiGaN Software) und der MW-Plasmaquelle (CST Microwave Software) folgten die umfangreichen Untersuchungen der Materialeigenschaften. Der Aufbau und die MW-Plasmaquelle, die als wesentliche Komponente den Hohlraumresonator enthält, wurden konstruiert und in den vorhandenen Wachstumsreaktor implementiert. Die Stabilität des MW-Plasmas als Funktion von Temperatur und Druck wurde zugleich mit ihrem Einfluss auf die Keimtemperatur und damit auf die Wachstumsbedingungen untersucht. Außerdem wurde die Optische Emissionsspektrometrie (OES) zur in-situ Charakterisierung der Wachstums-Atmosphäre verwendet. Die Wechselwirkung des Ga-Dampfes mit der Stickstoffentladung wurde auf der Basis der Energieniveau-Struktur der unteren angeregten Ga-Zustände interpretiert.

Die Abscheidungs-Experimente wurden unter Verwendung von Saphir-Keimsubstraten, GaN-, AlN- und AlGaN-Templates durchgeführt. Die GaN-Schichten wurden auf Saphir-Keimsubstraten und auf GaN-Templates gewachsen und mit verschiedenen Methoden charakterisiert: die Struktur mit der Rasterelektronenmikroskopie (SEM), die Zusammensetzung mit der Energiedispersiven Röntgenspektroskopie (EDX) und der Sekundärionen-Massenspektrometrie (SIMS) und die Kristallqualität mit der hochauflösenden Röntgenstrukturanalyse (HRXRD). Die Ergebnisse der Charakterisierung zeigten zusammen mit den Resultaten der OES-Messungen die Bedeutung von Kohlenstoff für das MW-Plasma gestützte, subatmosphärische Wachstum von GaN aus der Gasphase. Zusätzlich wurden sie durch die Experimente im Aufbau mit reduziertem Kohlenstoffgehalt bestätigt. Mögliche Wege der GaN-Synthese wurden diskutiert, wobei die CN-unterstützte GaN-Bildung der wahrscheinlichste ist. Während CN in den Plasmaspektren nachgewiesen wurde, gab es keine Beweise für die Existenz von GaN-Molekülen in der Dampfphase.



# Contents

<b>1. Introduction</b>	<b>1</b>
1.1. Properties of GaN . . . . .	2
<b>2. Current status of GaN growth technology</b>	<b>5</b>
2.1. Review of relevant bulk growth techniques . . . . .	7
2.1.1. Solution growth . . . . .	7
2.1.2. Vapour phase growth . . . . .	11
2.2. GaN vapour growth in IKZ . . . . .	15
2.2.1. Physical vapour transport of Ga . . . . .	15
2.2.2. Chemical vapour transport of Ga . . . . .	18
2.3. Seeds and growth modes . . . . .	19
2.3.1. Seeds . . . . .	20
2.3.2. Growth modes . . . . .	21
<b>3. Nitrogen plasma</b>	<b>23</b>
3.1. Power absorption in the microwave field . . . . .	23
3.2. Plasma classification . . . . .	26
3.3. Excited states of nitrogen . . . . .	29
3.4. Optical emission spectroscopy . . . . .	30
3.4.1. Molecular spectra . . . . .	32
<b>4. Plasma enhanced methods for GaN growth</b>	<b>39</b>
4.1. Plasma assisted vapour epitaxy . . . . .	39
4.2. Plasma assisted solution growth . . . . .	43
4.3. Physical vapour transport with barrier discharge in IKZ . . . . .	45
<b>5. Experimental - MW plasma enhanced growth</b>	<b>49</b>
5.1. Outline of the system . . . . .	49
5.1.1. Growth setup . . . . .	51
5.1.2. MW plasma source . . . . .	58
5.2. Stability of MW plasma . . . . .	68
5.3. Advantages of nitrogen plasma over ammonia . . . . .	74
5.4. Study on Ga vapour . . . . .	76
5.4.1. Ga supply and super-saturation . . . . .	77
5.4.2. Plasma excitation of Ga vapour . . . . .	84
5.5. Deposition experiments as optimisation tool . . . . .	92
5.6. Growth of GaN single crystalline layers . . . . .	100
5.6.1. Experimental procedure . . . . .	100
5.6.2. Characterisation of GaN layers . . . . .	102

<b>6. Summary and Outlook</b>	<b>113</b>
<b>Appendices</b>	<b>xi</b>
<b>Appendix A. Material properties</b>	<b>xiii</b>
A.1. Ceramics . . . . .	xiii
A.2. Refractory metals . . . . .	xiv
<b>Appendix B. Calculations</b>	<b>xv</b>
B.1. Thermal expansion coefficient of Mo . . . . .	xv
B.2. Change of the cavity diameter . . . . .	xv
B.3. Resonance frequency shift - estimations . . . . .	xvi
<b>Appendix C. Experiments</b>	<b>xvii</b>
<b>Appendix D. Second positive system of N<sub>2</sub></b>	<b>xix</b>
<b>Bibliography</b>	<b>xxi</b>
<b>List of Figures</b>	<b>xxxix</b>
<b>List of Tables</b>	<b>xlvi</b>
<b>List of Symbols</b>	<b>xlvii</b>
<b>List of Abbreviations</b>	<b>li</b>
<b>Acknowledgements</b>	<b>lv</b>

# Chapter 1

## Introduction

In recent years GaN has slipped unnoticed through the back doors of our houses, being a key part of many contemporary electronic and optoelectronic devices. Although GaN has not such a strong position in conventional wisdom as silicon, yet its impact on people's life has been increasing (indoor and outdoor LED-based lighting systems, blue LDs in Blu-ray technology, high-voltage switching devices for power grids, etc.). GaN way from research laboratories to households is marked by series of technological breakthroughs: 1969 - growth of the first GaN single crystalline layer [1], 1971 - the first GaN LED [2], the achievement of p-doping in GaN [3], 1995 - the first blue InGaN/GaN double heterostructure LEDs [4], 1999 - the first commercially available violet InGaN-based LD [5], 2006 - the first Blu-Ray ROM players released by Samsung (BD-P100) [6] and Sony (BDP-S1) [7].

GaN properties (see Table 1) have been exploited mainly in solid state lightning and high power/high frequency electronics. The (Al,Ga,In) N-based materials system covers the entire visible range, with the direct band gap spanning from 0.69 eV (InN), through 3.4 eV (GaN) to 6.2 eV (AlN) (see Fig. 1.1). GaN based LEDs and LDs take advantage of much brighter emission characteristics than gallium arsenide (GaAs) and gallium phosphide (GaP). Owing to the wide band gap, high break-down voltage, large critical electric field, and high thermal conductivity, GaN devices can operate at high voltages and high switching frequency. Therefore, inverters, RF devices, power supply modules, and motor drives are at present the major power electronic application fields of GaN.

One of the main limiting factors for GaN technology is absence of well-established and cost-efficient technique of GaN bulk growth. The initial goal of this research was to study the possibility of GaN bulk single crystal growth from the vapour phase at moderate pressure (200 - 800 mbar), exploiting MW nitrogen plasma source implemented in the

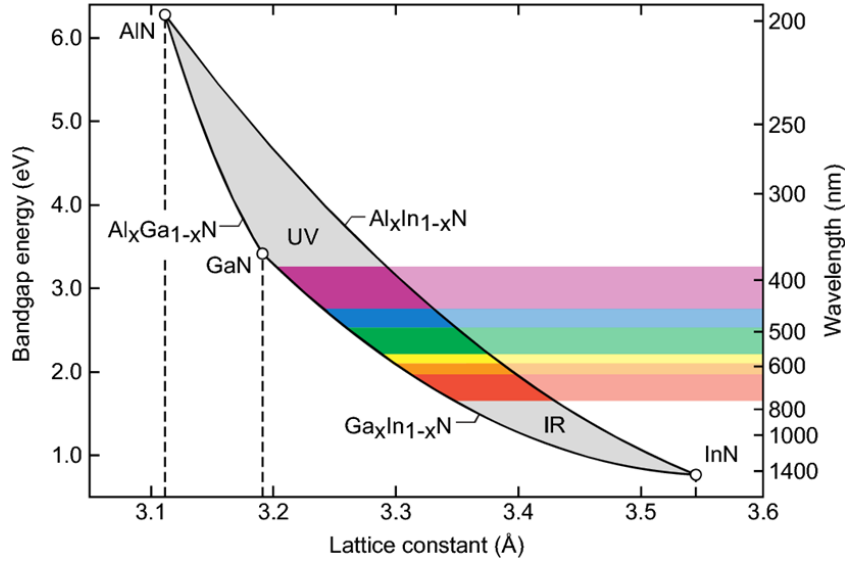


Figure 1.1.: Band gap energy in the function of lattice constant. III-nitrides at RT [8]

growth region.

## 1.1. Properties of GaN

Unique properties of GaN (see Table 1) derive from its crystal structure. GaN has either meta stable zinc blende (cubic) or thermodynamically stable wurtzite (hexagonal) crystal structure (Fig. 1.2). This work is focused only on the latter one, though. Wurtzite lattice constants  $a$  and  $c$  have relation as  $c/a = \sqrt{8/3} = 1.633$  and internal parameter  $u = 3/8 = 0.375$ , where  $b = u \times c$  corresponds to the anion-cation bond length.

Each hexagonal unit cell of GaN wurtzite crystal structure (space group  $P6_3mc$ ) consists of two interpenetrating hexagonal close-packed (hcp) sublattices. Each of them is composed of either Ga or N atoms, in tetrahedral nearest-neighbour atomic coordination. GaN exhibits mixed ionic-covalent bonding, whereas its high ionicity results in high bond strength of 9.12 eV/molecule. Spontaneous polarization  $P_{SP}$  along the  $c$ -axis is induced by an intrinsic asymmetry in the wurtzite structure. Furthermore, mechanical stress imposed by heteroepitaxial growth of GaN layer generates piezoelectric polarization  $P_{PZ}$ . Due to  $P_{SP}$  and  $P_{PZ}$ , there is a built-in electrostatic field in

Table 1.: Properties of wurtzite GaN [9]

Property	Value
Lattice constants	$a = 3.189 \text{ \AA}, c = 5.186 \text{ \AA}$
Molar mass	$83.73 \text{ g mol}^{-1}$
Density	$6.15 \text{ g cm}^{-3}$
Melting point	$2225 \text{ }^\circ\text{C}$ at $p > 6 \text{ GPa}$ [10]
Thermal expansion coefficients	$\alpha_{ort} = \alpha_c = 3.17 \times 10^{-6} \text{ K}^{-1}$ $\alpha_{  } = \alpha_a = 5.59 \times 10^{-6} \text{ K}^{-1}$
Thermal conductivity	$1.3 \text{ W cm}^{-1} \text{ }^\circ\text{C}^{-1}$
Specific heat	$0.49 \text{ J g}^{-1} \text{ }^\circ\text{C}^{-1}$
Band gap	$3.47 \text{ eV}$
Breakdown field	$3.3 \times 10^6 \text{ V cm}^{-1}$
Dielectric constants	8.9 (static), 5.35 (high frequency)
Refractive index	$n = 2.29$

the [0001] direction, which is not favourable for optoelectronic devices (shift of emission peak and reduction of emission efficiency). Therefore semi-polar r-plane ( $1\bar{1}02$ ), planes ( $10\bar{1}1$ ), ( $10\bar{1}2$ ), ( $10\bar{1}3$ ), ( $20\bar{2}1$ ), ( $11\bar{2}2$ ) and non-polar a-plane ( $11\bar{2}0$ ), and m-plane ( $1\bar{1}00$ ) have been used for growth of GaN-based LEDs and LDs.

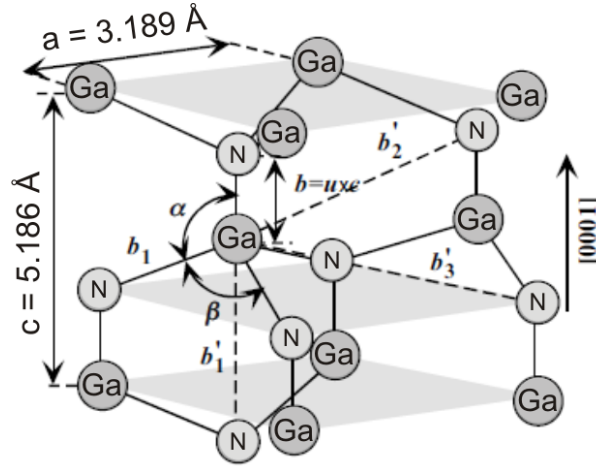


Figure 1.2.: Ideal wurtzite GaN structure:  $a$  and  $c$  - lattice constants,  $b$  - bond length,  $\alpha = \beta = 109.47^\circ$  - bond angles,  $b'_1, b'_2, b'_3$  - three types of second nearest neighbour distances. Adapted from [11]

The present work deals with the development of a novel method to grow GaN single crystalline layers from vapour, using MW nitrogen plasma at moderate pressure (200 -

800 mbar). Chapter 2 is intended to give an overview of the contemporary GaN technology, including relevant bulk growth methods and techniques used in Leibniz Institute for Crystal Growth in Berlin (IKZ) to synthesize GaN. In Chapter 3 nitrogen plasma along with optical emission spectroscopy (OES) is described. Chapter 4 is meant to present techniques that utilize nitrogen plasma for GaN growth. Description of the growth setup developed in our research group and studies on MW plasma enhanced growth of GaN at moderate pressure (200 - 800 mbar) are to be found in Chapter 5. It is accompanied by the outcome of characterisation of grown GaN single crystalline layers and discussion on plausible growth mechanism.

# Chapter 2

## Current status of GaN growth technology

The following chapter discusses the actual state of the art in the GaN growth technology. In Section 2.1 focus is put on the relevant GaN bulk growth techniques from solution (high nitrogen pressure solution growth, flux, ammonothermal) and vapour phase alike (physical vapour phase based process, sublimation sandwich technique, halide vapour phase epitaxy). Section 2.2 presents the activities of the author's group in the field of GaN synthesis from vapour, introducing the concept of pseudohalide transport of Ga. Selected materials employed as seeds in the GaN growth are presented in the last Section 2.3, along with the overview of the epitaxial growth modes.

It has been more than forty years, since M.P. Maruska reported in 1969 [1] growth of first single-crystalline GaN, appropriate for determining its direct energy band gap from optical and electrical characterisation. Despite long history of research and development on GaN and undisputable progress made in this area, a manufacturing technology for GaN bulk crystals has not been established by now. Utsumi et al. [10] showed experimentally that GaN melts congruently at pressures above 6.0 GPa at 2225 °C. Due to the extreme melting conditions, bulk GaN from melt is technically unfavourable and could not have been practically realized so far. Figure 2.1 presents the equilibrium curve for GaN, obtained by Karpinski et al. in 1984 [12].

In recent years, several different growth methods have been employed, in the search of the one that could provide GaN bulk single crystals commercially: physical vapour transport (PVT) [13, 14], halide vapour phase epitaxy (HVPE) [15], high pressure solution growth (HPSG) [16], Na-flux [17] and ammonothermal method [18, 19]. Currently,

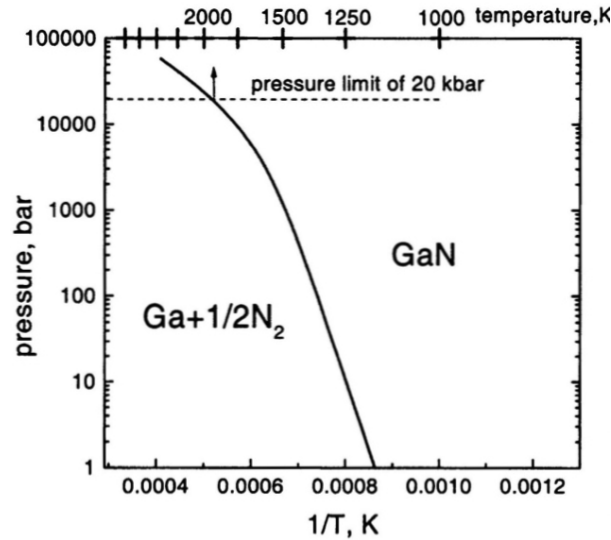


Figure 2.1.: Equilibrium curve for GaN [12]

growth from solutions [17, 18, 19] is under development for native substrates and ammono-thermal growth [18, 19] seems to have a high potential to meet the demand for “true bulk single crystals”. Due to growth rates of about 100  $\mu\text{m}/\text{h}$  HVPE is nowadays a very well established method to prepare free standing thick GaN layers, to be employed as substrates. Limited growth time due to ammonium chloride ( $\text{NH}_4\text{Cl}$ ) formation and relatively high dislocation density are the main drawbacks of this approach. Plasma-assisted synthesis of GaN has been subsequently drawing an attention of the scientific community. Replacing  $\text{NH}_3$  by nitrogen plasma as a source of reactive nitrogen, presents numerous advantages, such as: elimination of a dangerous, poisonous gas from the reaction chamber and lowering of the reaction temperature. Although, plasma enhanced methods have been successful in thin film GaN growth, they have not become an answer for a growing demand for GaN substrates so far. Ozawa et al. [20] reported 3  $\mu\text{m}$  GaN layers on sapphire, grown by solution growth with the assistance of 2.45 GHz microwave excited nitrogen plasma. Plasma-assisted molecular beam epitaxy (PAMBE) proved its reliability in terms of GaN and other III-nitrides layers, taking advantage of a remote nitrogen radio frequency (RF) plasma source. Recently Novikov and Foxon [21] presented a novel approach for the growth of GaN layers, combining liquid phase electroepitaxy



system with a PAMBE into plasma-assisted electroepitaxy (PAEE). The latter seems exotic and limited to very slow growth rates, though.

## 2.1. Review of relevant bulk growth techniques

### 2.1.1. Solution growth

HPSG, Na-flux and ammonothermal method constitute group of crystal growth techniques from solution. The basic principle for solution growth methods is the same. Material to be grown (solute) is dissolved in an appropriate solvent, super-saturation is induced by thermal gradient, controlled cooling down or solvent evaporation and eventually crystals are deposited on the seed.

#### High Pressure Solution Growth (HPSG)

HPSG is the oldest one among GaN growth methods from solution. It was proposed by Porowski [22], specifically to grow GaN crystals from supersaturated solution of nitrogen in molten Ga. Experiments are carried out in the high-pressure-high-temperature chamber, near thermal equilibrium, thus resulting in the lowest dislocation density reported for GaN bulk. By applying the temperature difference  $\Delta T$  along the boron nitride crucible, supersaturation in the growth solution is achieved. Nitrogen dissolved in the hotter part of the solution is transported by diffusion and convection to its colder part, where crystal growth takes place. The high pressure solution growth process can be described by the synthesis solute diffusion (SSD) mechanism, discussed elsewhere [23]. Either pure liquid Ga or Ga alloyed with 0.2 – 0.5 at% of Mg to reduce the concentration of free electrons is used. Typical growth conditions are in the range of  $p = 8 - 10$  kbar,  $T = 1400 - 1500$  °C,  $\Delta T = 40 - 50$  °C, duration of process without an intentional seeding is between 80 - 150 h. Dimensions of the spontaneously nucleated hexagonal platelets (up to 3 cm in diameter) or needles (length up to 1 cm) are limited by the size of crucible and available volume of supersaturated solution. The main advantage of HPSG GaN is its extreme low dislocation density, lower than  $100 \text{ cm}^{-2}$  [24]. In multi feed-seed configuration the

re-growth procedure of HVPE seeds was implemented to obtain crystallographically flat HPSG GaN substrates of higher structural quality, but with lower purity [25].

### **Ammonothermal**

For the time being, method that provides GaN bulk crystals of the best crystalline quality is the ammonothermal one. Epi-ready substrates prepared from AMMONO's GaN bulk crystals exhibit the 16 arc sec FWHM of X-ray rocking curve, measured for c-plane orientation (0001), for non-polar m-plane (1010) and semi-polar (2021) as well [26]. Principle of the ammonothermal method is dissolution of polycrystalline GaN in supercritical ammonia followed by its recrystallization on native seeds. With a view to increase solubility of GaN in ammonia, appropriate mineralisers are added to the solution. There are two different environments used: ammonobasic (Fig. 2.2(a)), developed by AMMONO S.A. and taking advantage of  $\text{NH}_2^-$  ions in the solution (alkali metals or their amides work as mineralisers:  $\text{LiNH}_2$ ,  $\text{NaNH}_2$ ,  $\text{KNH}_2$  or  $\text{NaNH}_2+\text{NaI}$ ) [26, 27] or ammonoacidic (Fig. 2.2(b)), introducing  $\text{NH}_4^+$  ions (supplied by halide compounds:  $\text{NH}_4\text{Cl}$ ,  $\text{NH}_4\text{Br}$ ,  $\text{NH}_4\text{I}$ ) [27, 28, 29].

High-pressure autoclave comprises two main temperature zones T1 and T2, so that  $T_2 > T_1$ . The near-isothermal conditions in each zone are provided by a baffle installed in between. The growth configuration (the position of feedstock basket and GaN native seeds) depends on the applied environment and on the temperature of the solution. In the ammonobasic solution and in the high temperature ammonoacidic solution [31] GaN has retrograde solubility, thus its solubility decreases with temperature (Fig. 2.2(a)). Extreme growth conditions (T in the range 500 – 600 °C and p around 0.1 - 0.3 GPa in case of the ammonobasic method [26]) pose challenges for the selection of appropriate autoclave materials. The physical properties of the nickel-based superalloy have been a significant limiting factor for the growth rates (around 2  $\mu\text{m}/\text{h}$ ) in the ammonothermal technique. Ehrentraut et al. [32] proposed high-temperature resistant ceramics as an inner shell, thus allowing for use steel instead of expensive nickel-based superalloy. GaN single crystals grown under 750 °C and 600 MPa in the SCoRA™ reactor have been

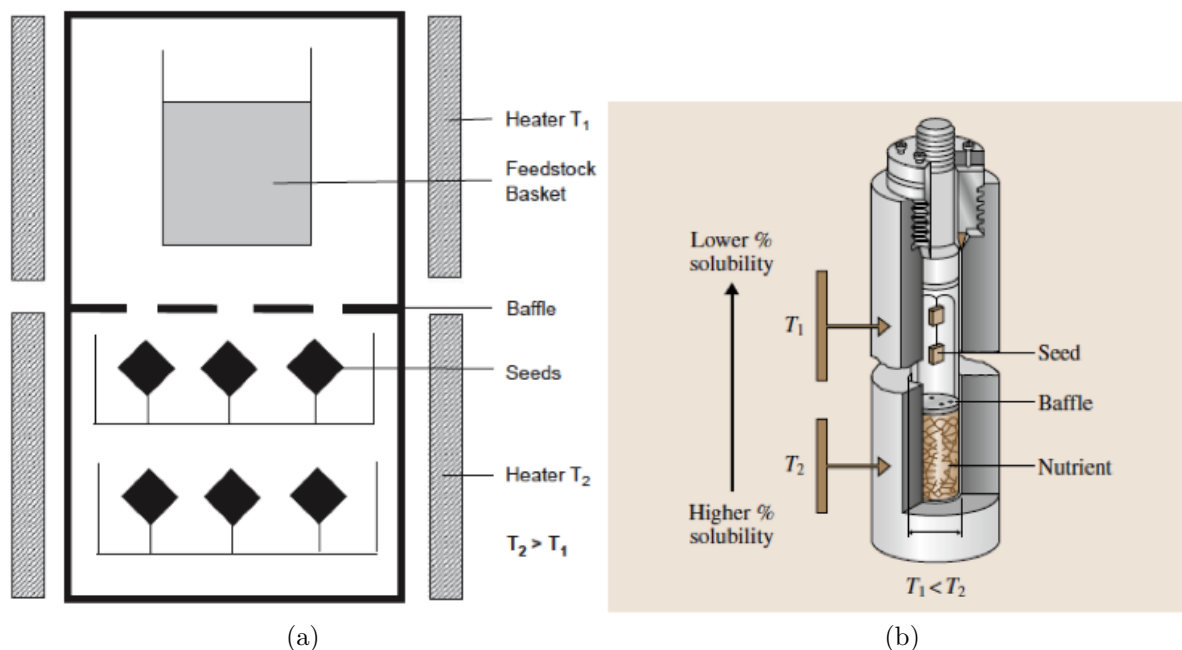


Figure 2.2.: Ammonobasic [30] (a) and ammonoacidic [27] (b) growth setups

demonstrated, with typical growth rates in the range of 10 - 30  $\mu\text{m}/\text{h}$ . Mitsubishi Corporation together with its partners developed a corrosion-resistant autoclave SCAAT<sup>TM</sup>, enabling growth of GaN in acidic environment at high  $p$  and  $T$  of  $\sim 0.1$  GPa and  $\sim 500$   $^{\circ}\text{C}$ , respectively. Process data disclosed by Mikawa [19] includes the growth rates in the range of 20  $\mu\text{m}/\text{h}$  and FWHM of the x-ray rocking curves on the grown  $m$ -plane GaN lower than 20 arcsec. Currently on the market, there are semi-insulating polar substrates up to 1.5 inch,  $n$ -type polar substrates up to 1 inch,  $n$ -type semi-polar ( $20\bar{2}1$ ) substrates 10 x 10 mm and  $n$ -type non-polar ( $10\bar{1}0$ ) substrates available from AMMONO S.A. [33].

### Na-Flux

The first one to report utilisation of Na flux method to grow GaN single crystals was Yamane et al. [34]. Solvent consisted initially of  $\text{NaN}_3$  and Ga only, however due to thermal decomposition of  $\text{NaN}_3$  at 300  $^{\circ}\text{C}$ , Na and  $\text{N}_2$  were obtained during the following reaction



Mixture of  $\text{NaN}_3$  and Ga was encapsulated in a stainless-steel tube container. By applying to it the temperature in the range of 600 – 800 °C and then cooling it down to room temperature, GaN crystals of 0.5 mm size were grown in 24 h process.

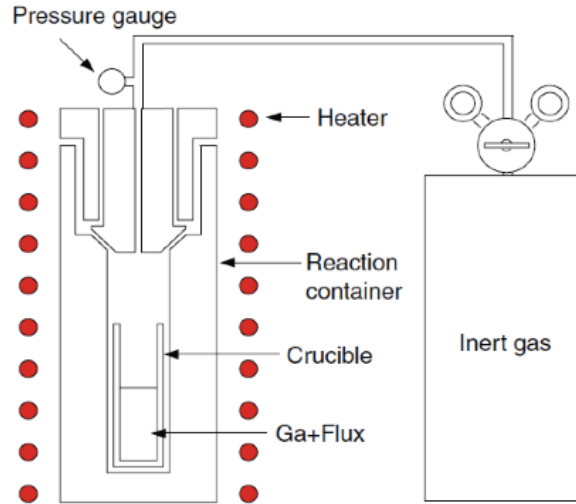


Figure 2.3.: Na flux growth setup [35]

Figure 2.3 depicts a typical Na flux growth system of GaN used at present times. Worthy to notice are two separate sources of Na and  $\text{N}_2$  in contrary to single one in form of  $\text{NaN}_3$  used in [34] and crucible made of boron nitride (BN).

As shown in Figure 2.4, Na catalyses the reaction between  $\text{N}_2$  and Ga in the Na-Ga melt by the following mechanism [36]: electrons released by Na are received by  $\text{N}_2$  molecule, weaken its bonding and lead to dissociation of  $\text{N}_2$  into negatively charged N atoms ( $\text{N}^{*-}$ ). Finally, the only elements in mixture that can form a nitride are Ga atoms.

Studies of Mori group (Osaka, Japan) revealed that adding carbon to Ga-Na melt can improve the growth rate by one order of magnitude, up to about 20  $\mu\text{m}/\text{h}$ . The unfavourable growth of polycrystalline GaN, which tends to dominate at higher nitrogen pressure, is suppressed [37]. It was shown that addition of Ca to Ga-Na melt improves transparency of the grown GaN crystals [35], while both Ca and Li increase the solubility

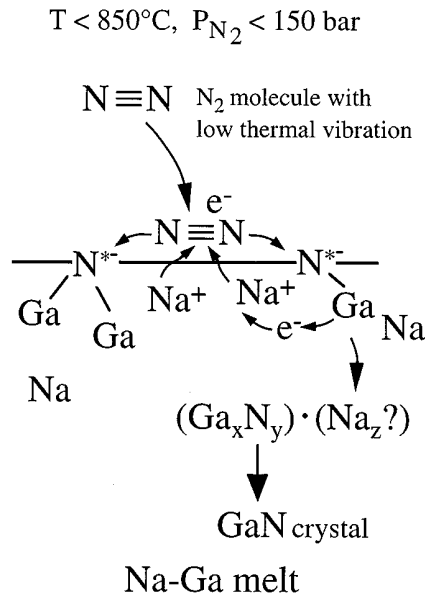


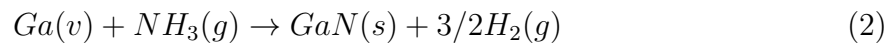
Figure 2.4.: The reaction between  $\text{N}_2$  and Ga, catalyst action of Na [36]

of nitrogen in the Ga-Na solution [17]. Recently 3 inch diameter GaN crystals on HVPE GaN substrate were reported [17]. After polishing it to the thickness of  $750 \mu\text{m}$ , optical absorption coefficient was estimated to be  $0.27 \text{ cm}^{-1}$ , whereas incorporated oxygen concentration was measured by SIMS to be at  $3 \times 10^{16} \text{ cm}^{-3}$ . Growth on small seeds resulted in pyramidal GaN bulk crystals of size of 15 - 20 mm. Simplicity of Na flux growth system is prevailed by a moderate growth rate of around  $20 \mu\text{m/h}$  and solvent contamination. Li-based flux method has lead to hexagonal GaN platelets with a size of 1 - 4 mm [38].

## 2.1.2. Vapour phase growth

### Physical Vapour Transport (PVT)

One of the oldest approaches to the vapour phase growth of GaN is defined by the following reaction:



Liquid Ga in the source is heated up to 1400 °C, while growth takes place at temperatures up to 1200 °C, within sub-atmospheric (200 – 800 mbar) or atmospheric pressure under N<sub>2</sub> atmosphere. Applicability of this method to grow polycrystalline GaN was presented already by Johnson et al. in 1932 [39]. Over the following years, several researchers succeeded in a single crystal GaN growth by improving the above described technique. It has been limited to low growth rates, though [40]. In case of unseeded growth, the size of crystals did not exceed few mm [41, 42]. When instead of liquid Ga pre-synthesized GaN powder is used, one speaks about incongruent sublimation of GaN [13]. GaN powder is usually heated (1100 – 1200 °C) either in an NH<sub>3</sub> flow [43] or under NH<sub>3</sub> atmosphere [44]. In spite of high growth rates of around 0.5 mm/h [42], the limitation remains the need for continuous supply of pre-synthesized GaN powder. Stability of GaN powder is the essential issue, reported for instance by Schoonmaker et al. [45]. Due to an incongruent sublimation, excess of Ga remains in the crucible and autocatalytic enhances the incongruent sublimation. As a result, after few hours there is only Ga left in the crucible [46].

### **Sublimation Sandwich Method (SSM)**

Wetzel [47], Fischer [48] and Vodakov [49] reported a modified PVT technique for GaN growth, denoted as sublimation sandwich method (SSM). The main concept of SSM is to place the substrate in front of the Ga source, within the distance of few millimetres. Such a small gap resulted in the increased mass transport of Ga vapour, thus in the high growth rates up to 1 mm/h [49]. On the other hand it limits dimensions of the grown crystal. Ammonia gas flow served as a source of reactive nitrogen, while supersaturation was achieved by temperature gradient applied between the source and the substrate. Single crystalline GaN layers on 6H-SiC with FWHM value of 420 arcsec, grown at 1240 °C were reported [48]. Kurai et al. [50] presented 30 - 70 µm thick GaN layers grown on sapphire.

## Halide Vapour Phase Epitaxy (HVPE)

Halide vapour phase epitaxy (HVPE) wins outright with other methods, when it comes to the growth rate of GaN. Values up to 300  $\mu\text{m}/\text{h}$  were reported [15], approximately 15 times higher than those for Na-flux technique and 10 times higher than for HT ammonothermal method. However, high crystal quality is limited to lower values of about 100  $\mu\text{m}/\text{h}$ . On the other hand,  $\text{NH}_4\text{Cl}$  by-product formation, high dislocation density due to heteroepitaxial growth and large gas consumption are among main drawbacks of HVPE [27, 51]. It was the HVPE method, which allowed in 1969 for growth of first, single-crystalline GaN on sapphire [1]. Since then, HVPE has grown into the significant, yet substitute and temporary technique for GaN bulk growth and GaN substrate preparation. Nowadays several groups all around the world work on development and improvement of HVPE for manufacture of high-quality GaN templates. Growth of GaN on Si [52, 53] or combination of HVPE with other growth techniques [54], for instance ammonothermal one, might partially satisfy the increasing demand for the low defect density GaN substrates at a moderate price. Recently a novel approach to produce free-standing GaN on Si substrate using HVPE has been reported by Samsung Electronics Co., Ltd. [55]. By applying high-temperature in-situ removal of Si substrate (etched by HCl at about 1000  $^\circ\text{C}$ ), fabrication of the high crystal quality ( $\text{EPD} < 1 \times 10^6 \text{ cm}^{-2}$ ) free-standing GaN over 8 inches in diameter is said to be profitable from economical and technological point of view.

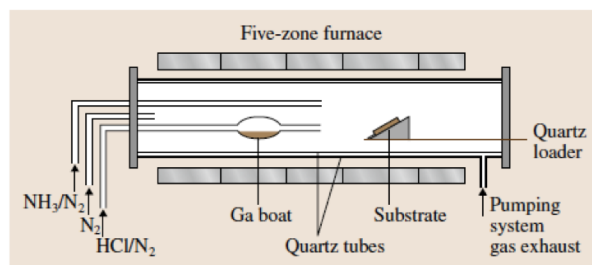
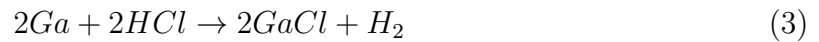


Figure 2.5.: HVPE growth setup [27]

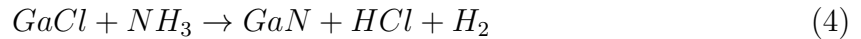
## 2. Current status of GaN growth technology

---

Scheme of the horizontal HVPE setup is depicted in Figure 2.5. It typically consists of quartz reactor (nowadays the vertical configuration is preferred), heated by multi-zone furnace or radio frequency heater. Separate quartz lines supply halide and hydride precursors, as well as a carrier gas: N<sub>2</sub>, H<sub>2</sub>, He, Ar or their mixtures. In the low-temperature zone (800 - 900 °C) halides are formed by flowing high purity HCl gas over a boat with liquid Ga



Subsequently, the vapour phase, including the chloride precursor GaCl and the hydride precursor NH<sub>3</sub>, is transported by a carrier gas to the deposition zone. Usual temperature of the substrate for GaN growth is at about 1050 °C and the reaction proceeds in the following way



In order to minimize parasitic growth, gallium chloride (GaCl) and NH<sub>3</sub> should not come into contact with each other, before reaching the growth region. [27, 51]

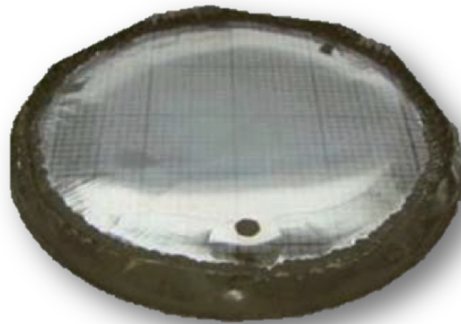


Figure 2.6.: GaN bulk crystal grown by HVPE [56]

So far, the best results of HVPE bulk-like growth were reported by groups from Japan [56] and Germany [15]. They succeeded in preparing ~6 mm thick GaN boules (see



Figure 2.6), starting from MOCVD GaN/sapphire template. Such GaN crystals could be possibly exploited to produce GaN wafers of high quality. However, this intermediate technology has not reached its maturity and thus can not be used on industrial scale. Therefore, the typical approach to prepare HVPE GaN free standing substrate is still a growth of a thick GaN layer on a foreign substrate followed by its separation. By using this so called wafer-by-wafer technology, GaN substrates up to 6 inches can be prepared [15, 57].

## 2.2. GaN vapour growth in IKZ

### 2.2.1. Physical vapour transport of Ga

Investigations on PVT-based synthesis of GaN were carried out in an inductively heated reactor (Fig. 2.7).

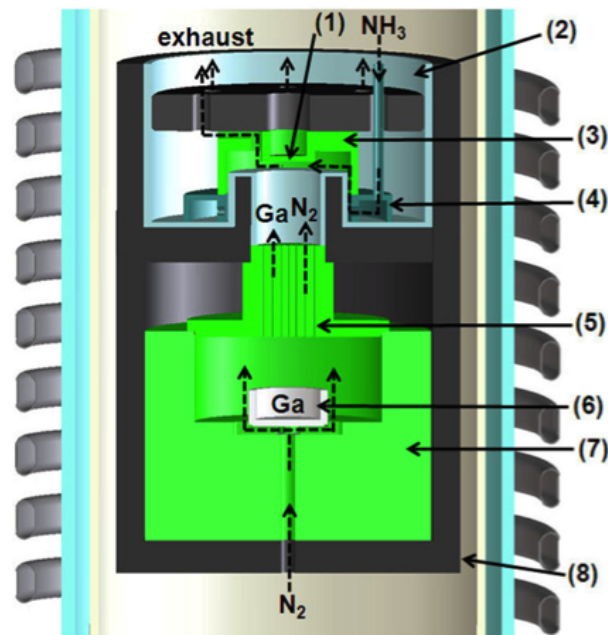


Figure 2.7.: Scheme of the inductively heated reactor: (1) – position of seed, (2) – quartz vessel, (3) – seed-holder, (4) – ring shower, (5) – diaphragm, (6) – source crucible, (7) – graphite susceptor, (8) – graphite isolation felt [58]

Two components necessary in a classical PVT method for GaN growth, elemental Ga

## 2. Current status of GaN growth technology

---

and reactive nitrogen, came from liquid Ga source and gaseous ammonia, respectively. Experiments without seeds lead to a spontaneous nucleation of millimetre-size GaN crystals, which were found on the seed-holder after 10 h growth with growth rates up to 50  $\mu\text{m}/\text{h}$ . Growth on 1  $\mu\text{m}$  MOCVD GaN on (0001) sapphire templates at a moderate temperature difference ( $\Delta T \leq 200$  K) between the Ga source and the seed resulted in not completely coalesced 280  $\mu\text{m}$  thick layers, with significant carbon incorporation [46]. In order to diminish the carbon contamination, graphite crucible, susceptor, diaphragm and top isolation were covered with pyrolytic boron nitride (pBN) layers. As the outcome, share of the chemical transport of Ga was decreased and simultaneously the growth rate dropped from 50 - 60  $\mu\text{m}/\text{h}$  to 5 - 10  $\mu\text{m}/\text{h}$  [14]. To compensate this effect, increase of the Ga source temperature was proposed, thus increasing enhancing physical transport of elemental Ga to the growth region (compare Fig. 2.8).

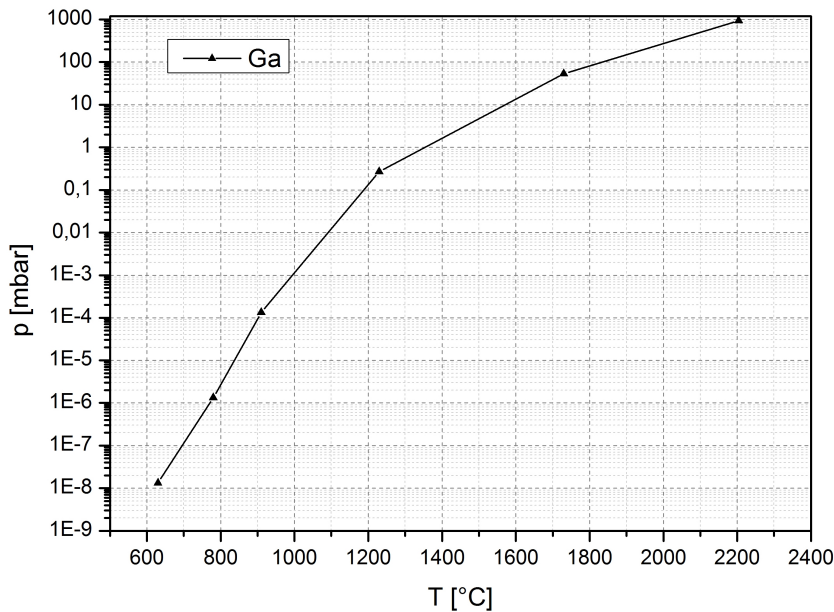


Figure 2.8.: Vapour pressure of Ga in function of temperature [59]

Temperature of the liquid Ga source was therefore kept above 1400  $^{\circ}\text{C}$ . Additional parameter used for control of Ga transport was  $\text{N}_2$  carrier gas flow (100 - 200 sccm) from the inlet located in the lower part of the growth reactor, below the Ga crucible. Typical  $\text{NH}_3$  flow was within 100 – 400 sccm range and 4 h growth experiments on 1  $\mu\text{m}$

MOCVD–GaN on sapphire templates at 1100 °C were conducted. The total pressure was varied between 200 and 800 mbar. Under above described conditions only polycrystalline GaN was found on the seed (Fig. 2.9).

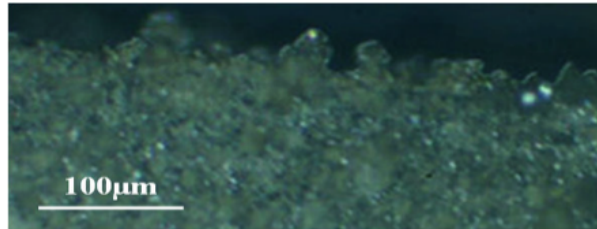


Figure 2.9.: Polycrystalline GaN layer on the seed [60]

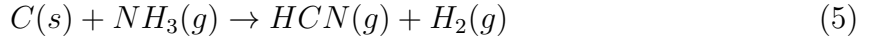
The polycrystalline growth was associated to the high temperature difference ( $\sim 300$  K) between the seed and the source, which caused supercritical supercooling of the Ga vapour resulting in formation of Ga droplets. High temperature differences in PVT growth of GaN emerge from contradictory temperature prerequisites. As it was already mentioned, at the Ga source side temperatures around 1400 °C are required for providing sufficient amount of gaseous Ga. At the growth side, temperatures exceeding 1100 °C are not favourable, due to enhanced early ammonia pyrolysis, with  $H_2$  being one of its products. This in turn not only limits the nitridation of Ga vapour, but also can lead to decomposition of GaN template and already grown layer. As it was shown by R.C. Schoonmaker et al. [45], GaN thermal decomposition of GaN polycrystalline powder starts at 900 °C. Degradation of structural and morphological properties of GaN on sapphire template, heated above 900 °C, was reported by Choi et al. [61]. Efficient supply of reactive nitrogen is able to prevent this process and enable growth of GaN in the metastable region. The lower limitation for the growth temperature originates from the growth kinetics. Temperature, at which the kinetic rate of arrival at each surface (diffusion and sticking) site is equal to the rate of removal by surface diffusion and desorption, has been considered as the minimum growth temperature. Dryburgh [62] calculated it for GaN growth under atmospheric pressure to equal  $\approx 900$  °C.

Temperature of the seed is also limited by the use of quartz parts in its vicinity (vessel, ring shower). The main benefit of  $NH_3$  transport by quartz tubes is that it minimizes

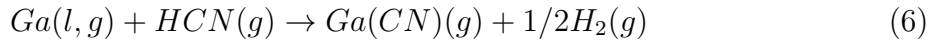
pyrolysis of NH<sub>3</sub>, which starts already at 500 °C.

### 2.2.2. Chemical vapour transport of Ga

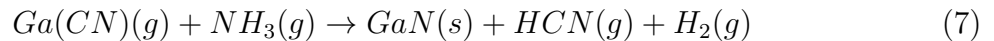
In the concurrent presence of graphite parts and ammonia in the reactor, chemistry of GaN growth process is profoundly changed. Pure physical transport of Ga is supported then by the chemical vapour transport, triggered by the reaction of NH<sub>3</sub> with carbon. It is known that NH<sub>3</sub> interacts with carbon at elevated temperatures [63, 64]. Jacobs et al. [14] proposed hydrogen cyanide (HCN) being the dominant product of this process



HCN was later detected by IR spectroscopy in the waste gas and is expected to act analogously to hydrogen chloride (HCl) in the HVPE [1], forming a volatile gallium compound (Eq. 6). While in the HVPE Ga is carried by GaCl, pseudohalide vapour growth relies on the transport of Ga to the deposition region by means of Ga(CN)(g), being supported by the carrier nitrogen gas.



Formation of GaN can proceed via a subsequent reaction of Ga(CN)(g) with NH<sub>3</sub>, which is the most favourable path from thermodynamic point of view at temperatures T > 950 °C.



In the experiments, utilizing pseudohalide vapour transport of GaCN from 1100 °C Ga melt, single crystalline GaN layers on 2 µm MOCVD–GaN on sapphire templates were grown (Fig. 2.10). Owing to a small temperature gradient (T<sub>seed</sub> = 1050 °C), Ga supercritical supersaturation was not an issue. Other important growth parameters were as follows: N<sub>2</sub> carrier gas flow of 100 sccm, NH<sub>3</sub> flow 100 - 400 sccm, growth time t<sub>g</sub>

typically 4 h with average growth rates of  $\sim 50 \mu\text{m/h}$ .

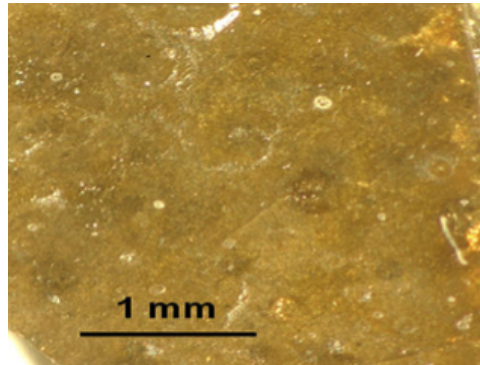


Figure 2.10.: CVT grown single crystalline GaN layer, 160  $\mu\text{m}$  thick with C inclusions [60]

Research on GaN growth by means of controlled cyanotransport is currently in progress in IKZ [65].

## 2.3. Seeds and growth modes

Seeds are of the utmost importance for the growth of high quality bulk GaN, thus homoepitaxial growth on GaN seed crystals is very promising. In spite of continuous development in the field, it was only recently when AMMONO S.A. introduced 1 inch GaN substrates on the market. Because of its high price and lack of bigger GaN wafers available, growth of GaN layers is carried out mostly on foreign substrates. There is a wide range of materials, employed as substrates for GaN growth, such as sapphire ( $\text{Al}_2\text{O}_3$ ),  $\text{Ga}_2\text{O}_3$ , AlN, SiC, GaAs, Si, MgO, ZnO,  $\text{TiO}_2$ ,  $\text{LiAlO}_2$  etc. [66]. This chapter discusses typical orientations, planes and step-cuts of chosen foreign substrates and templates used in GaN vapour phase growth techniques in our laboratory that is  $\text{Al}_2\text{O}_3$ , AlN,  $\text{Ga}_2\text{O}_3$  and GaN/ $\text{Al}_2\text{O}_3$  templates. Heteropitaxial growth of GaN entails several challenges, due to materials mismatch in terms of their lattice constants, thermal expansion coefficients, etc. Therefore, techniques like one- or two-step epitaxial layer overgrowth (1S-ELO, 2S-ELO), low temperature buffer layers, etc. were introduced to reduce the threading dislocation density of the GaN layers grown on the foreign substrates [27, 50]. They are

not itself a subject of this dissertation, though.

### 2.3.1. Seeds

#### **Al<sub>2</sub>O<sub>3</sub>**

Despite the large difference in lattice constant (around 16%) and mismatch with GaN thermal expansion coefficient ( $\alpha_{\parallel} = 5.59 \times 10^{-6}/K$  for GaN and  $7.50 \times 10^{-6}/K$  for sapphire [9, 67]), sapphire has been extensively used for GaN epitaxy. The prevailing arguments are its relatively low cost and access to 2 inch wafers. On a commonly exploited c-plane (0001) of sapphire, c-plane oriented GaN films are grown, with a 30° in-plane rotation. Since GaN has a built-in electrostatic field along the [0001] direction, growth on r-plane (1 $\bar{1}$ 02), a-plane (11 $\bar{2}$ 0), m-plane (10 $\bar{1}$ 0) have been performed as well, so to obtain a non-polar a-plane GaN, thus diminishing the negative influence of the electrostatic field on nitride-based optoelectronic devices. [27, 66] Improved morphology of GaN layers grown on a off-cut sapphire by both MOVPE and HVPE has been reported [68, 69]. The 0.3° c-plane off-orientation against the a-plane or the m-plane in case of HVPE leads to the reduction of hillocks [68]. T. Yuasa et al. [70] demonstrated that in case of the MOVPE, the smoothest surfaces result from the epitaxy on the 0.17° miscut sapphire. Improvement of the crystal quality of GaN on sapphire is realized by implementing such pre-treatment processes steps like plasma or NH<sub>3</sub> nitridation in HVPE [71], MOVPE [72] and MBE [73] or low-temperature-grown GaN buffer layer (LT-GaN) [74, 75]. In our experiments double side epi-ready sapphire from PB-Technik AG has been used for deposit observation.

#### **$\beta$ -Ga<sub>2</sub>O<sub>3</sub>**

Growth of wurtzite GaN on monoclinic (C2/m)  $\beta$ -Ga<sub>2</sub>O<sub>3</sub> is a challenging task. Nevertheless, the first epitaxial layers of GaN and the blue light-emitting diode, both grown on (100)  $\beta$ -Ga<sub>2</sub>O<sub>3</sub> by MOVPE, were demonstrated by K. Shimamura et al. [76]. By con-

trolling the nitridation conditions, GaN films on (100)  $\beta$ -Ga<sub>2</sub>O<sub>3</sub> were grown by means of radio frequency (RF)-MBE [77]. Kachel et al. [78] reported on thick GaN layer grown on (100)  $\beta$ -Ga<sub>2</sub>O<sub>3</sub> by the PHVPE, while low-temperature intermediate buffer layer was formed by an in-situ treatment of epi-ready  $\beta$ -Ga<sub>2</sub>O<sub>3</sub> substrate with NH<sub>3</sub>.

#### **GaN/Al<sub>2</sub>O<sub>3</sub> template**

GaN templates offer a possibility to start growth already on a thin GaN layer deposited epitaxially on a foreign substrate (mainly sapphire or silicon) by MOVPE or HVPE. In this way the initial nucleation process is facilitated. Currently there is a wide range of GaN templates with dislocation density around  $1 \times 10^8 \text{ cm}^{-2}$  available on the market, both on c- plane sapphire (n-type undoped, n-type Si doped, semi-insulating Fe-doped, p-type Mg doped) and (111) Si (n-type undoped) [79, 80, 81, 82]. Standard commercial GaN on sapphire templates (from University Ulm, IAF Freiburg and FBH Berlin) were utilized in our growth experiments.

#### **AlN**

AlN is an interesting alternative for GaN templates. High thermal stability of AlN (up to around 1800 °C [83]) allows for the increase of growth temperature. The main drawbacks are problems with polishing of AlN substrates and lattice mismatch to GaN that equals 2.5% [84]. The American company HexaTech manufactures single crystalline AlN wafers, which are mostly used as base for optoelectronic and high-power electronic devices, though [85]. AlN wafers are produced also in Leibniz Institute for Crystal Growth in Berlin (IKZ).

#### **2.3.2. Growth modes**

There are three main modes distinguished in the area of epitaxy, i.e. Frank-van der Merwe (FM, layer by layer), Stranski Krastanov (SK) and Volmer-Weber (VW) [86]. The occurrence of a certain epitaxial mode depends on the misfit between substrate and

epitaxial layer, and the thermodynamic driving force – minimization of the total free energy  $G$ , by changing the surface energy  $\Delta\gamma$ .

$$\Delta\gamma = \gamma_L + \gamma_i - \gamma_S \quad (8)$$

where:  $\gamma_S$  is the surface free energy of the substrate,  $\gamma_i$  is the free energy of the interface and the surface free energy of the layer is denoted as  $\gamma_L$ . When  $\Delta\gamma > 0$ , thus  $\gamma_S < \gamma_L + \gamma_i$ , then VW mode takes place. Formation of three dimensional (3D) islands or clusters is observed that is typical for GaN growth on sapphire [87]. Because of the large lattice mismatch and large  $\gamma_i$  between sapphire and GaN, random nucleation of islands all over the substrate is expected. Initial 3D mode can be transformed to 2D, thanks to the growth of LT GaN and subsequent annealing.

In spite of relatively smaller lattice mismatch between GaN and SiC (3.4%), direct growth of GaN on SiC follows the VW mode as well [88]. In case of  $\Delta\gamma \leq 0$ , hence  $\gamma_S \geq \gamma_L + \gamma_i$ , FM growth mechanism is observed, which is expected to result in flat layers of high structural perfection [86]. In heteroepitaxy, after exceeding a certain critical thickness of the growing film, layer-by-layer growth can switch to VW mode. This two-step SK mode is treated as an intermediate one between 2D and 3D mode, following FM mode in the initial phase and then continuing through the VW mode to release strain that comes from the lattice misfit. While considering the total energy change  $\Delta\gamma$  of thicker layers, an increase in specific free interface distortion energy  $E_d$  has to be taken into account.

For the first few layers:  $E_d \approx 0$ , hence  $\Delta\gamma \leq 0$  and  $\gamma_S \geq \gamma_L + \gamma_i + E_d$ , whereas for thicker films  $E_d > 0$ , thus  $\Delta\gamma > 0$  and  $\gamma_S < \gamma_L + \gamma_i + E_d$ . The controlled SK mode in strained-layer epitaxy is used to form GaN/ AlN quantum dots [89, 90, 91]. The structural properties of the epi-layers such as perfection, flatness and interface abruptness depends directly on the growth mode. Constant efforts of numerous researchers to govern the GaN growth mode resulted in techniques and approaches like: misorientated substrates to promote step-flow growth mode [92], AlN buffer layer [93, 3], deposition of LT GaN nucleation layer [94], thermal annealing of LT layer [95], etc.



# Chapter 3

## Nitrogen plasma

Plasma is a particle system containing free charged particles that move in random directions. On the average plasma is macroscopically neutral, albeit locally charged. Quasineutrality of plasma means that total density of electrons and negative ions nearly equals density of positive ions. Plasmas have been often denoted as the fourth state of matter, ever since this term was coined by W.Crookes in 1897 [96]. The fact is that they constitute most of the visible matter in our universe. [97] The following chapter discusses prerequisites for breakdown of gases in the microwave (MW) field and further interaction of plasma with incoming electromagnetic (EM) energy (Section 3.1). Subsequently, some fundamental classifications of plasma along with its chosen basic parameters are presented (Section 3.2). In Section 3.3 excited states of nitrogen in nitrogen plasma are discussed, whereas Section 3.4 is devoted to application of optical emission spectroscopy (OES) in plasma characterisation. It is intended to show OES assistance in understanding processes taking place during microwave plasma enhanced vapour growth of GaN. The last Subsection 3.4.1 focuses on molecular spectra and their origin.

### 3.1. Power absorption in the microwave field

The condition for MW breakdown of gases is given by

$$E_b = \frac{E_0}{\sqrt{2}} = \tilde{E} \quad (9)$$

when the root mean square (rms) value of the microwave electric field  $\tilde{E}$  reaches the breakdown electric field  $E_b$ . The amplitude of the MW radiation is denoted as  $E_0$ . For

### 3. Nitrogen plasma

an unmagnetized plasma, the frequency-independent effective electric field  $E_{eff}$  is defined as

$$E_{eff}^2 = \tilde{E}^2 \frac{v_c^2}{\omega^2 + v_c^2} \quad (10)$$

where  $v_c$  is the electron-neutral collision frequency and  $\omega$  is the angular frequency of the EM field [98]. It can be shown, that once MW breakdown of gas occurs, plasma can be sustained by lower electric fields. The power absorption per volume  $P_{abs}/V$  by plasma in a MW field is given by the equation:

$$\frac{P_{abs}}{V} = n_e \frac{e^2}{m_e v_c} \frac{v_c^2}{\omega^2 + v_c^2} E_b^2 \quad (11)$$

where  $n_e$  is the electron density,  $e$  and  $m_e$  are the electron charge and the electron mass, respectively. According to Equation 11, power absorption is the function of  $v_c$ , having a single maximum. [99, 100] This single maximum corresponds to the minimum value of MW breakdown electric field, visible in Fig. 3.1.

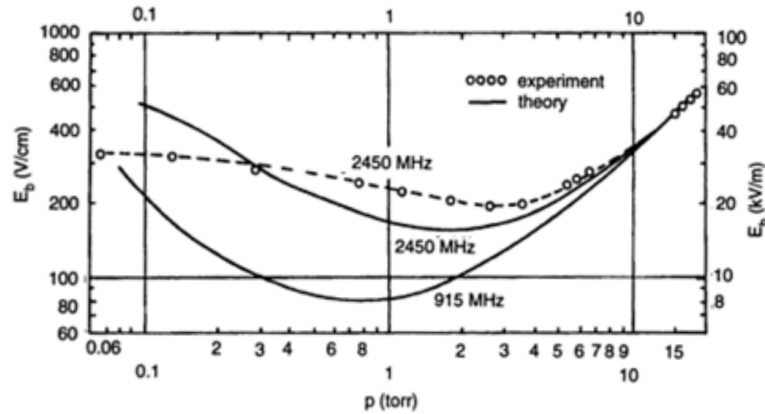


Figure 3.1.: Breakdown electric field of air against pressure [101]

The above breakdown electric field  $E_b$  curves in the function of pressure are the high frequency analogies of the Paschen curve for DC discharges. Paschen's law describes the breakdown voltage between two electrodes in a gas as a function of pressure  $p$  and gap length  $d$

$$V_b = \frac{Cpd}{\ln\left(\frac{Apd}{\ln\left(1 + \frac{1}{\gamma}\right)}\right)} \quad (12)$$

where  $V_b$  is the breakdown voltage in volts,  $A$  and  $C$  are gas-specific constants of Townsend's first ionization coefficient, and  $\gamma$  is a secondary electron emission coefficient [98]. For the plane parallel geometry, the breakdown electric field equals

$$E_b = \frac{V_b}{d} \quad (13)$$

In case of high frequencies one can show by solving a continuity equation that a breakdown electric field in unmagnetized plasma has the following dependency [98]. At high gas pressures the critical electric field for breakdown is directly proportional to the neutral gas pressure  $p$

$$E_b \approx C_1 p \quad (14)$$

where  $C_1$  is a constant. Whereas in the collisionless regime of low background pressure  $p$ , the dependency of  $E_b$  on  $p$  can be written as

$$E_b \approx \frac{C_2}{\Lambda_{dif} p} \quad (15)$$

where  $C_2$  is a constant and  $\Lambda_{dif}$  is the characteristic diffusion length. [98] High electric fields (compare Fig. 3.1:  $E_b = 20 \text{ kV/m}$  for air, at around 4 mbar) are required for reasonable power absorption and therefore plasma ignition, because of a small initial electron density  $n_e$  in plasma. As soon as  $n_e$  increases, and it can be shown that electron density increases exponentially during MW breakdown, even reduced electric fields provide high power absorption by plasma [100]. However, interaction between incoming electromagnetic waves and plasma is limited to a small, outer region of plasma – the ‘skin’. Efficiency of electromagnetic power coupling into plasma depends on the relation between the frequency of electromagnetic waves  $\omega$  and the plasma frequency  $\omega_{pe}$ . The latter is defined as [99]

$$\omega_{pe} = \left( \frac{e^2 n_e}{\varepsilon_0 m_e} \right)^{1/2} \quad (16)$$

where  $\varepsilon_0$  represents the permittivity of vacuum,  $n_e$  is the electron density,  $e$  - the charge of an electron,  $m_e$  - the electron mass. If  $\omega$  is below the  $\omega_{pe}$ , then the incoming wave is damped and partially re-radiated by the electrons in the outer layer of plasma. Although, owing to the skin effect small penetration of plasma takes place. For a high collision rate, when  $\nu_c \gg \omega$  the skin depth  $\delta_s$  is given by [99]

$$\delta_s = 2^{1/2} c \left( \frac{\varepsilon_0 m_e \nu_c}{e^2 n_e \omega} \right)^{1/2} \quad (17)$$

where  $c$  is the speed of light. However, if  $\omega$  is above the  $\omega_{pe}$ , the incident radiation is propagated through plasma, practically without attenuation or reflection. One can thus define the critical electron density  $n_c$ , above which the incident electromagnetic wave will be reflected [98]

$$n_c = \frac{\omega^2 m_e \varepsilon_0}{e^2} \quad (18)$$

The so-called cut-off density at 2.45 GHz is about  $7.45 \times 10^{16}$  electrons/m<sup>3</sup>.

## 3.2. Plasma classification

The fundamental classification of the gas discharge plasmas for local thermal equilibrium (LTE) plasmas and non-local thermal equilibrium (non-LTE) plasmas reflects temperature of species in plasma. LTE plasmas known also as thermal plasmas are characterised by equal temperature of electrons ( $T_e$ ) and heavy particles ( $T_g$ )  $T_e \approx T_g$ , and high electron density ( $10^{21} - 10^{26} \text{ m}^{-3}$ ). On the contrary, non-LTE plasmas have lower density of electrons ( $< 10^{19} \text{ m}^{-3}$ ), which are much hotter than the heavy plasma species,  $T_e \gg T_g$ . Typically, the pressure in the plasma is a decisive factor in this subdivision. At high pressures, frequent collisions among the plasma species cause efficient energy transfer between electrons and other particles, thus leading to equal temperatures of all

plasma species. On the other hand, when pressure is low enough (i.e. long collision free path), collisions occur seldom, and hence the energy transfer from fast electrons to heavier particles is much smaller. This results in  $T_e$  being much higher than  $T_g$ .

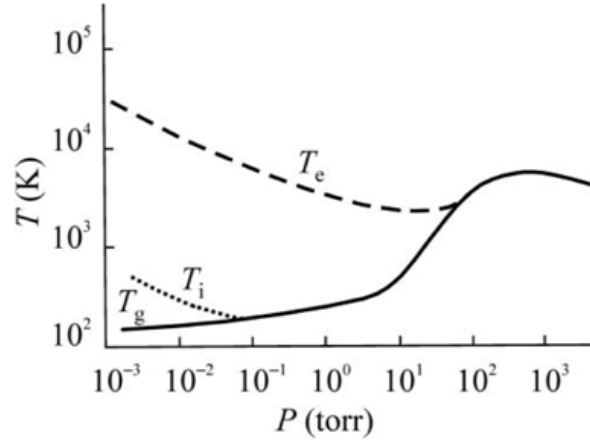


Figure 3.2.: Temperature of plasma against pressure [102]

Dependence of plasma temperature under stationary discharge conditions on pressure is depicted in Fig.3.2. Translational energy distribution among charged species is described by temperature  $T_i$ . [103, 102, 104, 105]

Non-LTE plasmas are not restricted only to low pressure regimes. Owing to the fact that thermal equilibrium is obtained after a certain time that means a certain number of collisions, it is possible to sustain a non-equilibrium discharge at higher pressures [104]. Distance between the electrodes or the length of the discharge is an additional factor influencing the hot and cold plasma division. Dielectric barrier discharge and glow discharge are examples of non-LTE plasmas working under atmospheric pressure. [103]

The degree of ionization  $x$  is defined as the ratio of charged carriers  $n$  to the total number of atoms/molecules in plasma ( $n + n_g$ )

$$x = \frac{n}{n + n_g} \quad (19)$$

where:  $n$  – density of charged particles,  $n_g$  – neutral particle density. Based on the value of the degree of ionization, plasmas can be divided into fully ionized plasma ( $x \approx 1$ ) and

partially ionized plasmas ( $x \neq 1$ ). Even very weakly ionized gases ( $x = 10^{-4} - 10^{-6}$ ) already behave like plasmas. When plasma is in LTE or close to this state, its transition from a neutral gas to the fully ionized plasma can be illustrated by the Saha equation [98].

There are two types of electric carrier - neutral collisions that transpire in plasma. Elastic collisions manifest themselves by the exchange of momentum between interacting particles without excitation taking place, whereas inelastic collisions result in electron excitation processes. The mean free path  $\lambda$  is the average distance covered by a relatively fast-moving particle, such as an electron or ion, between two successive collisions. It depends on the neutral particle density  $n_g$  and the collision cross section  $\sigma_c$  of the specific interaction [106]

$$\lambda = \frac{1}{n_g \sigma_c} \quad (20)$$

Dividing the mean free path by the charged particle velocity  $v$ , the mean time  $\tau$  between collisions is determined

$$\tau = \frac{1}{n_g \sigma_c v} \quad (21)$$

Averaging over all of the Maxwellian velocities of the charged particles, the collision frequency  $\nu_c$  is given by

$$\nu_c = \frac{1}{\tau} = n_g \sigma_c \bar{v} \quad (22)$$

Charged particles within plasma interact with each other by means of Coulomb forces. In consequence, one can speak about charge separation and a Debye sphere is a volume outside which charges are electrically screened (i.e. ion electric field is damped by mobile charge carriers in its surroundings). The radius of a Debye sphere is denoted as the Debye length  $\lambda_D$  – the length of field screening. When ions are much colder than electrons, then formula for the Debye length reads [98]

$$\lambda_D = \left( \frac{\varepsilon_0 k_B T_e}{e^2 n_e} \right)^{1/2} \quad (23)$$

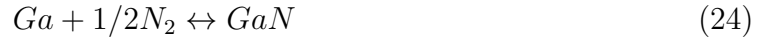
where:  $k_B$  – the Boltzmann constant,  $T_e$  – the temperature of electrons,  $n_e$  – the electron density.

### 3.3. Excited states of nitrogen

Nitrogen plasmas may usually contain several types of reactive species, including atomic N, excited molecular N<sub>2</sub> and nitrogen ions, like N<sub>2</sub><sup>+</sup>. Plasma composition depends heavily on its parameters and excitation method, i.e. DC discharges, pulsed DC discharges, dielectric barrier discharges DBD, RF, ECR, MW discharges, electron beam discharges, etc. [102]. For instance, ratio of atomic nitrogen to excited molecular nitrogen increases when the power of RF plasma source implemented for MBE growth increases [107]. Iliopolous et al. [108] investigated concentration of nitrogen atoms and excited molecular nitrogen in RF plasma versus nitrogen carrier gas flow and the coupled RF power. The concentration of nitrogen atoms was increasing with the RF power, while being unaffected by the change of the nitrogen gas flow. Yet, the concentration of excited molecular nitrogen was increasing with both parameters. Agarwal et al. [109] showed how composition of RF inductively coupled plasma (ICP) alters with pressure. In the pressure range below 1.3 mbar, excited nitrogen molecules dominate, while at higher pressures nitrogen atoms are the prevailing active species. Hughes et al. [110] compares the output of a RF ICP source and an electron cyclotron resonance (ECR) plasma source under MBE growth conditions of GaN. It was concluded that ECR plasma was rich in excited molecular nitrogen of 2nd-positive series and nitrogen molecular ions. The second positive system (SPS) of molecular nitrogen is comprised of fully allowed transitions from the electronic state  $C^3\Pi_u$  to the lower electronic state  $B^3\Pi_g$ , in the UV and visible range of 280 – 545 nm [111] (see also Appendix D). On the contrary the ICP RF source produced mainly atomic nitrogen and 1st-positive series of excited molecular nitrogen, resulting in the growth of better quality GaN films. The first positive system (FPS) of

molecular nitrogen includes transitions from the electronic state  $B^3\Pi_g$  to the electronic state  $A^3\Sigma_u^+$ , emitting light in the approximate region between 500 and 2500 nm [111].

Excited nitrogen species, with energy above the ground-state molecules, allow for the growth of GaN in the meta-stable growth region [112]. The reaction of Ga with nitrogen is reversible and it is governed by the competition between the forward reaction leading to the growth of GaN and the opposite process of GaN decomposition (Eq. 24).



The role of the excited nitrogen species is to provide enough energy to form GaN. By applying sufficiently high rate of active nitrogen species incoming at the growing surface, it is possible to prevail its decomposition. In this respect, relatively high kinetic barrier of  $\sim 2eV$  [12] for GaN decomposition is favourable. Considering potential energy of reactive nitrogen, it is to note that the excited neutral molecular nitrogen, the ionized molecular nitrogen and the atomic nitrogen present levels of potential energy above the one necessary to form GaN (Fig. 3.3), since the total energy barrier for GaN synthesis under typical MBE conditions is around 4 eV (kinetic barrier of  $\sim 2eV$  and Gibbs free energy of 1.9 eV).

The reverse reaction is limited by the high kinetic barrier, around 200 kJ/mole (2 eV/atom), catalytically decreased by the action of Ga, though [45, 113]. The change of the Gibbs free energy of GaN formation depends on the reaction path, on the growth conditions etc. For instance, Karpinski and Porowski [12] calculated the standard Gibbs free energy change of the reversible reaction (Eq. 24), based on the experimentally measured equilibrium temperature and pressure of a solution of  $N_2$  in Ga under high nitrogen pressure. Calculated values were between 0.3 eV and 1.2 eV, depending on the temperature.

## 3.4. Optical emission spectroscopy

Optical emission spectroscopy (OES) stands for one of the most established approaches for plasma diagnostics. It was developed in the decline of the 19th century and nowadays



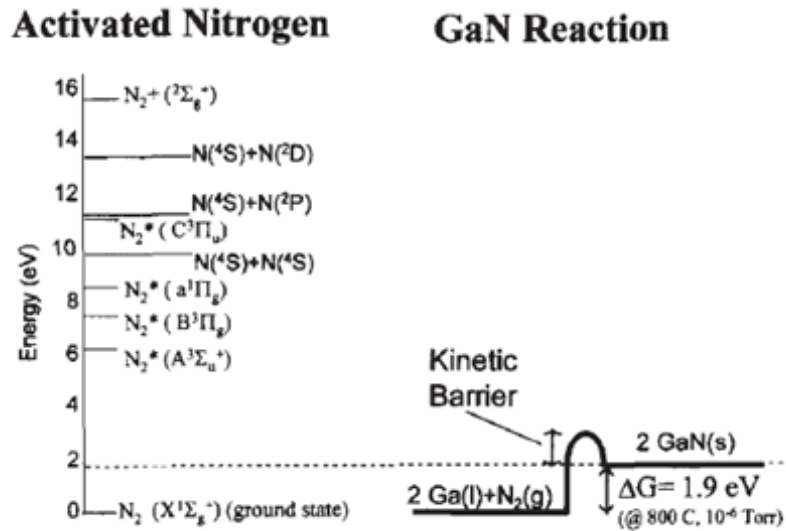


Figure 3.3.: Energy levels of excited nitrogen and energy barrier for GaN synthesis [112]

it is used to get insight into plasma composition and parameters. OES together with supplementary absorption spectroscopy are very common techniques, utilised not only in the fundamental research, but also in plasma processing and technology [114, 115]. In the OES electromagnetic radiation is recorded, spectrally resolved and further interpreted, based on universally available databases of spectral lines for elements and bands for molecules [116, 117, 118]. This is the most straightforward method of plasma characterisation, as only one port is needed for conducting measurements. OES is completely non-invasive, contrary to a Langmuir probe [119]. This in-situ technique does not come into contact with plasma and it is not affected by the presence of DC potentials or RF fields, which is definitely beneficial in the case of inductively heated reactors and microwave discharges. Additionally, it gives more freedom in the plasma source design. Spectra recorded by OES, even those with a moderate resolution, can quickly provide information on the type of species present in the discharge. Their identification is possible, provided that they emit radiation in the range of the installed detector. When comparing recorded lines (for atoms) or bands (for molecules and ions) with wavelength tables, plasma composition can be determined, provided a suitable model is used. Lines coming from higher orders of diffraction are suppressed by installation of an appropriate

filter. When characterising nitrogen plasma interaction with Ga vapour, the following issues should be taken into consideration: the rotational and vibrational temperatures, the gas temperature, presence of GaN molecules in vapour and plasma composition. They can be resolved by the careful study of emission spectra, allowing for a determination of plasma parameters. The gas temperature can be obtained twofold, either by the precision measurement of the line width or by the analysis of rotational lines of a vibrational band of a diatomic molecule. The first method assumes that the dominant broadening mechanism is the Doppler broadening and the Balmer line  $H_\alpha$  is a preferred choice for measurement. The latter one is based on the comparison of measured vibrational band of  $N_2$  with simulation of its spectra. Calculated rotational temperature  $T_{rot}$  in the excited state equals  $T_{rot}$  in the ground state ergo the gas temperature, if two following conditions are fulfilled. Firstly, the Franck-Condon principle is valid thereof the rotational quantum number is conserved during the electronic transitions. Secondly, the rotational levels of the ground state are populated as a result of heavy particle collisions. [120] Existence of GaN molecules in vapour has not been confirmed and reported so far, and to the author's best knowledge there is no spectroscopic data available. Theoretical investigations by Ueno et al. [121] predict  $X^3\Sigma^-$  to be the ground state and  $(1)^3\Pi$  the first excited state, having very close energies. Correct analysis of the recorded molecular spectra is thus of an utmost importance and the next subsection provides an insight into the basics of molecular spectroscopy, including notation used in this field.

#### 3.4.1. Molecular spectra

The most commonly observed molecular spectra consist of broad wavelength regions, so called 'bands'. The bands usually have at one end a sharp edge, where the intensity falls rapidly to zero – it is denoted as a band head. At the other end intensity falls off slower. The bands are said to be degraded to the violet or the red, when this gradual fall off intensity takes place towards shorter or longer wavelength, respectively. The molecular bands arise as the result of excitation of the additional degrees of freedom that molecules exhibit compared to a single atom, namely the vibrational and rotational motion of the

excited molecule (compare Fig. 3.4). Based on the Born-Oppenheimer approximation [122], energy components of the excited molecule can be treated separately

$$E = E_{el} + E_{vib}(n_{vib}) + E_{rot}(J) + E_{trans} \quad (25)$$

where  $E_{el}$  is the electronic energy,  $E_{vib}(n_{vib})$  is the vibrational energy,  $n_{vib}$  - vibrational quantum number,  $E_{rot}(J)$  is the rotational energy,  $J$  - rotational quantum number, and  $E_{trans}$  is the translational energy, being so small that usually neglected.

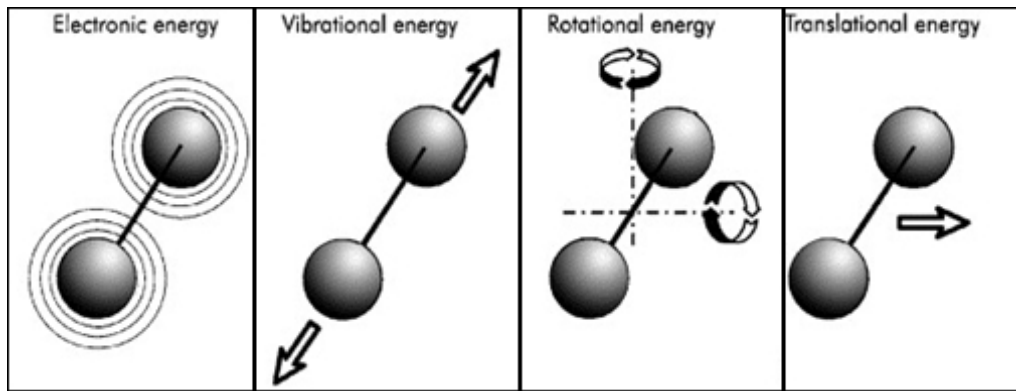


Figure 3.4.: Diatomic molecule - degrees of freedom

The vibrational and rotational features of the spectrum can be considered as separate contributions superimposed on the overall electronic transition between molecular states. A useful model for vibrational excitations is the quantum harmonic oscillator (Fig. 3.5), which has energy levels given by

$$E_n = (n_{vib} + 1/2)\hbar\omega_{osc} \quad (26)$$

where  $n_{vib}$  is the vibrational quantum number, an integer, and  $\omega_{osc}$  corresponds to the fundamental frequency of the simple harmonic oscillator. Transitions in which  $\Delta n_{vib} = -1$  lead to an emission spectrum of equally spaced lines. Vibrational spectra are observed in the IR region.

The rotational excitations can be approximated by a model of a rigid rotator. In this case the optical emission is associated with transitions between the quantized energy

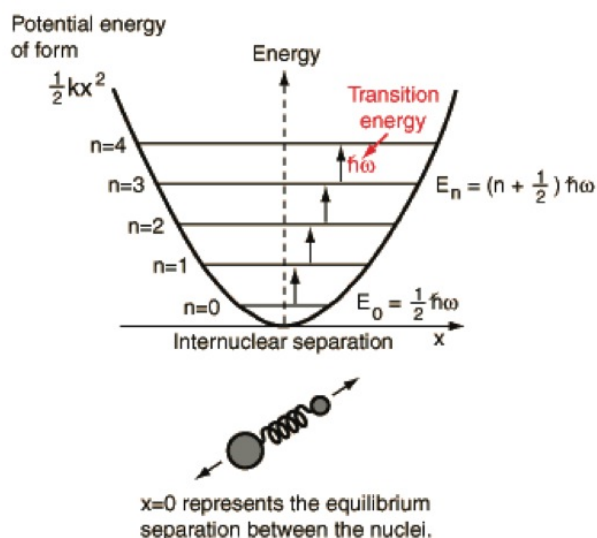


Figure 3.5.: Quantum harmonic oscillator [123]

levels of a rigid rotator. For a diatomic molecule

$$E_{rot} = \frac{\hbar^2 J(J+1)}{2I} \quad (27)$$

where  $\hbar$  – reduced Planck constant,  $J$  – the rotational quantum number,  $I$  – the moment of inertia of a diatomic molecule. The energy levels of the rotational states are not equally spaced. The rotational transitions typically produce spectra in the microwave region (see Fig. 3.6).

### Molecular term symbol for diatomic molecules

A molecular configuration is a specification of the occupied molecular orbitals in a molecule. For instance, in case of  $N_2$ , it is denoted as

$$1\sigma_g^2 1\sigma_u^2 1\Pi_g^4 2\sigma_g^2 \quad (28)$$

where  $\sigma$  and  $\Pi$  are the molecular orbital symmetry labels (shells), denoting the type of interaction between atomic orbitals. The  $g/u$  subscript applies only to molecules with the centre of symmetry and denotes the symmetry with respect to inversion through

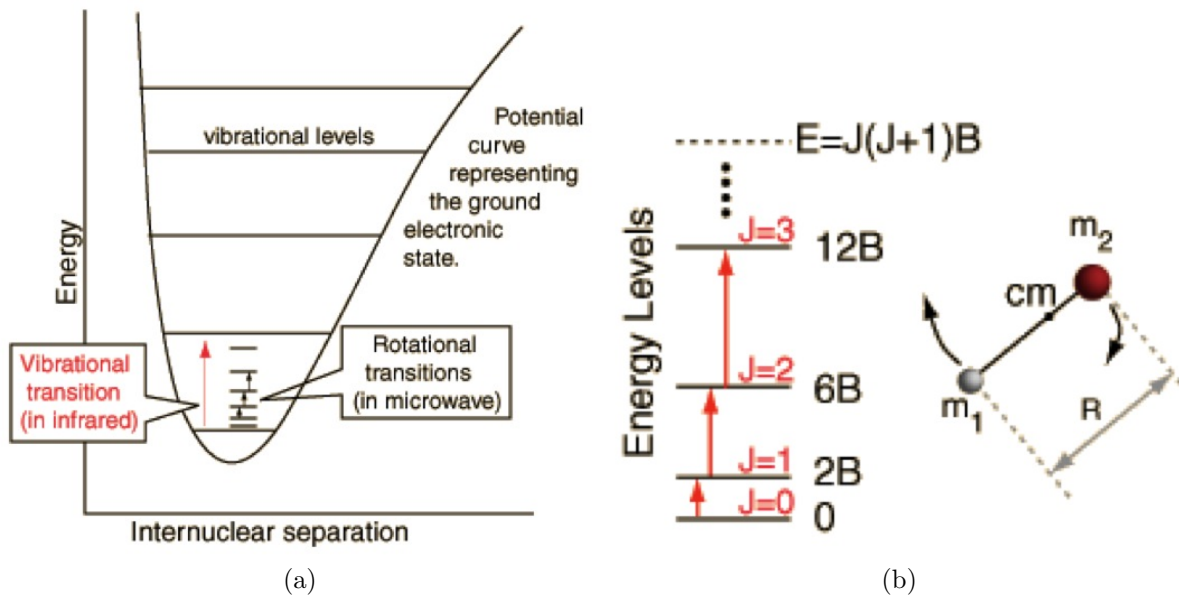


Figure 3.6.: Rotational transitions [124]

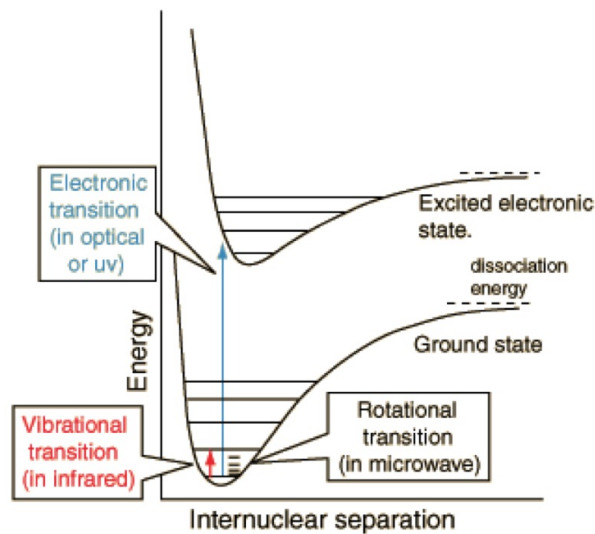


Figure 3.7.: Electronic, vibrational and rotational transitions [123]

the centre of symmetry (g - symmetric, u - antisymmetric) (Fig. 3.8 a). Depending on the arrangement of valence electrons, a certain molecular configuration may have several different states. A molecular term symbol classifies these states, providing information about the total spin and orbital angular momentum of the molecule. It has a general form

$$^{2S+1}|\Lambda|_{g/u}^{+/-} \quad (29)$$

where  $S$  is the total spin angular quantum number for the molecule, formed from the individual electrons' spin quantum numbers,  $\Lambda$  is the projection of the orbital angular momentum  $L$  along the internuclear axis (for  $|\Lambda| = 0, 1, 2, 3 \dots$  the notations are  $\Sigma, \Pi, \Delta, \Phi \dots$  respectively). The  $+/-$  superscript applies only to  $\Sigma$  states and denotes the symmetry with respect to reflection in a plane containing the internuclear axis (Fig. 3.8 b).  $\Omega$  is the projection of the total angular momentum along the internuclear axis (Fig. 3.8 c).

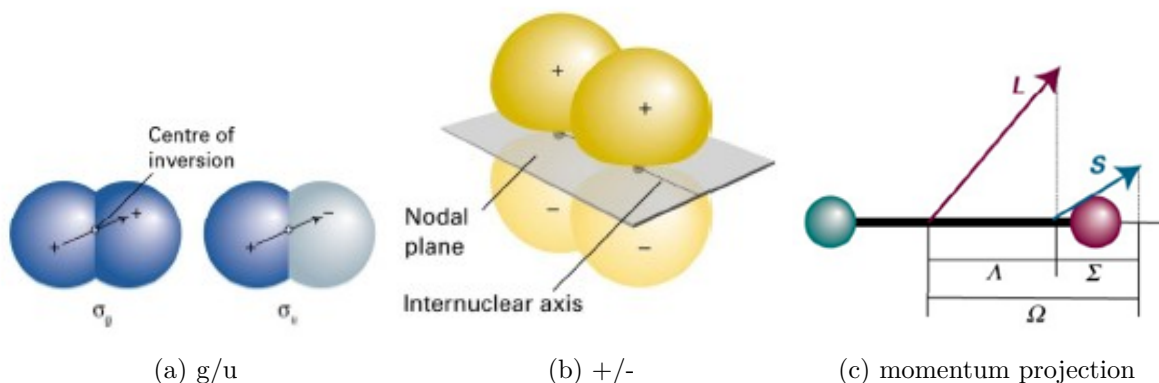


Figure 3.8.: Meaning of a) subscripts g/u, b) superscripts +/- and c) quantum numbers [125]

The ground state of nitrogen molecule is described by the molecular term  $^1\Sigma_g^+$ , because  $\Lambda = 0$  therefore a  $\Sigma$  term and since  $S = 0$  (all electrons paired), hence a singlet term.

### Nitrogen, electronic states

Curves of the potential energy versus internuclear distance are the usual way of presenting the energy levels of diatomic molecules. The convention is that the ground state is denoted as X, the excited states, which have the same multiplicity ( $2S + 1$ ) as the ground state, as A,B,C, etc., the excited states of different multiplicity than the ground state as a,b,c,... etc. However, the only exception to this rule is  $N_2$ , where A, B, C, ... designate the excited triplet states and a, b, c, ... the excited singlet states [117]. Curves

for nitrogen are depicted in Fig. 3.9.

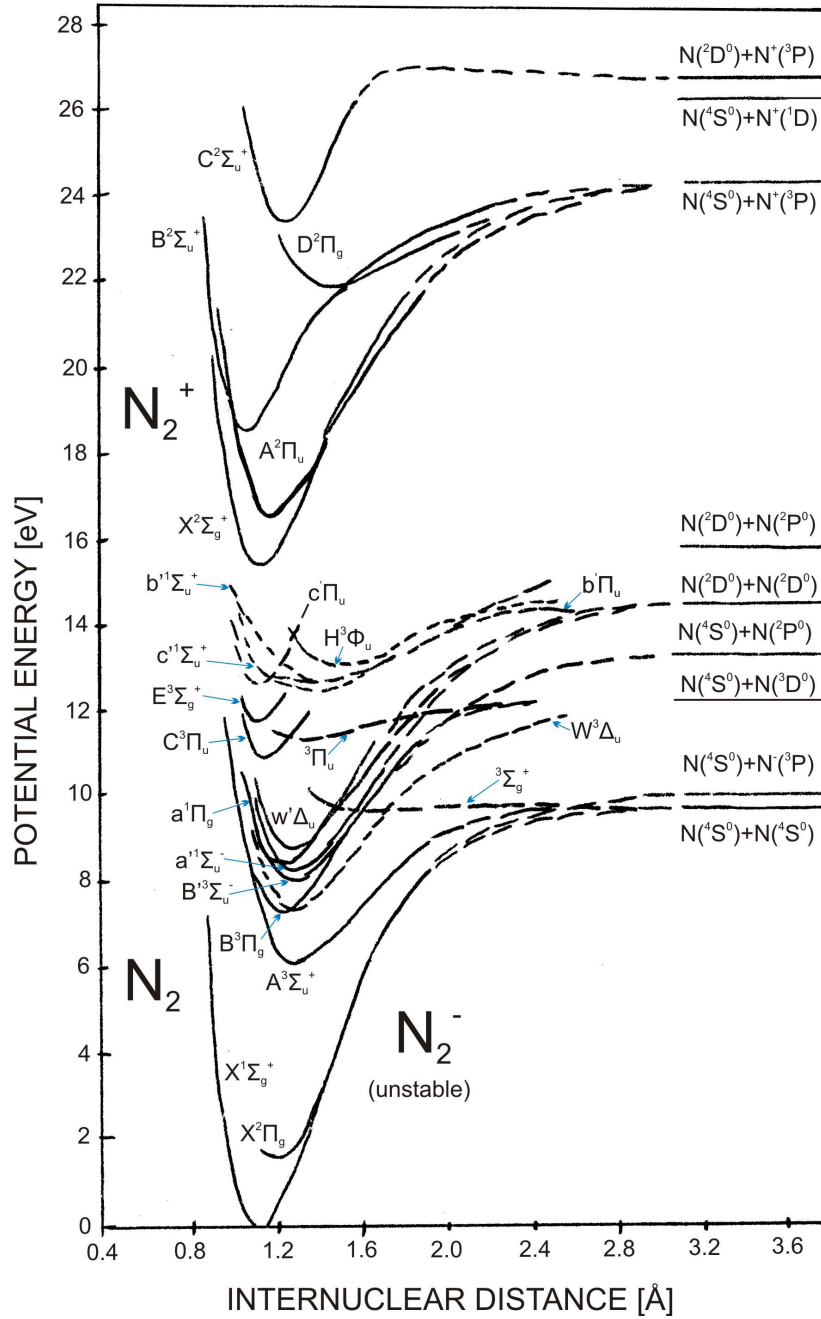


Figure 3.9.: Energy levels of nitrogen, based on [190]





# Chapter 4

## Plasma enhanced methods for GaN growth

In Chapter 4 topic of plasma enhanced methods for GaN growth is discussed. As it is shown, enhanced reactivity of the  $\text{NH}_3$  or nitrogen plasma can be successfully employed for the challenging synthesis of nitrides. Plasma enhanced growth methods using nitrogen instead of  $\text{NH}_3$ , benefit from higher growth rates. Furthermore, uncontrolled production of hydrogen from  $\text{NH}_3$  can be eliminated from the growth process. Due to the thermal instability of many nitrides, it was mostly cold plasma that has drawn the attention of the scientific community. Combination of high energy, sufficient to activate the inert  $\text{N}_2$  molecule and low temperature of plasma gas has been harvested in various techniques to grow GaN. Sections 4.1 and 4.2 are devoted to plasma-assisted epitaxy of GaN and plasma enhanced solution growth, respectively. The last part of the chapter concentrates on dielectric barrier discharge (DBD), implemented by our research group for PVT-based synthesis of single crystalline GaN.

### 4.1. Plasma assisted vapour epitaxy

In the vapour phase epitaxy, films are grown from gaseous precursors. In the case of most contemporary growth techniques of GaN from the vapour phase, precursors for Ga and active nitrogen need to be used. Typically GaCl (halide vapour precursor for Ga) and ammonia (hydride precursor for nitrogen) are utilised in halide vapour phase epitaxy (HVPE), metalorganic chemical vapour phase epitaxy (MOVPE) takes advantage of trimethylgallium (TMG) and  $\text{NH}_3$ , molecular beam epitaxy (MBE) employs  $\text{NH}_3$  as

well, whereas flow of Ga vapour comes from the evaporation of liquid Ga in the effusion cell. Selected results of the GaN growth by plasma assisted molecular beam epitaxy (PAMBE), plasma assisted metalorganic vapour phase epitaxy (PA-MOVPE) and remote plasma enhanced chemical vapour deposition (RPECVD) are discussed in the following section. PAMBE is nowadays a well-established method to produce high-quality single crystalline thin-films [127, 128], AlGaIn/GaN heterostructures for high-electron-mobility transistor (HEMT) devices with a two-dimensional electron gas (2DEG) confined within the structure [129, 130], light-emitting diodes (LEDs) and nitride-based laser diodes (LDs) [131, 132]. Within the range of pressures used in MBE ( $10^{-5} - 10^{-6}$  mbar), the average mean free-path of excited nitrogen is longer than 1 m [118], so that a remote plasma source (installed much closer than 1 m to the seed) is able to deliver excited nitrogen species to the growth zone. Electron cyclotron resonance (ECR) microwave plasma sources [133] fell into desuetude in the case of PAMBE, replaced by radio frequency (RF) plasma sources that provide higher quality of GaN films. Supposedly the nitrogen ions (first negative series) produced by ECR, were responsible for deterioration of the surface quality, reported for GaN growth by PAMBE [110].

Reflection high-energy electron diffraction (RHEED) system enables a real-time monitoring of crystal growth, which takes place in a carbon- and hydrogen-free environment. Low growth rate of few  $\mu\text{m}/\text{h}$  (typically below  $3 \mu\text{m}/\text{h}$ ) is counterbalanced by the unprecedented control of atomic layer by layer growth, smooth surfaces and sharp interfaces [127, 128], and low threading dislocation density (TDD) ( $10^4 - 10^6 \text{ cm}^{-2}$  depending on substrate quality) of the grown layers.

PA-MOVPE derives from MOVPE, which has become a major technology for growth of III-V based optoelectronic devices, owing to the progress made in the growth of device-quality GaN epilayers on sapphire and the two-step growth technique, where a LT buffer layer was followed by a HT layer growth [134, 135]. MOVPE is normally operated at moderate pressures from around 10 to 970 mbar. In the epitaxial growth of GaN TMG and  $\text{NH}_3$  are used as precursors for Ga atoms and N atoms, respectively [136]. When employing PA-MOCVD for GaN growth, either  $\text{NH}_3$  is excited by plasma or  $\text{NH}_3$  is

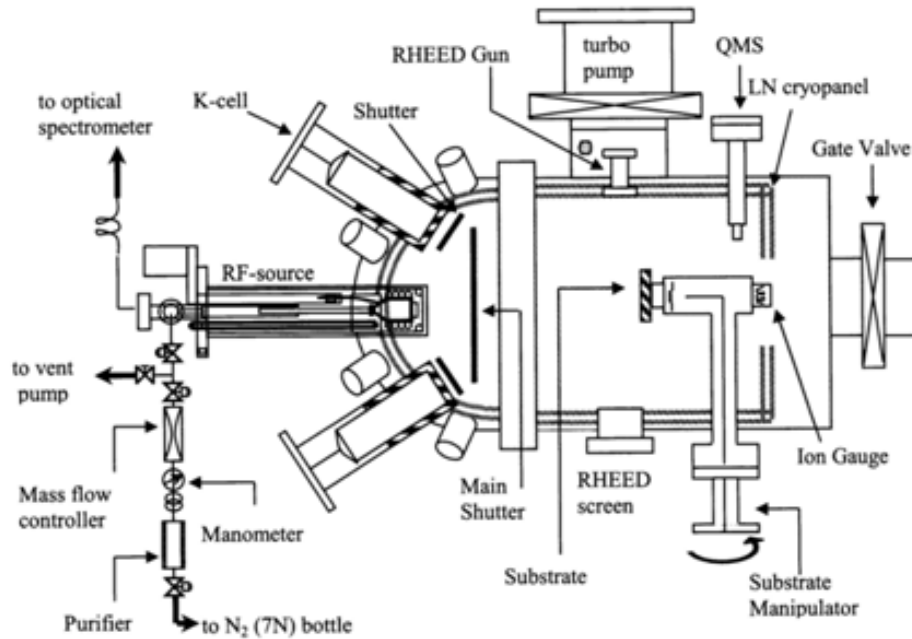


Figure 4.1.: Schematic drawing of a typical PAMBE system [132]

replaced by nitrogen plasma that serves as a source of reactive nitrogen. Hassan et al. [137] reported on low-temperature (200 °C) grown GaN of mixed amorphous and microcrystalline structure in  $\text{NH}_3/\text{N}_2$  atmosphere on Si (111), using 2.45 GHz ECR PA-MOCVD system, whereas Lee succeeded in realization of metal-semiconductor-metal (MSM) photodiodes based on GaN films on Si (111) grown by the same ECR PA-MOCVD method [138]. ECR-heated plasma spanned the horizontal quartz reactor up to the substrate heater (see Fig. 4.2).

Ihashi et al. [139] implemented microwave (2.45 GHz) plasma in the MOCVD setup (Fig. 4.3).  $\text{NH}_3$  gas was replaced by a mixture (1:1) of nitrogen and hydrogen. GaN stoichiometric films on fused silica were obtained at a total pressure of 6.5 mbar. Influence of the substrate position in the plasma on the surface temperature of the substrate was investigated and reported.

In the early work of Choi et al. [140] the RPECVD method was investigated as an alternative for MOVPE. Pressure in the reactor equalled 1.3 mbar. Schematic drawing of the setup is presented in Fig. 4.4. The RF coil, surrounding the plasma tube, was used

#### 4. Plasma enhanced methods for GaN growth

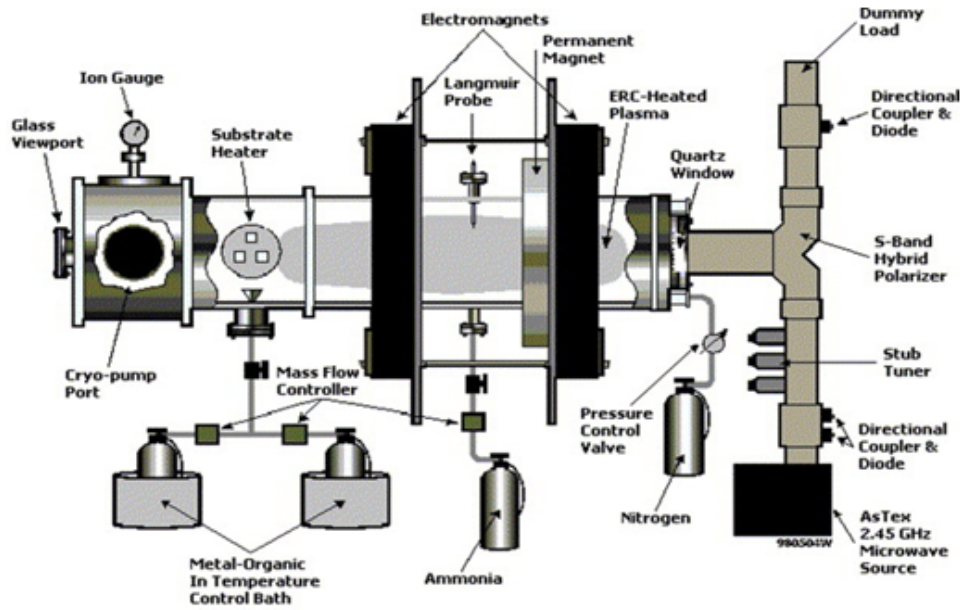


Figure 4.2.: ECR plasma-assisted MOCVD system [138]

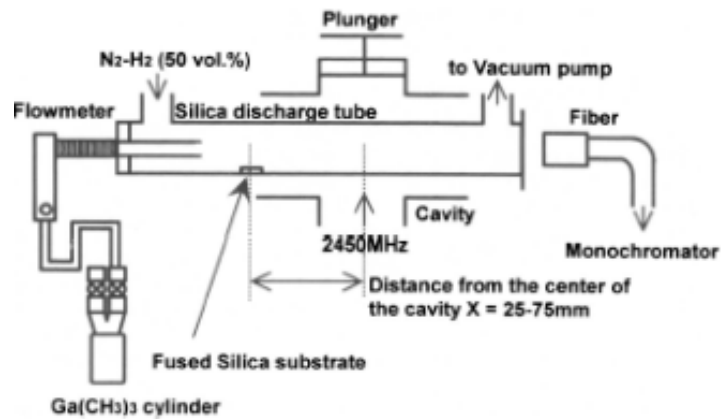


Figure 4.3.: MW plasma enhanced MOCVD setup [139]

to excite either NH<sub>3</sub> or N<sub>2</sub> diluted with helium (He) and subsequently injected upstream into the deposition tube. The role of He was to provide energetic electrons and long-lived metastable atoms. Growth experiments at temperatures in the range 315 – 500 °C resulted in thin polycrystalline GaN films (exact thickness not revealed) on sapphire (0001) and (111) silicon.

Nagata et al. [141] proposed to replace a conventional NH<sub>3</sub> source of N with nitrogen plasma from barrier discharge, succeeding in the growth of single crystalline GaN at the

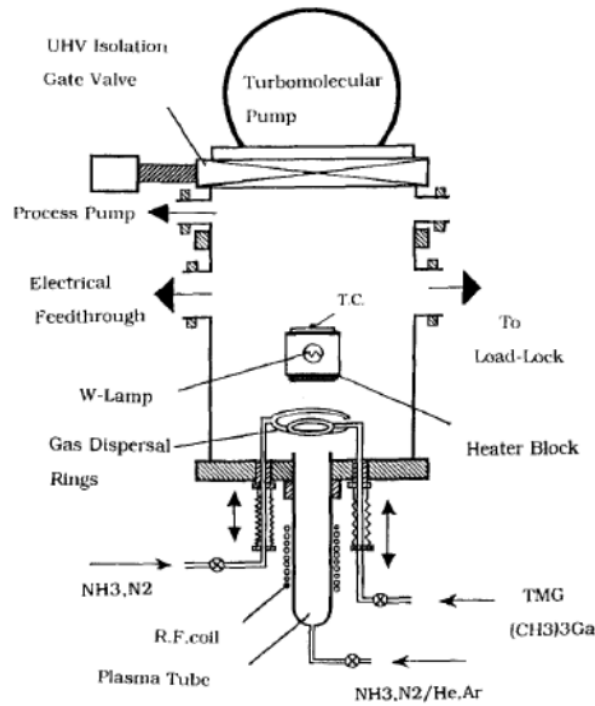


Figure 4.4.: RPECVD setup [61]

near atmospheric pressure. The modified MOVPE system is presented in fig. 4.5. Pure N atmosphere was used, since He discharge is known to produce at atmospheric pressure undesired corona discharges and glow discharges. Nitrogen plasma was generated locally at the seed, within a 1 mm thick uniform gap, formed by two parallel electrodes. Alternating pulsed voltages (3-7 kV) were applied to the electrodes at a frequency of 30 kHz. Process resulted in 300 nm thick GaN film grown on (0001) sapphire at a pressure of 400 mbar [141].

## 4.2. Plasma assisted solution growth

Ozawa et al. [142, 20] proposed solution growth of GaN with 2.45 GHz MW plasma assistance at moderate pressure. In this approach atomic nitrogen reacts with Ga on the surface of the metal, forming Ga-N clusters, which are then transported by thermal convection flow to the bottom of the crucible. The actual growth of GaN takes place at the bottom of the crucible. The growth setup is depicted in Fig. 4.6.

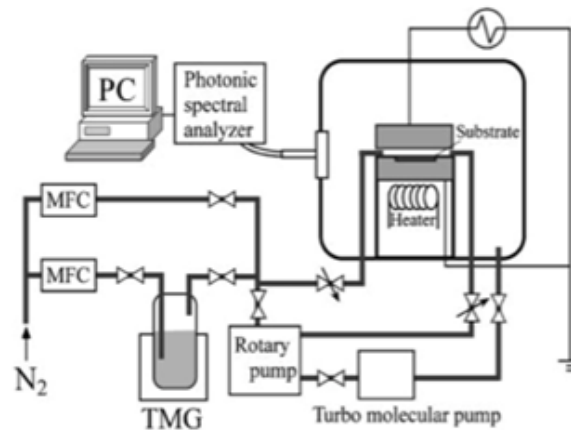


Figure 4.5.: Modified MOCVD setup. Barrier discharge as a source of reactive nitrogen [141]

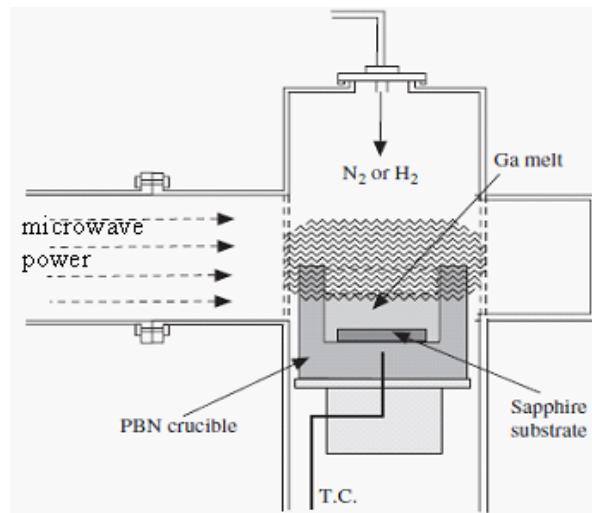


Figure 4.6.: Schematic drawing of the growth setup [142]

Under pure nitrogen plasma only polycrystalline GaN was synthesized at pressures of 2 - 4 mbar and temperature of 610 – 700 °C. By using the plasma mixture of nitrogen and hydrogen (50:50), the crystalline GaN film was grown on the sapphire substrate at the average rate of 0.6  $\mu\text{m}/\text{h}$ . Hydrogen plasma prevented high nucleation density at the surface of Ga melt by removing Ga oxide, thus allowing for growth of single crystalline material.  $\text{H}_2$  may also lower kinetic barrier on the seed by saturation of dangling bonds [143].

Plasma assisted solution growth method of nitrides is under development in the Leibniz

Institute for Crystal Growth. Although it is primarily focused on growth of indium nitride (InN), prerequisites for growth of both aluminium nitride (AlN) and GaN are being taken into consideration as well. Combining the high-pressure solution growth of GaN [144] and the industrially ubiquitous steel nitridation by plasma [145], a novel approach to synthesize AlN, GaN and InN has been proposed. Plasma activated nitrogen should be dissolved in a molten metal, transported by thermal convection flow and diffusion to the substrate and finally form III-N compound. The substrate is not in direct contact with plasma, thus substrate damages by highly energetic plasma species and the unintentional increase of its temperature are hindered. High flow of the reactive ionised nitrogen and high temperature gradient in the melt are to be obtained by applying a negative voltage (so called bias) at the melt surface. Real-time control of the temperature gradient in the melt and the intensity of the ion current would allow for high growth rates. Inductively coupled plasma source (ICP) has been implemented into the resistively heated reactor. Current experiments are conducted with In- melt at  $T_{growth}$  of about 700 °C within the pressure range of 0.01 – 1 mbar. [65]

### 4.3. Physical vapour transport with barrier discharge in IKZ

Dielectric barrier discharges (DBD), called also silent discharges [146], have been in use since 1857, when Siemens [147] employed DBD for the generation of ozone from air or oxygen. Nowadays these types of discharge have many applications additionally to water treatment, in modern plasma display panels [103], pollution control, the pumping of CO<sub>2</sub> lasers, the production of methanol from methane/oxygen, various thin film deposition processes, etc. [103, 146, 148]. The DBD discharge is generated between two electrodes with a dielectric layer (made of glass, quartz, ceramic material or polymer) placed in between. The dielectric barrier limits the discharge current thus avoiding the arc transition and distributes the micro-discharges over the entire electrode surface area, ensuring the homogeneous treatment [105]. Dimension of the gas-filled gap between the electrodes is

usually around 0.2 – 5 mm. A voltage of 1 - 100 kV with the repetition frequency of 50 Hz – 1 MHz is applied to the electrodes, in order to sustain the discharge. DBDs are typically operated at pressures 0.1 – 1 bar. [146, 148, 99, 104]. Our research group has designed and employed a DBD device in the PVT growth of GaN crystals. The main goal of the research was to develop a plasma source capable of long-term stable operation under proposed GaN growth conditions ( $T_{growth} = 1000\text{ }^{\circ}\text{C} - 1200\text{ }^{\circ}\text{C}$ ,  $p = 200 - 800\text{ mbar}$ ). DBD device working in the vicinity of the seed should provide enough energy to activate nitrogen and concurrently prevent formation of Ga droplets in the vapour. Therefore, use of the aggressive and thermally unstable  $\text{NH}_3$  would be no longer necessary. When designing a DBD, few requirements were taken into the consideration. The 2D symmetry of an electrode array would provide easy installation of a plasma source inside the reactor. The dimensions were limited by the maximum size of the seed, which was set to 1 inch, owing to the costs of materials and reactor parts. The distance between the electrodes and the dielectric material should be minimized, to avoid sparks at lower pressure. The choice of the material system for the plasma source was of an utmost importance. Tables 4, 5 and 6 in Appendix A display lists of materials, which were under review for the electrodes and dielectric barrier. Consultations with manufacturers of ceramics and preliminary experiments with some test-structures (Fig. 4.7) lead to the following conclusion. Molybdenum (Mo) wire in an aluminium oxide ( $\text{Al}_2\text{O}_3$ ) tube is the most suitable building element of a DBD device, operated under the growth conditions for GaN in the PVT method. Mo has a high melting temperature  $T_m = 2623\text{ }^{\circ}\text{C}$ , relatively low sputtering rate of  $421\text{ \AA}/min$ , it is stable in contact with  $\text{Al}_2\text{O}_3$  and presents better machinability than tungsten (W).

A DBD device applicable for the growth setup is presented in Fig. 4.8.  $\text{Al}_2\text{O}_3$  tubes were securely installed within the  $\text{Al}_2\text{O}_3$  ring by means of ceramic glue Aremco Ceramabond™ 865 (stable up to  $1650\text{ }^{\circ}\text{C}$ ). The Mo wire ends were rounded and welded with Mo carrier half-rings (one for each voltage polarity).

The source was placed in front of the seed within a distance of 2 mm. The experiment at  $T_{source} = 1230\text{ }^{\circ}\text{C}$ ,  $T_{seed} = 1080\text{ }^{\circ}\text{C}$  and  $p = 400\text{ mbar}$  resulted in a thin textured



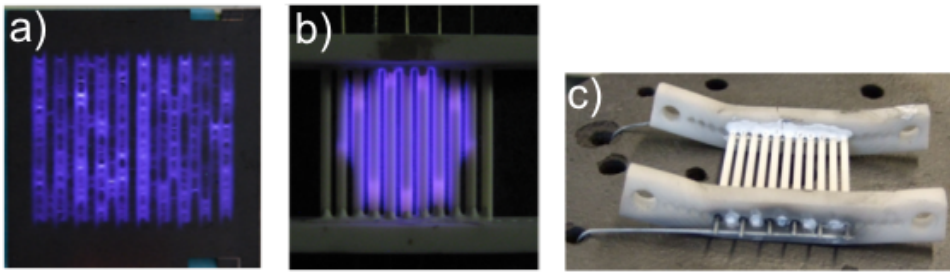


Figure 4.7.: a) Coplanar discharge in  $\text{Si}_3\text{N}_4$  ( $\text{Si}_3\text{N}_4$  becomes conductive at  $1400\text{ }^\circ\text{C}$ ), b) DBD with Cu-wires in  $\text{Al}_2\text{O}_3$  at RT, c) Test structure after operation at  $1100\text{ }^\circ\text{C}$



Figure 4.8.: DBD source mounted into the growth setup

GaN layer grown on a bare sapphire substrate within 4 h, with a growth rate at the order of  $10\text{ }\mu\text{m/h}$ . Furthermore, strong Ga lines and temperature dependent nitrogen spectra with excitation in the  $3 - 4.2\text{ eV}$  range were revealed in the OES spectra [60]. GaN was confirmed in the deposit by XRD measurements, thus it was shown that the implemented setup is capable of growth of GaN films. However, DBD assisted PVT growth of GaN has some inherent limitations. Electrodes are an obstacle in front of the seed, demanding more effort for homogeneous growth, either in the design of the DBD itself or by rotation of the seed during the growth. As the T increases, the barrier ceramics becomes conductive, limiting the maximum growth temperature. The small distance to the seed limits layer thickness without controlled seed-holder motion. In order to overcome the above mentioned problems, development of a microwave plasma

#### *4. Plasma enhanced methods for GaN growth*

---

source was initiated. The MW plasma approach seemed more promising for GaN growth, since it is able to supply more power at higher pressures, which in turn would result in the increased density of excited nitrogen, but also gas temperature. One goal of the research described in the dissertation was to learn, how this negative effect of enhancing GaN decomposition could be compensated by the supply of higher concentration of excited nitrogen.

# Chapter 5

## Experimental - MW plasma enhanced growth

Starting from the system outline of the main components, MW plasma generation system and growth setup are described. It follows the improvement of plasma stability, Ga evaporation, and deposition experiments as optimisation tool and finally, seeded growth of GaN single crystalline layers. Process stability depends essentially on stability of MW plasma and is one of the requirements for long-time growth experiments, while continuous supply of Ga into the growth region is another one. Therefore, the study on Ga vapour in the growth setup is described. Furthermore, stability and perfection of seeds is stressed as prerequisite for perfect layer growth. Finally, outcome of the deposition and growth experiments is discussed and summarized to draw conclusions out of experimental data.

### 5.1. Outline of the system

This section concentrates on the main element of the system, namely a stainless steel reactor, giving concurrently a description of the whole system, though.

Experiments were conducted in the computer-controlled system, custom designed for the plasma enhanced growth of GaN from gas phase. The main components of the system are: stainless steel reactor, growth setup with RF heating, gas flow and pressure control, MW plasma generation system, network analyzer (NA) for resonance frequency tuning and optical emission spectrometer (OES) for plasma characterisation. The system is used in two different configurations, depending on process stage. Configuration nr 1 is used for preparation of plasma ignition – the adjustment phase, whereas configuration nr 2

## 5. Experimental - MW plasma enhanced growth

is used for ignition and during plasma operation. Figure 5.1 presents the layout of the system in the configuration nr 1 (switch in A position) and configuration nr 2 (switch in B position). The main components are shown also pictorially in Fig. 5.2, in the real working environment.

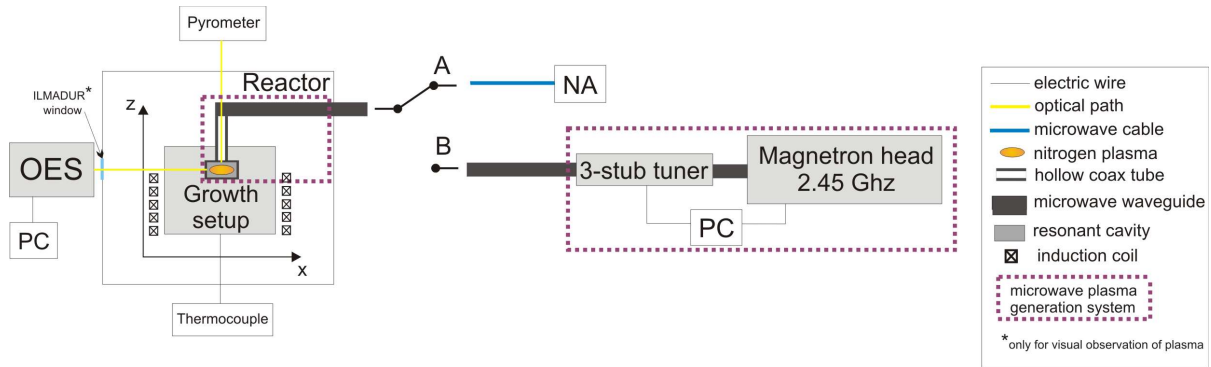


Figure 5.1.: A - configuration nr 1, B - configuration nr 2

The main component of the system constitutes the stainless steel reactor manufactured by Systec System- und Anlagentechnik GmbH & Co. KG. The remaining elements of the system are either connected to the reactor or incorporated into it. This water-cooled chamber is equipped with a vacuum line, containing a backing pump and a diffusion pump.  $N_2$ ,  $H_2$ , and Ar are provided by a gas supply line.  $N_2$  is additionally purified in ALPHAGAZ PURIFIER  $O_2$ -FREE before reaching the reaction chamber. The temperature profile in the source and growth area is established by means of the water-cooled induction coil, operated at 10 kHz [149]. It is placed in the middle of the reactor (see Fig. 5.2) and it is vertically movable. The growth setup, surrounded by the induction coil, is assembled on the quartz support (Fig. 5.2).

The resonance cavity belongs to the growth setup as well as to the MW plasma generation system itself. The MW generator is located outside the reactor and MW power is transmitted along a standard R-26 rectangular waveguide line, which is led through a quartz window into the reactor. A special R-26 part, made of molybdenum, is installed between two water-cooled flanges, to transfer microwaves into a coaxial line, which ends

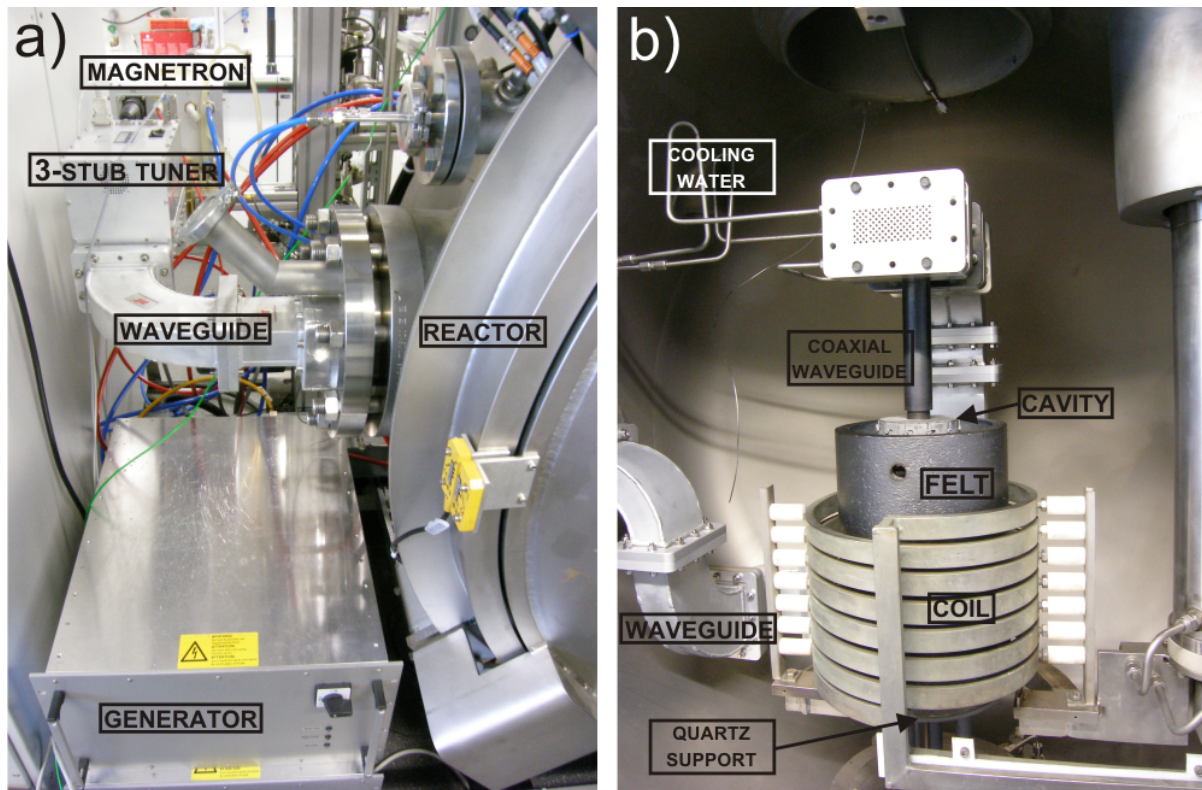


Figure 5.2.: Main system components a) outside the reactor and b) inside the reactor

in the growth setup. This end is connected to the seed-holder and surrounded by the cylindrical microwave cavity. Optical emission spectrometer (iHR 320 HORIBA Jobin Yvon) offers in-situ plasma process control. It has an optical access to the growth region through the front window of the reactor, holes in the isolation felt and in the susceptor. Network analyzer (HP8753C with HP85047A) is used only in the configuration nr 1 (see Fig. 5.1), during mechanical tuning of the resonance cavity, to measure the two-port  $S_{11}$  parameter. The subsection 5.1.2 discusses the microwave plasma source and supplementary devices: optical emission spectrometer and network analyzer in details.

### 5.1.1. Growth setup

This subsection lists all the components of the growth setup and specifies their materials parameters. Main functions of setup parts are explained. Scheme of the growth setup is shown in Fig. 5.3, whereas Fig. 5.2 b) depicts growth setup elements in the working

environment. Furthermore, results of modelling of temperature distribution in the growth setup, obtained by Virtual Reactor HEpiGaN software, are presented.

The growth setup was arranged to ensure that the following requirements are met:

1. Growth setup allows following growth parameters:
  - a) temperature of the seed 900 – 1100 °C
  - b) temperature of the Ga source 1200 – 1400 °C
  - c) total pressure in the reactor 200 – 800 mbar
  - d) atmosphere of nitrogen,
2. Chosen materials withstand growth process conditions,
3. Growth area is defined by the resonance cavity, built in the growth setup,
4. Seed is mounted inside the resonance cavity,
5. There is a possibility to manually adjust the position of the cavity along the vertical axis,
6. Microwave nitrogen plasma is ignited inside the cavity and burns in the vicinity of the seed,
7. Temperature measurement of the Ga source and seed with thermocouple and pyrometer, respectively,
8. Optical emission spectrometer has an optical access to the growth area,
9. Influence of the setup building materials on the process is minimized.

Taking advantage of the author's experience in the PVT growth of GaN and of the knowledge gained by our group in vapour phase growth of SiC [150, 151] and GaN [46], the growth setup was designed and implemented in the reactor (Fig. 5.3). The growth setup is placed on the quartz support. Two main segments to be distinguished are: the Ga source region in the lower section of the growth setup and the growth region in its

upper one. The Ga source region is kept at temperatures in the range of 1200 – 1400 °C, so as to reach the desired Ga vapour pressure in the reactor. Measurements of the Ga source temperature are done with a thermocouple, type C, suited for measurements in the range 0 - 2320 °C. Liquid Ga fills the round crucible, made of sintered graphite CZ3P20, covered with pyrolytic Boron Nitride (p-BN) layer. The crucible is placed in the susceptor, which inner diameter is 138 mm and the outer one equals 158 mm. Grooved channels in its lower part and the opening in its bottom are designed for N<sub>2</sub> carrier gas, enhancing transport of Ga vapour into the growth region bordered by the resonance cavity. The cavity is also the end section of the MW plasma generation system (see Subsection 5.1.2). Openings in the resonance cavity bottom allow for Ga vapour supply into the cavity, where the seed is mounted at the top flange (Fig. 5.3). The seed temperature is set within the range of  $T_{seed} = 900 - 1100$  °C. It is measured on the graphite covered backside of the seed with a pyrometer, IMPAC IP65, which works in the range of 800 - 2000 °C.

The most outer component of the growth setup is a graphite isolation felt, composed of tube, bottom disc and lid, surrounding the other setup parts. A hole in the graphite tube at the height of the cavity is part of an optical path for OES. By means of a hole (diameter of 50 mm) in the centre of the top disc, the coaxial waveguide was connected with the resonance cavity. Six outlets for carrier gas (each of them 14 mm in diameter) are symmetrically distributed around the centre hole in the insulation lid. Nitrogen carrier gas enters the growth setup from the bottom, via the inlet located in the very centre of the base disc of the insulation felt and susceptor. The felt is made of carbon-bonded carbon fibre (CBCF 15 - 2000), characterised by low thermal conductivity  $\alpha_{th}$  [W/m·K]. In nitrogen atmosphere it equals: 0.35 (at 500 °C), 0.54 (at 1000 °C) and 1.24 (at 2000 °C). Other important parameters are its density  $\rho = 170$  kg/m<sup>3</sup> and specific heat capacity  $c_p = 2100$  J/kg·K [152].

The susceptor is made of sintered graphite denoted as CZ3P20 (R6300) with high emissivity of  $\varepsilon = 0.7$ . Inductively heated with 10 kHz the penetration depth is about 10 mm. Subsequently energy is transferred by radiation to the growth crucible. By

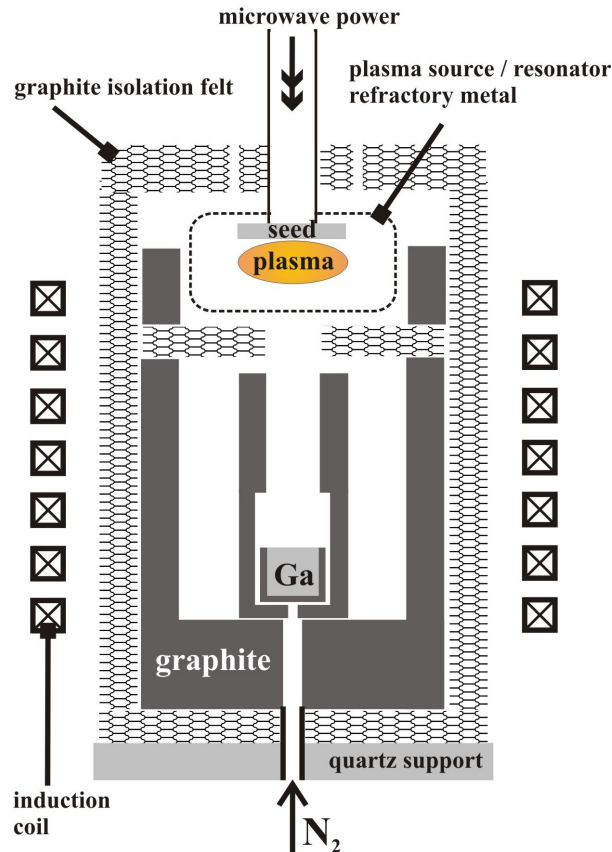


Figure 5.3.: Growth setup

stacking of several graphite rings the desired temperature gradient is formed along the vertical axis of the growth setup. A hole in the susceptor (diameter of 18 mm) serves as an optical access for OES to the growth region.

An alternative for the above described growth setup is a carbon-free version, without any graphite element. All the parts have the same dimensions like their carbon-containing equivalents, though. The outer isolation felt is made of Ultraform KVS 184/400 [153], containing 78% of  $\text{Al}_2\text{O}_3$  and 22% of  $\text{SiO}_2$ . Its density equals  $\rho = 400 \text{ kg/m}^3$ , whereas thermal conductivity  $\alpha_{th}$  [W/m·K] with 0.19 (at 600 °C), 0.25 (at 1000 °C) and 0.33 (at 1400 °C) is even lower than in case of CBCF 15-2000. Maximum operating temperature of 1800 °C fulfils the requirements for GaN growth. The isolation separating the Ga source from the growth region, is made of sintered silicon nitride (SSN- $\text{Si}_3\text{N}_4$ ) with thermal conductivity of 20 W/m·K (at RT) [154]. The Ga crucible is made of SSN-



$\text{Si}_3\text{N}_4$  either. A stack of five laser-cut Mo radiation shields serves as a top isolation (Fig. 5.4). The susceptor material is tungsten, with emissivity of  $\varepsilon = 0.07$  (at 500 °C) and  $\varepsilon = 0.15$  (at 1000 °C). The third version is a growth setup with greatly reduced carbon content. It comprises the combination of materials from two above described setups, being more similar to the carbon-free setup, though. The only difference applies to the outer isolation felt, which instead of Altraform KVS 184/400, is made of CBCF 15-2000. Such change in arrangement was induced by the fact that during growth experiments Altraform KVS 184/400 contaminates the reactor with oxygen.



Figure 5.4.: Mo radiation shield

The goal of simulations, done in Hydride Epitaxial GaN Simulator (HEpiGaNSTM), was to find the proper growth setup configuration and induction coil position, so as to  $T_{seed}$  would equal 1000 °C and simultaneously  $T_{source}$  would reach 1300 – 1400 °C. HEpiGaNSTM belongs to a Virtual Reactor family of two-dimensional (2D) software tools designed for the simulation of long-term growth of bulk crystals from the vapour phase. It was primarily designed for modelling of GaN crystal growth by halide vapour phase epitaxy (HVPE). In this thesis HEpiGaNSTM was exploited for modelling of temperature distribution in the growth setup. For the global heat transfer inductive heating, conductive heat transfer in solid materials, where the thermal conductivity of the materials used in the growth system can be prescribed by the user as a func-

tion of temperature, and both convective and radiative heat transfer in transparent gas blocks are considered. Comprehensive description of HEpiGaNSTM can be found on <http://www.str-soft.com>.

While temperature of the seed was fixed, the following parameters were optimized: configuration of graphite susceptor rings, their number and height, the vertical position of the induction coil and  $T_{source}$ . The basic growth setup geometry with denoted materials used for simulations is presented in Fig. 5.5, whereas materials parameters were taken from the default database of HEpiGaNSTM.

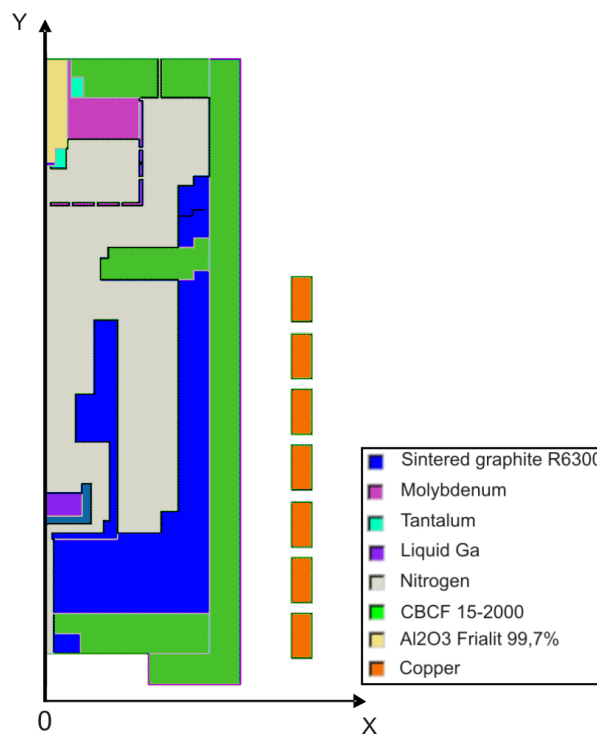


Figure 5.5.: Coil position  $y = 20$  mm

Fig. 5.6 presents the influence of the total height of the upper carbon susceptor on the temperature field in the growth setup. Coil position is set to 20 mm and pressure to 400 mbar. The upper susceptor contributes in a great extent to the seed temperature. Without this susceptor, the seed is mostly warmed up by heat convection from the lower part of the growth setup. Therefore, more energy needs to be transferred into the system by the induction coil to obtain the desired  $T_{seed} = 1000$  °C. It implies an increase of

$T_{source}$  in comparison to the case, when the upper susceptor is installed. In Fig. 5.6 a)  $T_{source} = 1418 \text{ }^\circ\text{C}$ , whereas in Fig. 5.6 b) it reaches  $1370 \text{ }^\circ\text{C}$ . Based on the described above simulation results, a method to control  $T_{source}$  by the adjustment of the upper susceptor configuration was developed. When the seed temperature and the position of the induction coil are fixed, then  $T_{source}$  directly depends on the upper susceptor arrangement. In Fig. 5.6 c) the resulting temperature field is depicted, in the case of applying the higher upper susceptor configuration (30 mm height).

In Fig. 5.7 the temperature field for two different coil positions is compared. The graphite susceptor,  $p_{N_2}$  and  $T_{seed}$  were the same in both cases.

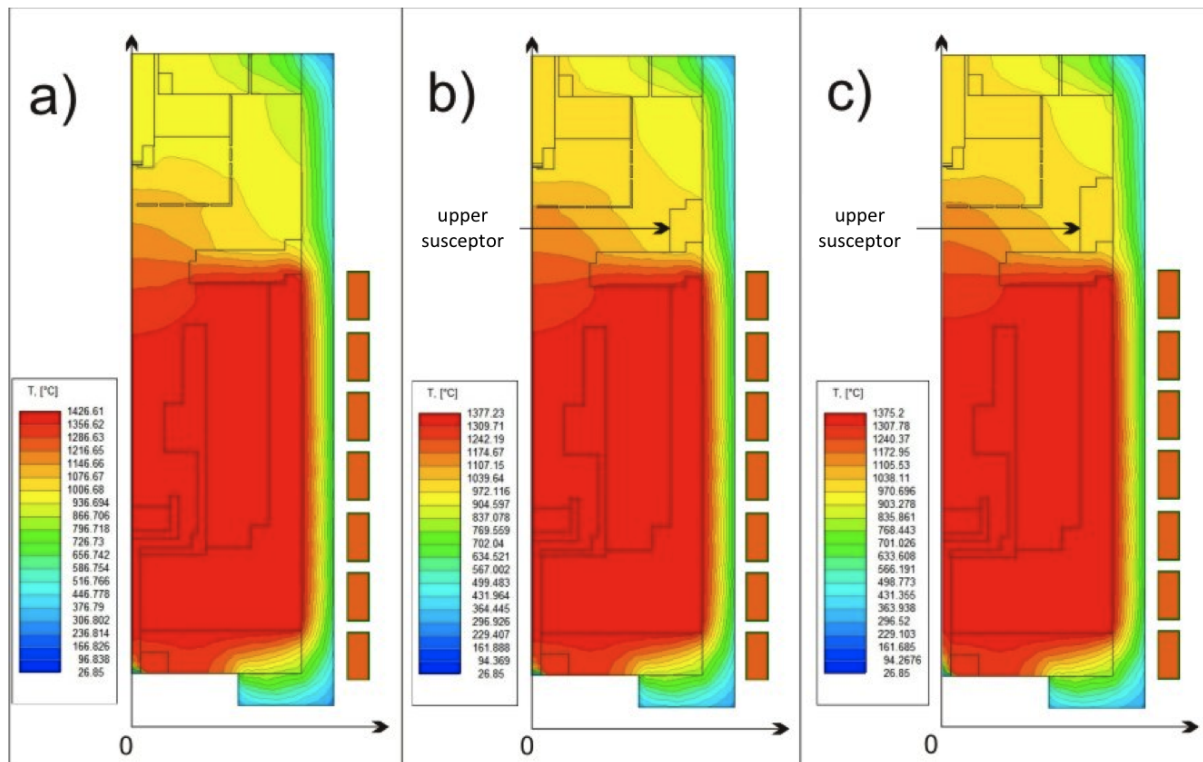


Figure 5.6.: Height of the upper susceptor: a) 0 mm,  $T_{source} = 1418 \text{ }^\circ\text{C}$ , b) 15 mm,  $T_{source} = 1370 \text{ }^\circ\text{C}$ , c) 30 mm,  $T_{source} = 1360 \text{ }^\circ\text{C}$

Fig. 5.7 shows that  $T_{source}$  decreases from  $1175 \text{ }^\circ\text{C}$  to  $1070 \text{ }^\circ\text{C}$  with coil position (axial distance of maximum induction area from the source) increasing from 50 to 100 mm, i.e. the higher vertical coil position, the lower temperature of the source is. This dependency

is one of the main disadvantages of the setup heated inductively with only one RF coil. Two separate induction zones interact with each other, though.

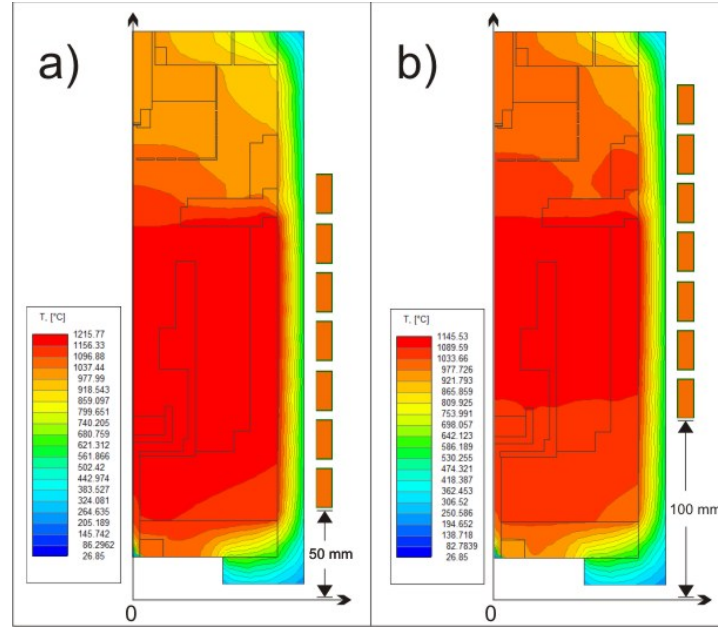


Figure 5.7.: a) Coil position 50 mm,  $T_{source} = 1175$  °C, b) Coil position 100 mm,  $T_{source} = 1070$  °C

Simulations of the temperature field distribution in the HEpiGaN software facilitated choice of the initial arrangement of the growth setup. Configuration presented in Fig. 5.6 c) was chosen as the starting point for experiments, with seed temperature of 1000 °C and temperature of the source at 1360 °C. Influence of the burning plasma on the seed temperature is described in Section 5.2.

### 5.1.2. MW plasma source

This subsection is focused mainly on the MW plasma source, yet the beginning of the subsection is intended to give a brief description of the software used for system modelling and network analyzer used for system characterisation. Components of the MW plasma source and principle of its operation are described. Resonant cavity is marked out, underlining the choice of appropriate building materials, in terms of their chemi-

cal stability to high temperature nitrogen plasma. Moreover, results of electromagnetic modelling of the cavity in CST Microwave Studio software are presented and conditions for plasma excitation are introduced.

CST Microwave Studio<sup>®</sup> (CST MWS) is software for the 3D EM simulation of high frequency components. It enables analysis of a wide range of high frequency devices such as antennas, filters, couplers, planar and multi-layer structures. The following modules are available within CST MWS, depending on the configuration: Frontend Module, Transient Solver Module, Transmission Line Matrix Method Solver, Frequency Domain Solver Module, Eigenmode Solver Module, Integral Equation Solver Module, Multilayer Solver, Asymptotic Solver Module. CST was used for designing and optimizing the microwave generation system. Further information on CST MWS software is to be found on <http://www.cst.com/>.

A network analyzer (NA) is an instrument that provides RF network measurements. It characterises the linear behaviour of either active or passive networks, devices or components. The HP 8753C model used together with the S-parameter test set HP85047A allows for measurements either from 3 MHz to 6 GHz or from 300 kHz to 3 GHz in a single sweep. It provides the capability to measure reflection and transmission characteristics, including scattering parameters (S-parameters) of two-port devices in either direction with a single connection. [155, 156] The HP 8753C network analyzer was utilised for measurements of  $S_{11}$  parameter, belonging to the S-parameters matrix. If we consider the following two-port network (Fig. 5.8) with  $\mathbf{a} = (a_1, a_2)$  as the waves travelling towards the two-port, and  $\mathbf{b} = (b_1, b_2)$  as the waves travelling away from the two-port, both waves are linked by the S-parameters matrix, while the focus was on the  $S_{11}$  parameter.

$$\begin{pmatrix} |b_1|^2 \\ |b_2|^2 \end{pmatrix} = \begin{pmatrix} |S_{11}|^2 & |S_{12}|^2 \\ |S_{21}|^2 & |S_{22}|^2 \end{pmatrix} \cdot \begin{pmatrix} |a_1|^2 \\ |a_2|^2 \end{pmatrix} \quad (30)$$

where:

$|a_1|^2$  - power wave travelling towards the two-port gate

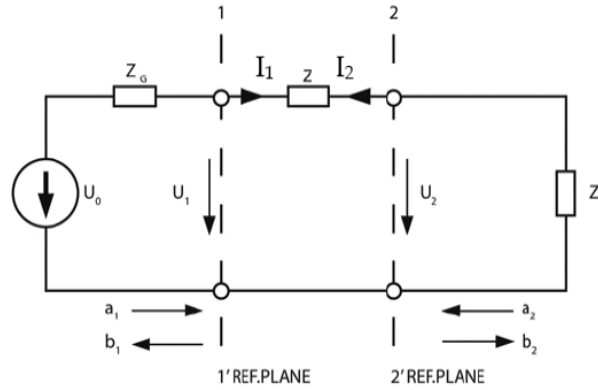


Figure 5.8.: Two-port network

$|b_1|^2$  - power wave reflected back from the two-port gate

$|S_{11}|^2$  - power reflected from port1

$|S_{12}|^2$  - power transmitted from port1 to port2

$|S_{21}|^2$  - power transmitted from port2 to port1

$|S_{22}|^2$  - power reflected from port2

The MW plasma source was developed in cooperation with Dr. A. Vodopyanov, from Institute of Applied Physics in Nizhny Novgorod, Russia. It comprises of remote magnetron head, microwave generator, 3-stub tuner, rectangular waveguides, microwave window, coaxial waveguide, slider and the resonance cavity. The magnetron head 2M266-M12WJ, delivered by IBF Electronic, produces a 2.45 GHz MW and sends it through a R-26 waveguide output. The device is water-cooled and equipped with a protection against reflected MW power [157]. A detector transmits information about the reflected power to a 3-stub tuner, which minimizes the reflected power by means of three mechanically movable stubs (Fig. 5.16). Control of the 3-stub tuner is realized with HomSoft – S-TEAM Homer Windows Visualization and Control Software [158], whereas communication with the MW generator is maintained via CAN Bus and PCAN view application from PEAK-SYSTEM TECHNIK GMBH. The MW generator is able to operate in continuous or pulsed mode with maximum power of 3 kW and 4 kW, respectively [157]. The MW power is transferred in the rectangular waveguide made of aluminium and enters

the reactor through a 20 mm thick quartz glass MW window, vacuum tight in the reactor wall. Subsequently, this power is transported inside the reactor by rectangular waveguide, transferred by a home-made R-26 coupler into the coaxial line, which ends in the resonant cavity, where nitrogen plasma is ignited. Two rectangular water-cooled flanges cool down the R-26 coupler. Coaxial waveguide consists of two molybdenum tubes and high-k dielectric tube in between. Alsint 99.7 was chosen to separate inner and outer conductor electrically, to maintain equal distance between both conductors along the coax and to prevent plasma formation between them. The physical properties of Alsint 99.7 are listed in the Appendix A, Section A.1. Apart from high volume DC resistivity at 20 °C, it has a maximum working temperature of 1700 °C. On the other hand, its thermal shock resistance is low.

The cylindrical resonant cavity is the crucial part of the MW plasma source. It defines not only the place of plasma ignition, but also the growth region. Dimensions and shape of the cavity were selected to obtain at 2.45 GHz the maximum electric field intensity just below the seed where the plasma ignition is expected to occur.

Results of modelling done by Dr. A. Vodopyanov, using CST MWS are depicted in Fig. 5.9.

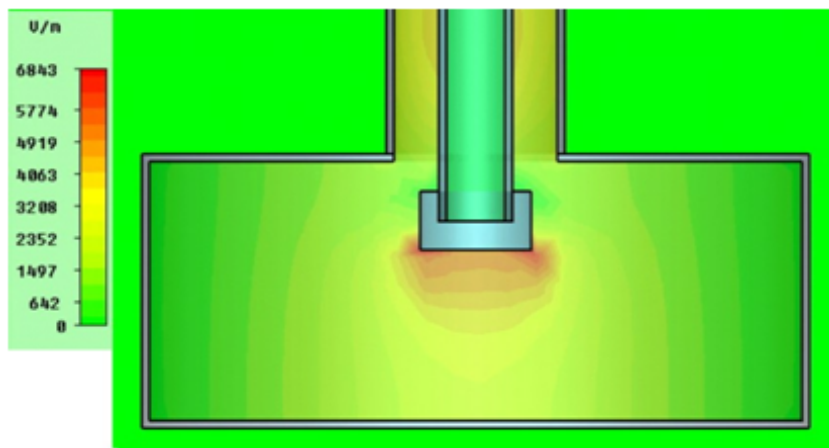


Figure 5.9.: Electric field distribution in the resonant cavity

The diameter equals 90 mm and the height  $h$  is adjustable in the range from 27 mm to 43 mm. Optical access to seed-holder and growth area is possible owing to a pattern of

## 5. Experimental - MW plasma enhanced growth

---

holes in the cavity's wall (Fig. 5.10a)). The hole diameter of  $d = 2r = 2$  mm guarantees that leakage of MW power from the cavity is not possible. Assuming that conditions for propagation of MW through the hole in the metal cavity can be approximated by MW propagation through cylindrical waveguide, one can calculate the lower cut-off frequency  $f_c$  of TE ground mode with the following equation

$$f_c = \frac{1.8412}{2\pi r \sqrt{\mu\epsilon}} = \frac{1.8412c}{2\pi r} \quad (31)$$

where:  $c$  - speed of light,  $r$  - radius of the circular cross-section of the waveguide and 1.8412 is the root of the first derivative of a Bessel function. The lower cut-off frequency for  $d = 2$  mm equals  $\approx 87.91$  GHz that is much above 2.45 GHz, frequency at which MW power is transferred into the cavity.

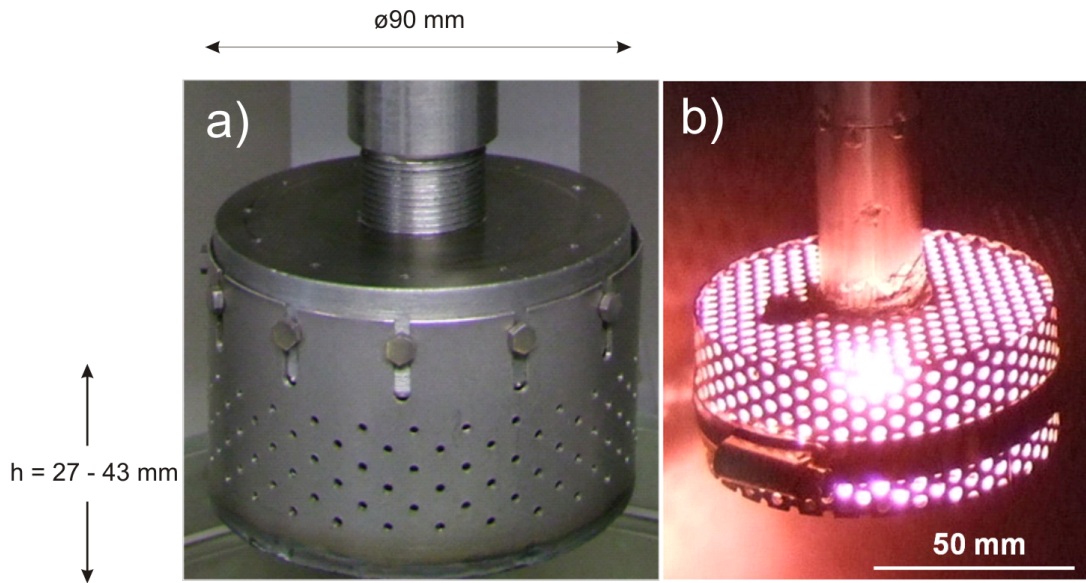


Figure 5.10.: a) cylindrical resonant cavity made of molybdenum foil, b) aluminium resonant cavity in operation at RT,  $p = 8$  mbar

When choosing material of the cavity, the following requirements were taken into consideration:

1. maximum operation temperature as high as 1500 °C,
2. resilience to Ga vapour (not alloying with Ga),



3. resilience to nitridation process by excited nitrogen,
4. high electric conductivity (min.  $1 \times 10^6 \text{ } [\Omega\text{m}]^{-1}$ ),
5. good machinability,
6. low sputtering coefficient.

Physical data of refractory metals are collected in Tables 5 and 6 in the Appendix A (Section A.2), and in Figures 5.11 and 5.12.

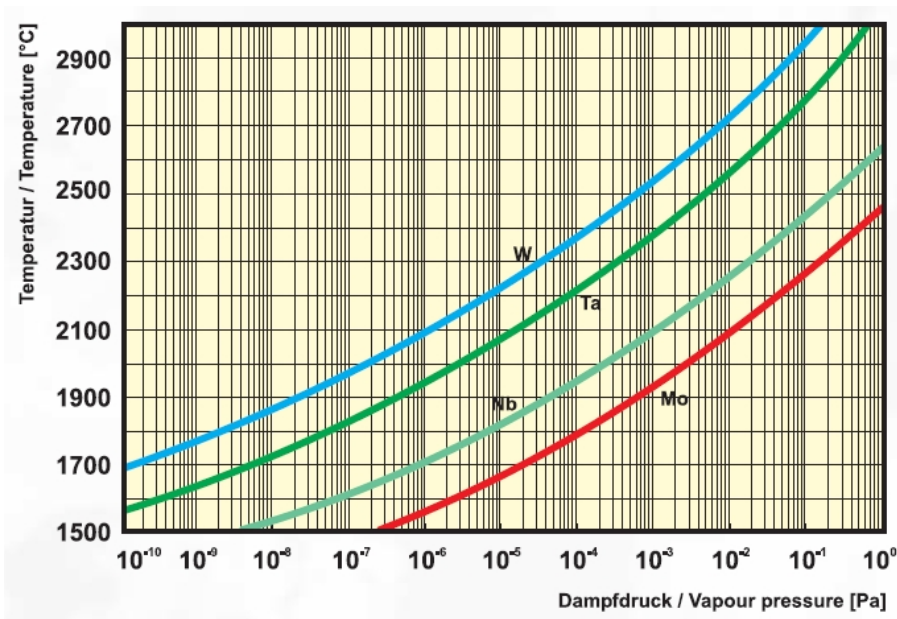


Figure 5.11.: Vapour pressure of refractory metals [159]

All the materials listed in Table 5 have a melting temperature  $T_m$  above the maximum operation temperature. Due to their resistance to nitrogen, molybdenum (Mo) and tungsten (W) have the substantial advantage over niobium (Nb), tantalum (Ta) and titanium (Ti). The evaporation rate of W and its vapour pressure are approximately five orders of magnitude smaller than in case of Mo. Nevertheless, Mo was the first choice material for cavity manufacturing. The decisive factor was its resistance to nitrogen as well as better machinability and weldability. The resonant cavity, made of Mo is depicted in Fig. 5.10. From the top it is closed by a Mo flange, with an opening for

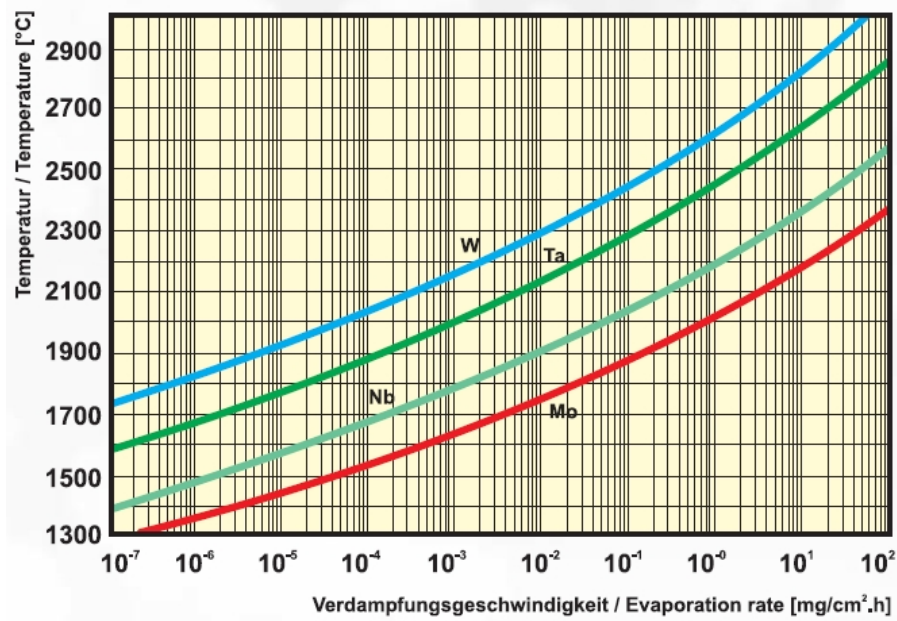
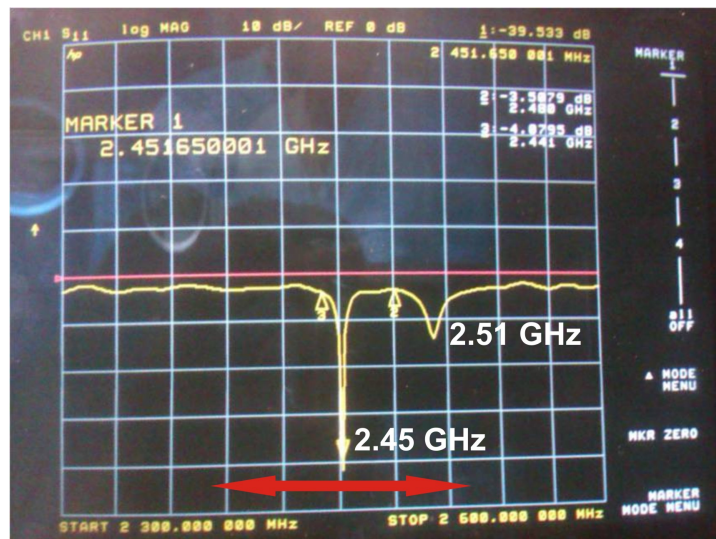


Figure 5.12.: Evaporation rates of refractory metals [159]

a coaxial waveguide. Twelve vertical slits in the cavity's side wall and twelve screws equally distributed along the flange side wall are used for adjustment of the cavity's height. Before the Mo cavity was constructed, cavity made of Ti had been utilised, as a quick, temporary solution. It was a short-lived cavity, since Ti is not resistant to nitrogen above 540 °C, it was nitrided after few experiments and eventually its walls cracked. The MW plasma source was designed with the intention to ignite nitrogen plasma in the resonance cavity. Still, a precise adjustment of the system is required before each experiment. It is carried out in the configuration nr 1, when instead of the magnetron head and 3-stub tuner, the NA is connected to the waveguide. The NA was employed to measure the  $S_{11}$  parameter as function of frequency around 2.45 GHz. To match the cavity with the working frequency of the MW generator, the  $S_{11}$  minimum of the standing wave was adjusted to 2.45 GHz. View of the network analyzer display while performing measurements of  $S_{11}$  parameter is depicted in Fig. 5.13.

The resonance peak in Fig. 5.13 is already very close to the optimum position, with its minimum at 2.4516 GHz,  $S_{11}$  value of -39.5 dB. It means that only 1.06% of power would be reflected at 2.4516 GHz. The resonance peak with lower intensity at around 2.51 GHz

Figure 5.13.:  $S_{11}$  parameter vs frequency

is caused by a parasitic standing wave either in the ceramic tube or somewhere inside the waveguide. Red horizontal arrow shows directions in which resonance peak can be shifted during the adjustment by changing the height and vertical position of the cavity. Therefore, cavity top flange and outer tube of the coaxial waveguide are connected via thread. While moving the cavity along the vertical axis, distances between the seed-holder and cavity change (see Fig. 5.14).

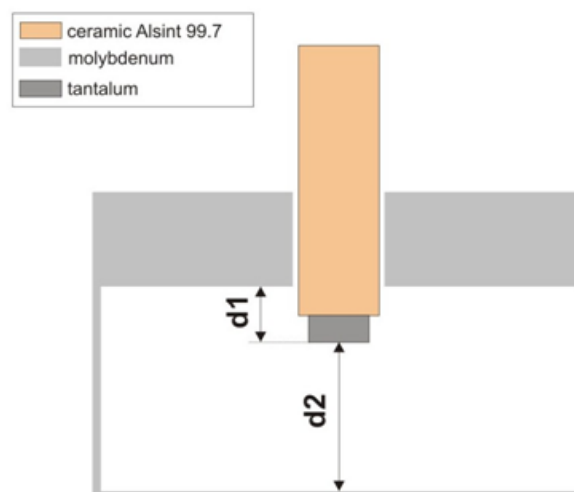


Figure 5.14.: Distances in the cavity

The fine position of the resonance peak depends on the distances  $d_1$  and  $d_2$ . When increasing distance  $d_2$ , resonance peak is shifted to higher frequencies. The maximum value of  $d_2$  is limited by the distance  $d_1$  between the seed-holder and the flange. If distance  $d_1$  is too small, the probability of electrical breakdown between the seed-holder and the flange gets too high, preventing plasma ignition under the seed-holder. Once the resonance peak is set at the proper frequency of 2.45 GHz, it needs to remain there until plasma is ignited in the cavity. This requires the mechanical stability of the microwave plasma generation system. The set distances  $d_1$  and  $d_2$  cannot alter during the following preparation stages: reconfiguration of the system – from configuration nr 1 to configuration nr 2 (detaching NA and connecting magnetron head), closing reactor door and pumping down the reactor. Demand for mechanical stability resulted in certain design approaches, which are briefly described below. Mechanical connections between Mo waveguide, coaxial outer tube and cavity flange have threads, as well as the one between inner coax tube and the seed-holder. Moreover, counter nut is used to prevent self loosening of the cavity and its displacement along the vertical axis, whereas cavity walls are attached to the flange by means of twelve screws (Fig. 5.10a)). Apart from the position of  $S_{11}$  minimum (resonance peak) within the frequency range, the total pressure in the reactor is another parameter for plasma ignition. Optimum pressure for plasma ignition in nitrogen atmosphere was found experimentally, considering the dependence of breakdown electric field for air vs pressure (Fig. 3.1), which is an analogy to the Paschen curve for DC discharges (see Section 3.1 for details). In our setup this pressure for 2.45 GHz MW plasma ignition at room temperature (RT) was experimentally found to be around 8 mbar, although in Fig. 3.1 minima of theoretical and experimental  $E_b$  curve lay at 2.5 mbar and 4 mbar, respectively. This deviation can arise from the difference in properties of air and nitrogen, which are described by values of gas constants A and B, used in the expression for Paschen law (see equation 12).

Appropriate actions for MW plasma excitation are setting the resonance frequency of the cavity at 2.45 GHz, connecting the magnetron head to the MW plasma excitation line and closing the reactor door and pumping down. The reactor is each time pumped

Table 2.: The gas-specific constants A and C of Townsend's first ionization coefficient.  
Valid in the range  $C/2 \leq E/p \leq 3C$  [98]

Gas	A [ion pairs $\text{m}^{-1}\text{Torr}^{-1}$ ]	C [V $\text{m}^{-1}\text{Torr}^{-1}$ ]
air	1220	36500
nitrogen	1060	34200

down to  $\sim 5 \times 10^{-5}$  mbar and then filled up with nitrogen. This procedure is repeated twice before setting the total pressure to 8 mbar. The output power of magnetron head is set to 300 W and nitrogen plasma is ignited inside the cavity (see Fig. 5.15), while the power supply is in continuous operating mode and all the three tuner's stubs are in absolute, mechanical zero position, i.e. they do not dive into the waveguide (Fig. 5.16). Finally, the reactor is filled with nitrogen at a rate of 20 slm to reach the desired pressure in the 200 - 800 mbar range. Auto tuning operation mode of 3-stub tuner is turned on, when the total pressure in the reactor reaches 100 mbar. Auto tuning means automatic matching of generator impedance and impedance of the load. It is based on the indirectly obtained load reflection coefficient at the load plane (see Fig. 5.16). At lower pressures wave impedance of the plasma is too small for the auto tuner to detect it. Without load, auto tuning leads to plasma extinction.

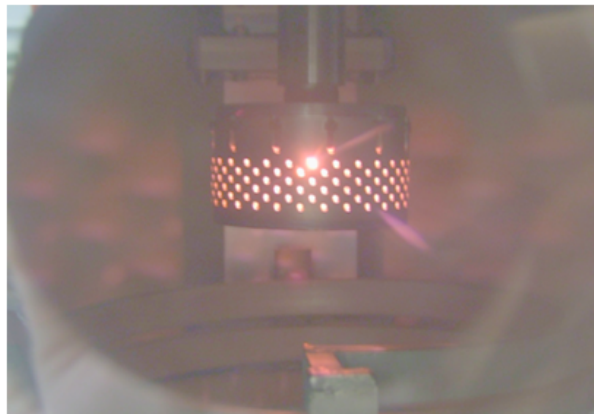


Figure 5.15.: Burning plasma in a Ti test-cavity, at 8 mbar

Stability of microwave plasma and its dependence on temperature is discussed in the following Section 5.2.

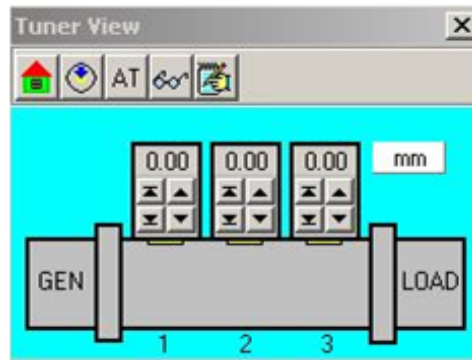


Figure 5.16.: The cross section of the auto-tuner. Stubs denoted as 1, 2, 3 are at absolute, mechanical zero position

## 5.2. Stability of MW plasma

Prerequisite for long time growth experiments is a stable MW plasma operation. Otherwise, lack of reactive nitrogen in the vicinity of the seed, at growth temperature, leads to GaN decomposition. It was shown by Choi et al. [61] that at temperatures above 900 °C in N<sub>2</sub> atmosphere significant decomposition of GaN occurs. Outcome of growth experiments carried out under non-stable plasma operation is elucidated in Section 5.5. Stable MW discharge is preceded by plasma ignition inside the resonant cavity. Proposed GaN crystal growth calls for nitrogen plasma excitation just below the seed-holder and its sustainment requires an effective MW power coupling into the burning plasma itself (compare power absorption in a MW field in Section 3.1). The auto tuner can guarantee minimization of the reflected power, measured at the incident plane, but does not assure that plasma burns in the right position or as a volume discharge either. Additionally, visual observation, seed temperature measurement and optical emission spectra are used to confirm stable plasma operation. In the low temperature range (until 600 °C) direct visual observation is possible, whereas above 600 °C black body radiation makes it impossible to distinguish light emitted by plasma from light emitted by hot elements of the growth setup. Since operation of the pyrometer starts at 800 °C [161], seed temperature is no useful indicator below this temperature. The most comprehensive tool to confirm the right position of burning plasma in this setup is OES. It is able to measure plasma

spectra in the whole heater temperature range, utilised during the growth process. Dependence of microwave plasma on the temperature of the cavity and seed-holder turned out to be crucial in terms of stable plasma operation. This dependency may hinder long term growth experiments. Since the cavity is made of metal, its dimensions increase with increasing temperature.

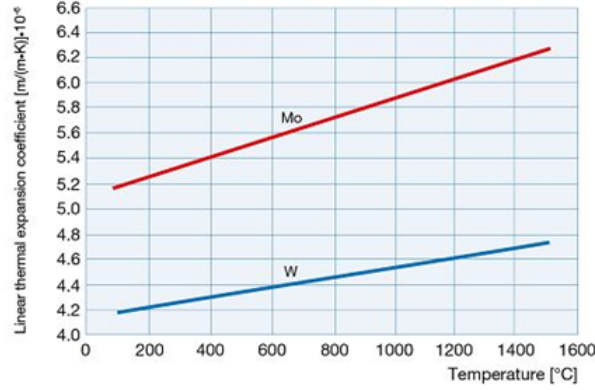


Figure 5.17.: Thermal expansion coefficient for molybdenum and tungsten [162]

In Appendix B, Section B.1 the interpolation formula for the linear thermal expansion coefficient for Mo within RT – 1500 °C range is derived from coefficients given in [162].

$$\alpha_L = 0.075 \times 10^{-8} [m/mK^2] \times T [^\circ\text{C}] + 5.1 \times 10^{-6} [m/(mK)] \quad (32)$$

Change of the cavity diameter  $D$  while heating up from RT ( $D = 90 \text{ mm}$ ) to 1330 °C is calculated using formula 33 in Appendix B, Section B.2 and equals  $\Delta D = 0.656 \text{ mm}$

$$\Delta D = D \int_{T_1}^{T_2} \alpha_L \cdot \Delta T \quad (33)$$

On the other hand, it was experimentally proven that by heating up the cavity to 1330 °C, resonance frequency is decreased from  $f_r = 2.45 \text{ GHz}$  by  $\Delta f_r = 0.049 \text{ GHz}$  (Fig. 5.18). By comparing those values one can speculate about the reasons of the resonance frequency alteration. If shift of resonance frequency depends only on the change of the cavity dimensions, then relative change of the cavity dimensions should equal that of resonance frequency  $f_r$ , according to the formula 34.

$$\frac{\Delta D}{D} = \frac{\Delta f_r}{f_r} \quad (34)$$

$$\Delta D = D \cdot \frac{\Delta f_r}{f_r} = 1.8 \text{ mm} \quad (35)$$

$$\Delta f_r = f_r \cdot \frac{\Delta D}{D} = 0.0179 \text{ GHz} \quad (36)$$

The above estimations show that such a substantial change of  $f_r$  as 0.049 GHz is caused not only by the change of cavity dimensions due to thermal expansion. If it was the case, then instead of 0.656 mm the change of cavity diameter should be 1.8 mm. But the elongation of the inner tube of coaxial line with the seed-holder causes additional shift of  $f_r$ . As the temperature increases, the distance  $d_2$  in Fig. 5.14 between the bottom of the cavity and the bottom surface of the seed-holder decreases. As a result,  $f_r$  shifts to lower values, comparable with adjusting  $f_r$  by moving the cavity upwards (compare with cavity tuning, described in Subsection 5.1.2). With the same equations as for the cavity diameter change the approximate elongation of the inner coaxial Mo tube with tantalum seed-holder was estimated. It was assumed that the Ta seed-holder has the same linear thermal expansion coefficient as Mo. Introduced error is negligible, as the seed-holder thickness of 4 mm is much smaller than the inner coaxial Mo tube length of 225 mm. With the total length  $L_{RT} = 229$  mm one gets  $\Delta L = 1.67$  mm. In Appendix B, Section B.3 estimations of the influence of the axial position of the seed-holder on the  $f_r$  of the cavity are presented. Based on experimental results,  $f_r$  shift per 1 mm shift of the seed-holder was estimated as  $\Delta f_r / 1 \text{ mm} = 0.0092 \text{ GHz/mm}$ . The 1.67 mm elongation of the inner coaxial tube results in a 0.0192 GHz change of the resonance frequency. Summarizing, 0.0179 GHz shift from the change of cavity diameter, 0.0192 GHz from elongation of the inner coaxial tube and additional influence of the thermal expansion of the cavity's bottom wall and of ceramic Alsint 99.7 tube have to be considered to explain the measured 0.049 GHz shift.

During cooling down  $f_r$  shifts back to the initial value. Fig. 5.18 presents the change



of  $f_r$  as function of source temperature, which is in this experiment related to the seed temperature by  $T_{seed} \approx T_{source} - 330$  °C. NA measurements were taken in configuration nr 1, with RF heating on. At  $T_{seed} \approx 1000$  °C the resonance peak was shifted as mentioned above by 0.049 GHz to 2.401 GHz. Such substantial shift causes strong plasma fluctuations, its displacement to the coaxial line or even its complete extinction.

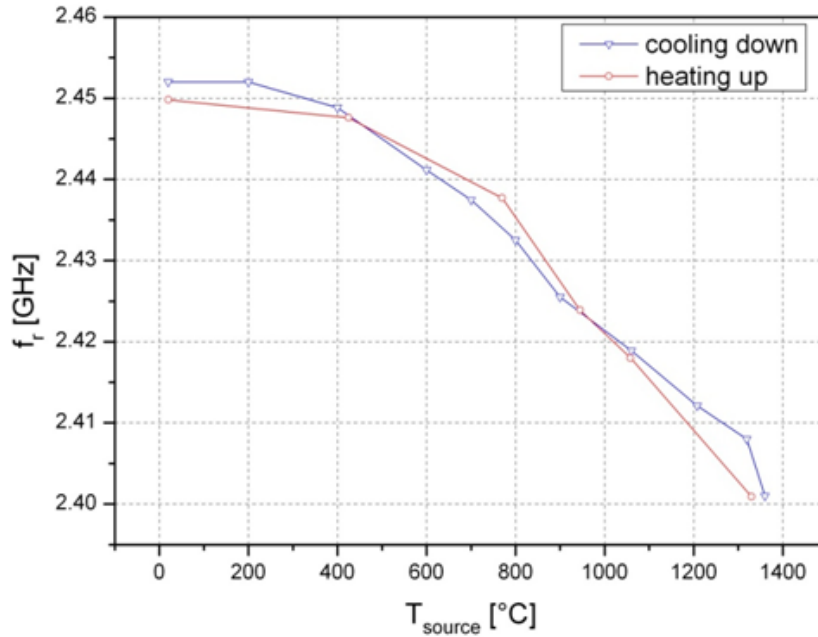


Figure 5.18.: Resonant frequency of the cavity vs  $T_{source}$

Complete plasma extinction is easily noticeable, as magnetron is turned off automatically and an error is reported. Plasma instabilities require other monitoring methods, as already mentioned in the introduction to this section. The seed is heated up by plasma and therefore its temperature can be utilised as a monitoring parameter above 800 °C, the minimum operation temperature of pyrometer. Fig. 5.19 presents influence of ignition and burning of microwave plasma in the cavity, centrally below the seed. Microwave power is set to 300 W. In this case the seed temperature, marked with a red line, rises of about 100 °C. Fig. 5.20 is complementary to Fig. 5.19. It shows decrease of the seed temperature, when plasma moved from the cavity to the coax end. Temperature decrease is much steeper and faster, than in case of turning off the induction heating, as

## 5. Experimental - MW plasma enhanced growth

presented in Fig. 5.21, which displays temperature curve, measured during the cooling phase of the process, when plasma was still burning in the cavity. Blue lines in the graphs represent the seed temperature to be obtained. In Fig. 5.19 it equals 1000 °C initially and then 1050 °C, in Fig. 5.20 desired temperature was first set to 1000 °C and then 950 °C, whereas in Fig. 5.21 it was set to 950 °C.



Figure 5.19.:  $T_{seed}$  vs  $t$ . Plasma ignited in the cavity

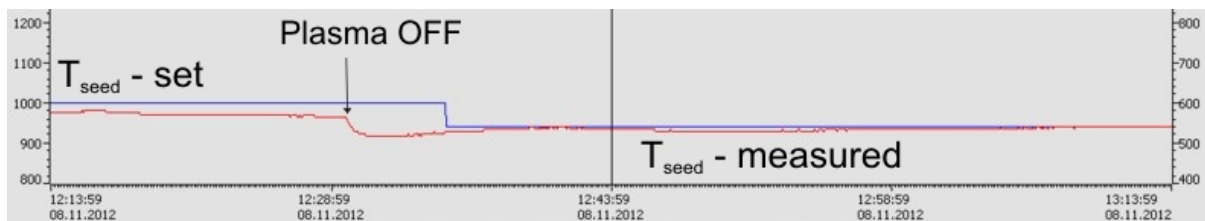


Figure 5.20.:  $T_{seed}$  vs  $t$ . Plasma started burning outside the cavity

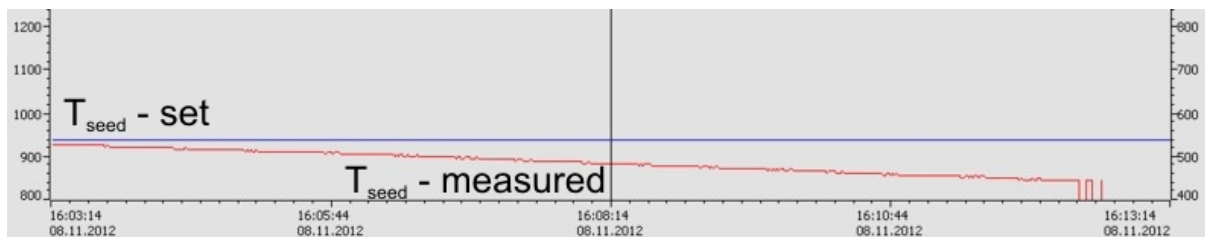
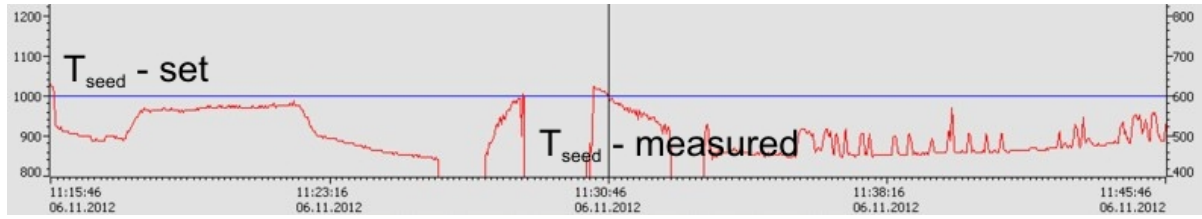


Figure 5.21.:  $T_{seed}$  vs  $t$ . After turning the induction heating off

Considerable impact of plasma instabilities on  $T_{seed}$  is visible in Fig. 5.22.  $T_{seed}$  was measured during unstable plasma operation inside the cavity. Discharge type was changing between homogeneous microwave one and arc-like.

Visual observations were possible through a window in the reactor and through holes in the cavity, graphite heater and felt. The front sapphire window of the reactor provides

Figure 5.22.:  $T_{seed}$  vs t. Unstable plasma operation

insight into the reactor, whereas additional ILMADUR borosilicate glass I-420 protects against UV light [163]. Direct observation is the fastest method to assess whether plasma is ignited in the right position or burns somewhere outside the cavity. Furthermore, it allows judge the form of plasma. The most favourable one would be homogeneous plasma, occupying a volume of few cubic centimetres just below the seed-holder, on the way of Ga vapour, transported by  $N_2$  carrier gas from the Ga crucible. On the contrary arcing definitely should be avoided. This phenomenon can cause etching of the already grown layer, sputtering of the cavity material and contribute to layer contamination [164, 165].

### Dependence on pressure

The dependence of plasma on total reactor pressure  $p_{tot}$  in terms of effective temperature of its electrons  $T_e$  and gas (atoms and molecules particles)  $T_g$  was described in Subsection 3.2. Within the pressure range used in our process (8 mbar – 800 mbar), plasma is denoted as hot, so that  $T_g \approx T_e$ . After successful plasma ignition at around 8 mbar, pressure is increased to reach a value within 200 – 800 mbar range. The higher  $p_{tot}$  in the reactor, the more MW power is needed to sustain the discharge. Mean free path of electrons decreases with pressure. Hence electrons have less time to gain energy for ionization of neutral particles. Operation at higher power levels results in increased plasma temperature, followed by an increase of the seed temperature.

### 5.3. Advantages of nitrogen plasma over ammonia

This section underlines the advantages of utilising nitrogen plasma rather than  $\text{NH}_3$ , as a source of reactive nitrogen. Discussion is based on observations made during  $\text{NH}_3$ -based vapour growth of GaN in a classical growth setup (Fig. 2.7) as well as during processes conducted in the reactor equipped with a plasma-activated nitrogen source (Fig. 5.3).  $\text{NH}_3$  readily reacts with molten Ga and carbon. The typical result in systems containing graphite, is the crust formation on the top of Ga source. If the sublimation process of this solid GaN layer, heavily contaminated with carbon, is too slow, then blocking mechanism finally prevails, leading to the growth cessation. On the contrary, nitrogen microwave plasma, being restricted to the resonance cavity, does not come into contact with molten Ga. Figures 5.23 a) and b) compare the top surface of molten Ga after 4 h growth experiment, in the classical  $\text{NH}_3$ -based approach and microwave plasma-based one, respectively.

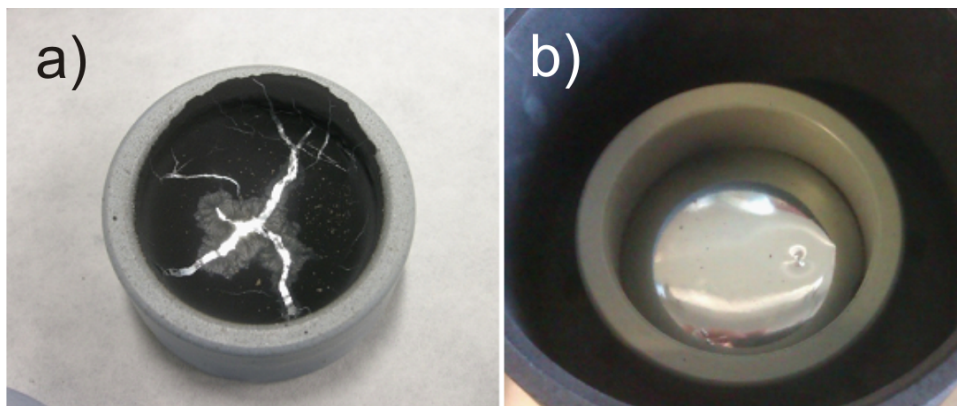


Figure 5.23.: Ga source after 4 h growth experiment with: a) ammonia, b) microwave plasma

In Fig. 5.23 a) the Ga surface is completely covered by crust, containing carbon that comes from graphite parts of the setup (see Fig. 5.3). It implies that Ga evaporation was severely reduced (or stopped completely) during the growth, making it impossible to control physical vapour transport of Ga to the growth region. Surface of Ga in Fig. 5.23 b) is clear and shiny. In this case no crust hindering Ga evaporation was observed. Reaction of  $\text{NH}_3$  with liquid Ga may be so violent, that emerging Ga droplets are hurled

to the seed. Deposited on the seed, they result in growth of polycrystalline GaN (see [60] and the references therein). Fig. 5.24 depicts Ga droplets in the Ga source, after NH<sub>3</sub>-based growth experiment.

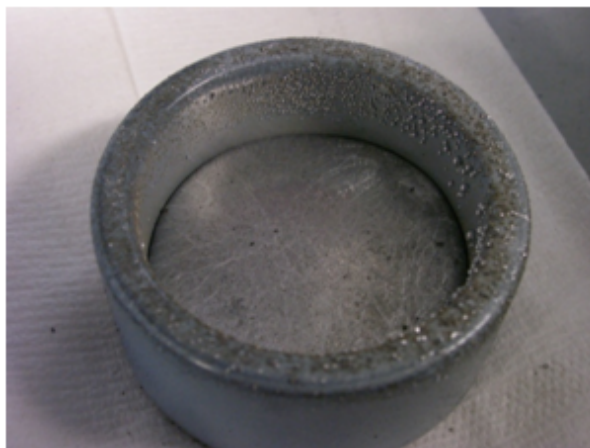


Figure 5.24.: Ga droplets in the Ga source

Replacing NH<sub>3</sub> with nitrogen plasma facilitates construction of the lower part of the setup, in the vicinity of the Ga source. There is no further need for use of diaphragm, whose main task would be to decompose ammonia, before it reaches the Ga source. However, diaphragm can be useful in terms of achieving laminar flow of nitrogen carrier gas. In plasma-based setup, the role of nitrogen carrier gas is limited to enhancing transport of Ga vapour to the growth region. It does not need to counteract NH<sub>3</sub> flow towards the Ga source. When considering growth parameters, additional degree of freedom is gained over NH<sub>3</sub>-based process.

Foremost issue related with implementing NH<sub>3</sub> in the growth setup, is its instability, which puts limits to plausible growth parameters and choice of the setup building materials. Since NH<sub>3</sub> is thermally unstable at elevated temperatures, it limits the growth temperature, as it was described in Subsection 2.2.1. At high temperatures, above 1000 °C dominates thermal decomposition of NH<sub>3</sub> into N<sub>2</sub> and H<sub>2</sub>. The dissociation of NH<sub>3</sub> is additionally enhanced by Al<sub>2</sub>O<sub>3</sub> and Ga, among other materials. Large surface of Al<sub>2</sub>O<sub>3</sub> catalyses decomposition process, reducing furthermore maximum usable growth temper-

ature [166].  $H_2$  is one of the products of  $NH_3$  dissociation, which in large amounts is undesirable in a system meant for GaN growth. It enhances etching of GaN surface [167].

Besides, gaseous  $NH_3$  is aggressive and causes degradation of parts containing carbon. In this way, lifetime of graphite parts of the setup is reduced. Reaction of  $NH_3$  with graphite produces HCN molecules, high temperature stable carriers of nitrogen. Consequently, chemical vapour transport (CVT) takes place, as Ga is transported by GaCN to the seed [14]. Fig. 5.25 a) presents graphite parts attacked by  $NH_3$  at temperatures around 1050 °C [14], whereas Fig. 5.25 b) depicts graphite susceptor used in nitrogen microwave plasma-based, ammonia-free setup.



Figure 5.25.: Graphite susceptor a) attacked by  $NH_3$  b) after microwave plasma enhanced experiment

## 5.4. Study on Ga vapour

The Ga source is located in the lower part of the growth setup (see Fig. 5.3). It is a graphite crucible covered with p-BN layer and filled with liquid gallium. Evaporation of Ga is possible owing to energy radiated by the inductively heated susceptor. Therefore,

Ga is delivered to the growth region as vapour and such transport is known as physical vapour transport (PVT). Consequently, growth of GaN nitride single crystalline layers described in this thesis can be denoted as combination of Ga PVT with chemical vapour deposition (CVD). In this subsection Ga vapour is studied during the “PVT + CVD” process. The influences of  $p_{tot}$  in the reactor on the Ga vaporization, as well as the super-saturation of Ga vapour are discussed. Finally Ga vapour excitation and its interaction with MW plasma are discussed.

### 5.4.1. Ga supply and super-saturation

Ga evaporation rate depends on  $p_{tot}$  in the reactor, nitrogen carrier gas flow and on temperature of Ga source  $T_s$ , according to the well-known Arrhenius law

$$M = Ae^{-E_v/RT} \quad (37)$$

where:  $M$  - rate constant,  $R$  - universal gas constant,  $T$  - absolute temperature in K,  $A$  - pre-exponential coefficient, and  $E_v$  - evaporation energy. The logarithm of the Equation 37 gives a linear function for determination of  $E_v$

$$\ln(M) = \ln(A) + \frac{-E_v}{R} \frac{1}{T} \quad (38)$$

Data of vapour pressure of Ga reported by [168, 169] are higher from those published by Cochran and Foster [170]. The discrepancy is due to formation of  $\text{Ga}_2\text{O}(v)$  in the reaction of Ga with quartz [171]. Harteck [168], Speiser and Johnston [169] employed the Knudsen method with quartz effusion cell, whereas Cochran and Foster [170] used an effusion cell made of alumina. Siche et al. [172] reported use of some quartz part inside the reactor, which could be the reason for difference between the calculated evaporation energy 284 kJ/mol and the data from literature 270.3 kJ/mol [173]. Detailed study on Ga evaporation in the inductively heated PVT reactor within sub-atmospheric pressures was carried out by Fizia [174] and subsequently continued by the author. The Ga loss was measured by comparing the difference of Ga source weight before and after the

experiment. Measurements were taken with Faust FA 3100-2iCE balance, its accuracy is  $\pm 10$  mg. In the whole series of experiments the evaporation time was constant 4 h. The evaporation increases with  $T_{source}$  (Fig. 5.26). Additionally, the expected evaporation increases with decrease of  $p_{tot}$ , because the physical barrier for vaporization of liquid Ga into the vapour phase is lowered.

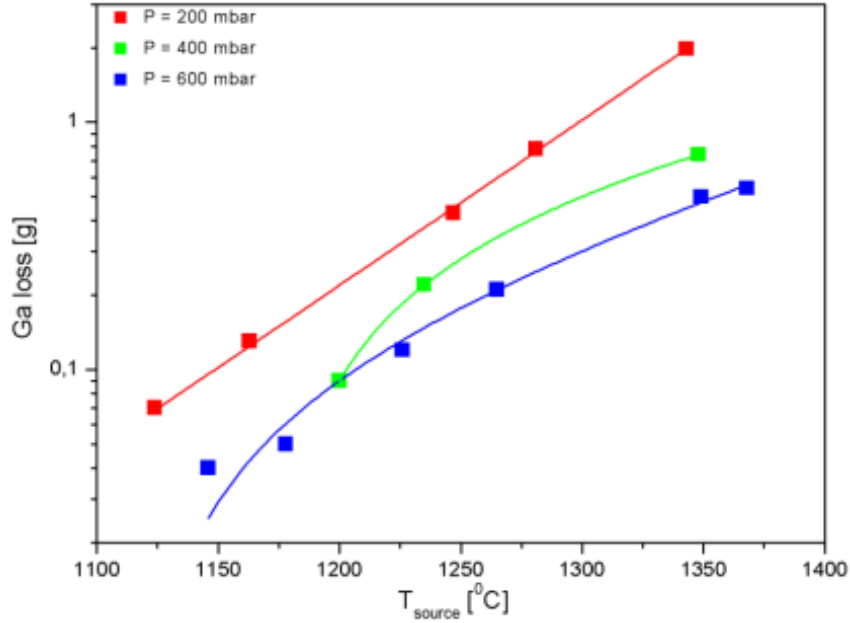


Figure 5.26.: Ga loss vs  $T_{source}$ . Nitrogen carrier gas flow set to 200 sccm [174]

The dependency of the Ga evaporation rate on temperature, carrier gas flow and total pressure limits the applicable parameters range for growth of GaN from the vapour phase. It constrains the temperature of the Ga source.

The desired minimum  $T_{source}$  can be derived from Fig. 5.27, assuming that all the evaporated Ga is deposited on the seed. For instance, in case of 4 h growth, with a growth rate of 10  $\mu\text{m}/\text{h}$ , substrate diameter of 2 cm and 200 sccm carrier gas flows, the minimum  $T_{source}$  equals 1120 °C, as it was read out from Fig. 5.27 for 65 mg of evaporated Ga, calculated using the following equation:

$$\Delta m_{Ga} = \frac{M_{Ga}}{M_{Ga} + M_N} \cdot \frac{\pi}{4} d^2 h \rho_{GaN} \quad (39)$$



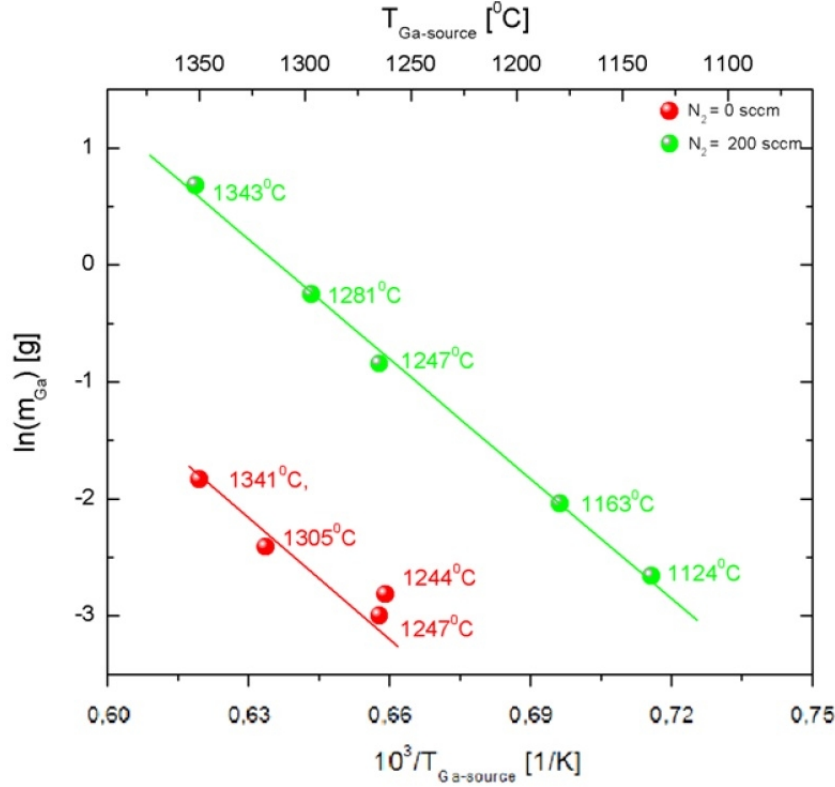


Figure 5.27.: Ga loss vs  $T_{\text{source}}$  for  $p = 200$  mbar [172]

with molar masses  $M_{\text{Ga}} = 69.72$  g/mol,  $M_{\text{N}} = 14.007$  g/mol and GaN density at 300 K  $\rho_{\text{GaN}} = 6.15$  g/cm<sup>3</sup>.

The control of Ga PVT to the growth region and concurrently control of the Ga vapour supersaturation in the growth setup is one of the prerequisites to grow GaN single crystals. Deviation from the thermodynamic equilibrium, either supercooling (the deviation of temperature  $\Delta T$ ) or supersaturation (the deviation of pressure  $\Delta p$ ) is the precondition for the formation of a new phase.

The classical theory of nucleation as developed by Gibbs [1928], Volmer [1926, 1939], Stranski and Kaischew [1934] and, Frenkel [1955] is valid at small or moderate supersaturation [175]. Vapour phase epitaxy (VPE) with typical values of the relative supersaturation between  $\sigma_{\text{VPE}}^* \approx 0.5 - 2$  [176] falls into this category. In supersaturated homogeneous systems a new phase appears as a result of the competition between the thermodynamic driving force  $\Delta\mu$  (the difference in chemical potential by supersatura-

tion) and the interface free-energy effects that strive to minimize the total crystal surface area, and leads to a change of the Gibbs free energy upon the creation of a droplet or nucleus

$$\Delta G(r) = \Delta G^V + \Delta G^{IF} = -\frac{4\pi r^3}{3v_l} \Delta\mu + 4\pi r^2 \sigma \quad (40)$$

where  $\Delta G^V$  is associated with increasing volume of the new particle,  $\Delta G^{IF}$  stands for the expenditure of energy required for increase of the droplet surface,  $r$  is radius of the droplet,  $v_l$  is the molecular volume of the new liquid phase and  $\sigma$  is the surface energy. The Equation 40 is plotted in Fig. 5.28. It displays a maximum at the critical radius  $r = r^*$ , beyond this the nucleus can further grow. The critical radius  $r^*$  is given by

$$r^* = \frac{2\sigma v_l}{\Delta\mu} \quad (41)$$

and the corresponding critical nucleation energy is

$$\Delta G^* = \frac{16\pi}{3} \frac{\sigma^3 v_l^2}{(\Delta\mu)^2} \quad (42)$$

which is the energy barrier to be overcome for condensation to take place. [27, 175, 176]

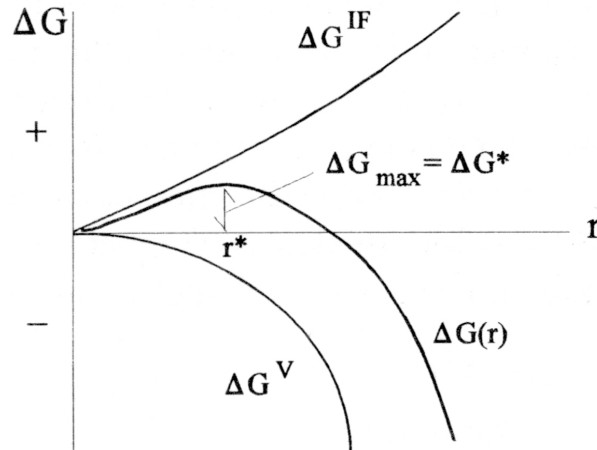


Figure 5.28.: Change of the Gibbs free energy vs radius of the droplet [176]

As it is visible from Equations 41 and 42, both the critical radius  $r^*$  and the critical

nucleation energy  $\Delta G^*$  decrease with the increase of the supercooling  $\Delta T$  (as  $\Delta\mu \sim \Delta T$ ).

The nucleation rate  $J$  increases with the decrease of the critical nucleation energy  $\Delta G^*$  (Equation 43). Consequently higher supercooling results in faster nucleation.

$$J_r = A \exp(-\Delta G^*/kT) \quad (43)$$

where  $A = f(T)$  is a system dependent constant. The critical nucleation energy  $\Delta G^*$  can be lowered not only by the increase of supercooling, but also by the application of a substrate. Such heterogeneous nucleation is usually encountered in single crystal growth. Substrates, reactor walls and impurity particles serve as catalytic agents for the reduction of nucleation work [176]. The critical nucleation energy  $\Delta G^*$  in the heterogeneous nucleation is described by the following equation

$$\Delta G_{het}^* = \Delta G_{hom}^* \cdot f(\Theta) \quad (44)$$

where  $f(\Theta)$  is the function of the wetting angle  $\Theta$

$$f(\Theta) = 1/4[(1 - \cos\Theta)^2(2 + \cos\Theta)] \quad (45)$$

Fig. 5.31 schematically presents the dependency of type of deposit on the degree of the Ga vapour supersaturation. One can see that the Ga vapour supersaturation limits the growth window. When the supersaturation is too low, crystallization does not occur. On the other hand, when the critical degree of supersaturation is exceeded, polycrystalline material is grown, as depicted in Fig. 5.29, showing a polycrystalline GaN layer grown on the  $\text{Al}_2\text{O}_3$  seed after 5 h growth. The average growth rate was estimated to be 6  $\mu\text{m}/\text{h}$ .

Ga supersaturation can also result in the formation of Ga droplets, which prevent further growth of GaN single crystalline layers. Gallium in excess enhances GaN decomposition. Schoonmaker et al. [45] showed that Ga can act as catalyst for the GaN vaporization. It may damage crystal structure, so that nitrogen atoms are able to leave their positions, diffuse through liquid Ga surface, form nitrogen molecules and evaporate. Therefore, too high amount of Ga can not only deteriorate the GaN seed, but also

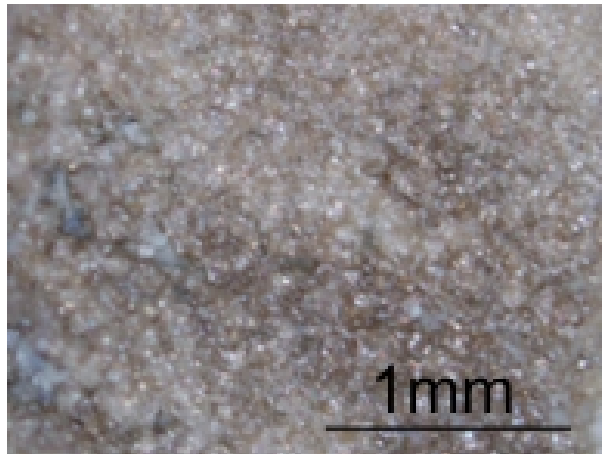


Figure 5.29.: Polycrystalline GaN grown on the  $\text{Al}_2\text{O}_3$  seed

completely block the growth of the GaN layer, enhancing the back reaction. Catalytic effect of Ga manifests itself in the decrease of high kinetic barrier for the reverse reaction (around  $200 \text{ kJ/mole} = 2 \text{ eV/atom}$ ).

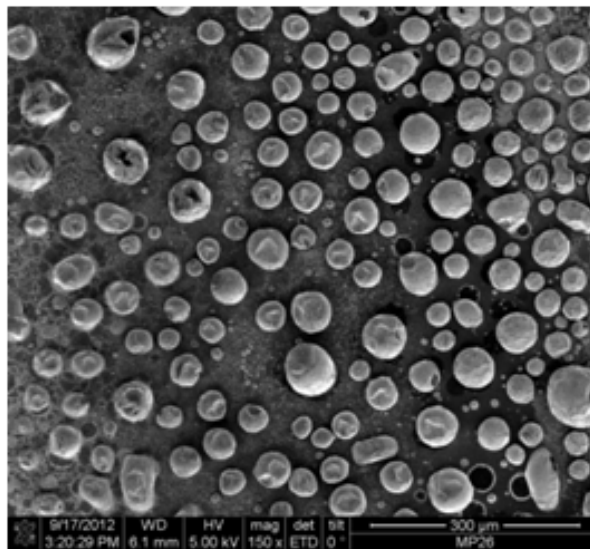


Figure 5.30.: Ga droplets on GaN template on  $\text{Al}_2\text{O}_3$

Fig. 5.30 shows Ga droplets deposited on the GaN template on  $\text{Al}_2\text{O}_3$ . In this experiment the temperature difference between Ga source and seed ( $\Delta T = 400 \text{ }^\circ\text{C}$ ) caused the Ga vapour supersaturation to exceed the upper limit of the growth window (see Fig.

5.31).

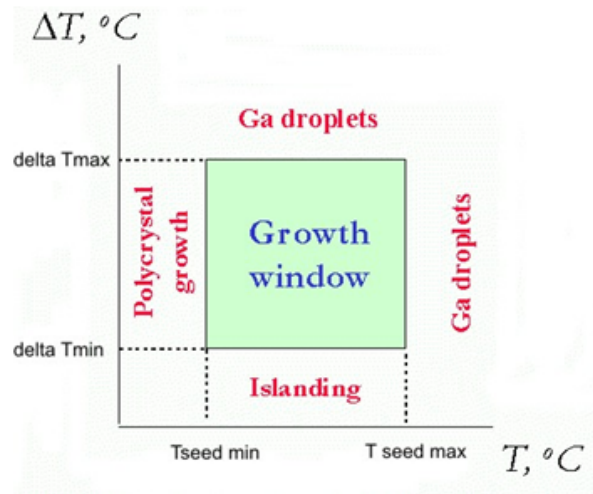


Figure 5.31.: Schematic growth window for sublimation sandwich technique [177]

Appearance of Ga droplets can be also a result of lack of sufficient amount of reactive nitrogen in the growth region or both conditions appear simultaneously. When not enough reactive nitrogen is available, Ga vapour in excess condensates on the colder seed and the seed holder as droplets. Droplet-like formation is due to the large surface tension (around  $709 \text{ mJ/m}^2$ ) [178] and low viscosity of liquid Ga ( $1.369 \text{ mPa s}$ ) [179]. Deficiency of reactive nitrogen, in case of experimental results presented in Fig. 5.30, was caused by unstable plasma operation. Fig. 5.32 presents Ga droplets on the seed-holder after the experiment, in which plasma was not burning steadily and directly beneath the seed. Concurrently, parasitic deposition of amorphous GaN observed in another experiment was caused rather by unstable plasma operation. Since Ga vapour was present in the cavity, the exact plasma position and the temperature distribution in the growth region defined growth location. Deposition of GaN powder was observed either on a part of the seed-holder or on the top cavity flange. Whenever plasma was burning at the edge of seed-holder or between the seed-holder and the top flange, GaN was deposited mainly there (Fig. 5.33). Topic concerning importance of plasma stability was raised and discussed in details in Section 5.2. Discussion on growth experiments is enclosed in Sections 5.5 and 5.6.



Figure 5.32.: Ga droplets on the seed-holder because of plasma instability

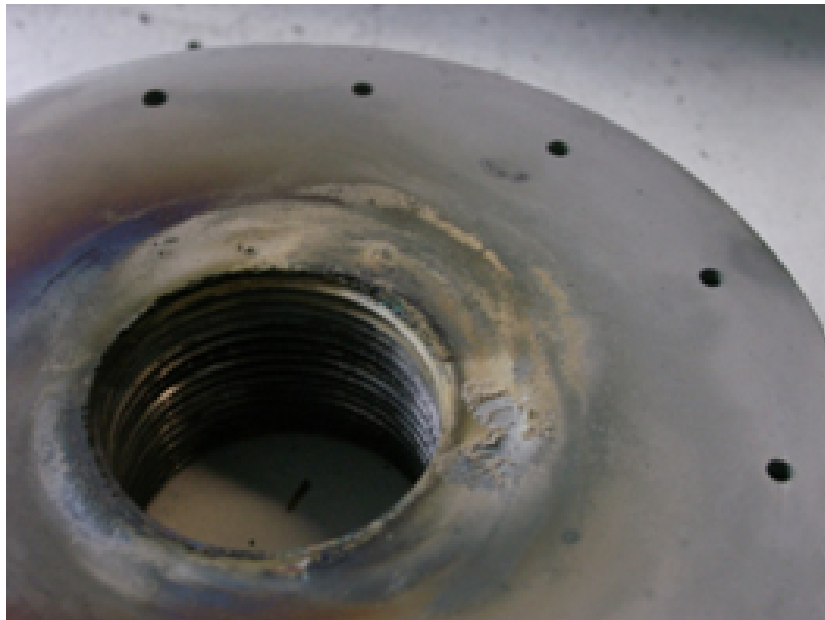


Figure 5.33.: Parasitic deposition of GaN on the top flange

#### 5.4.2. Plasma excitation of Ga vapour

Application of optical emission spectrometer allowed for the in situ measurements of Ga – N<sub>2</sub><sup>\*</sup> system in the vapour phase, in the vicinity of the seed. To the best of author's knowledge, it is the first time when such arrangement was reported in case of moderate pressure (200 - 800 mbar) MW plasma enhanced GaN growth from the vapour.

There have been extensive studies of general properties of MW discharges [98, 180, 181], processes occurring in MW plasmas [182], their operation under atmospheric pressure [183, 184], and comparison with RF plasmas in terms of materials processing [185, 186]. Investigations on OES of electron cyclotron resonance (ECR) and RF remote plasma source itself in MBE reactor and its influence on GaN growth [108, 187] have been carried out as well. So far results of optical emission spectra giving an insight into the growth region during the high pressure MW plasma enhanced GaN synthesis have not been revealed, though.

The in situ analysis of the growth region by means of optical emission spectrometry confirmed presence of Ga vapour under the growth conditions, during the heating and cooling phase. Figures 5.34 and 5.35 present optical emission spectra recorded at RT,  $T_{seed} = 1000$  °C and  $T_{source} = 1200$  °C, respectively. During all the three experimental stages nitrogen plasma was burning in the cavity at a total reactor pressure of 400 mbar. In Fig. 5.34 lines representing excited Ga atoms are not visible, since Ga partial pressure at RT is smaller than  $1.013 \times 10^{-6}$  mbar (Fig. 2.8). Bands of second positive system of  $N_2$  with band heads at 297.7 nm, 316 nm, 337.1 nm, 357.7 nm and bands of CN with band heads at 359 nm, 388.3 nm and 421.6 nm have been observed.

Partial pressure of Ga in relation to temperature was described in details in Subsection 5.4.1. With increasing source temperature, Ga appears in the vapour. The lines at 287.4, 294.4, 403.3 and 417.2 nm, visible in Figure 5.35 can be unambiguously related to Ga [116]. They are sharp and narrow, which is typical for transitions between electronic states in atoms. The strongest Ga lines are 417.205 nm and 403.298 nm with the latter one slightly weaker. The other lines, visible at 294.418 nm, 294.364 nm and 287.42 nm have relatively lower intensity. All the five mentioned lines belong to the group of so called “persistent lines of neutral Gallium (Ga I)”, which are observed over a broad range of experimental conditions. Electron configuration of neutral, gaseous atom of gallium at ground state  $[Ar] 3d^{10} 4s^2 4p^1$  is shown in Fig. 5.36 a) and is denoted as  $4p^2 P_{1/2}$  in Fig. 5.36 b).

When a Ga atom absorbs sufficient energy, an electron can jump to the orbital with

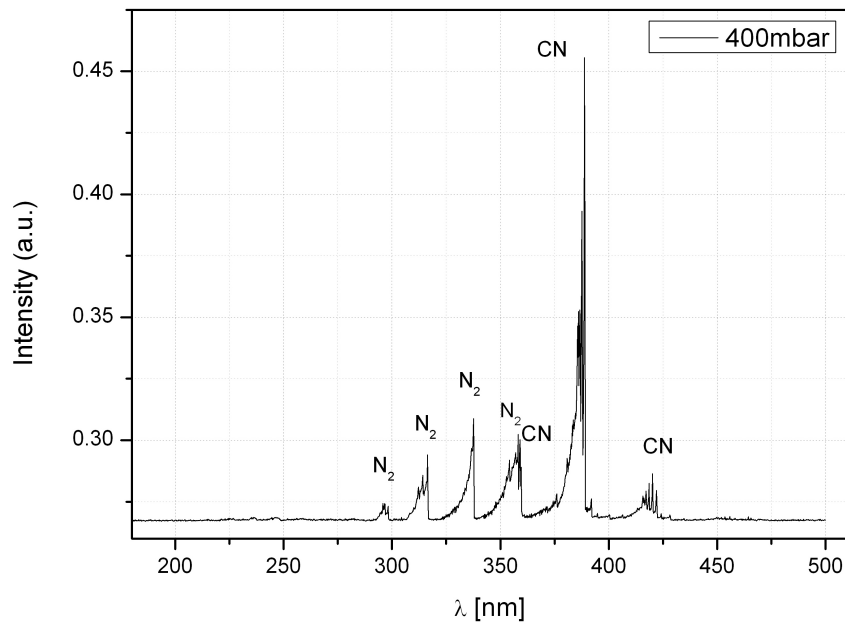


Figure 5.34.: OE spectrum recorded at RT,  $p = 400$  mbar, MW power  $\approx 400$ W, carrier gas flow = 0.1 slm  $N_2$

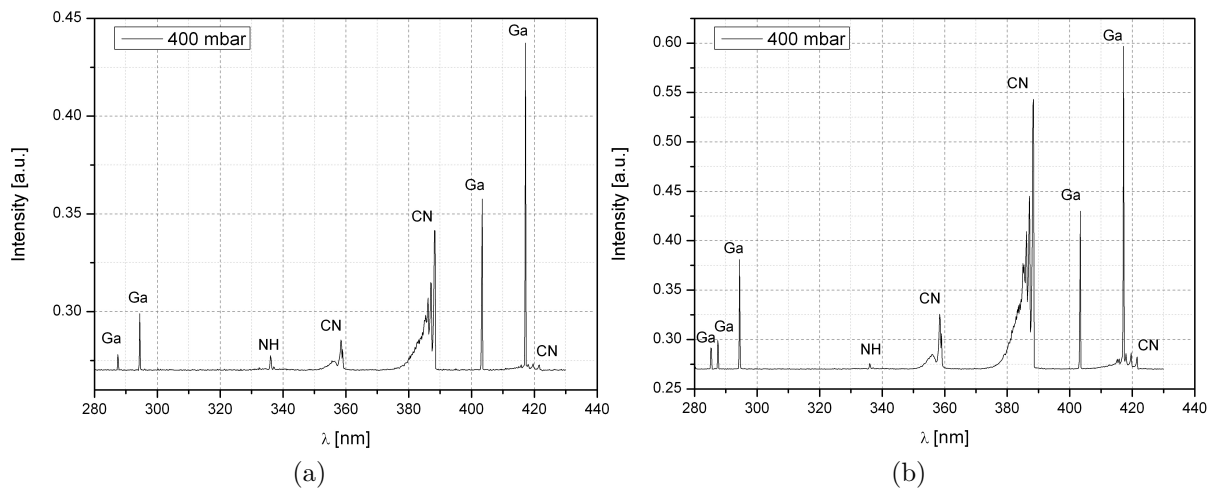


Figure 5.35.: OE spectrum recorded at a)  $T_{source} = 1000$  °C and b)  $T_{source} = 1200$  °C ( $p = 400$  mbar, MW power  $\approx 400$  W, carrier gas flow = 0.1 slm  $N_2$ )

higher energy level. Atom goes then in the excited state, which is unstable and rapidly followed by the recombination and energy emission. For instance, the line at 403.3 nm is the result of radiation when a Ga atom comes back to the ground state from the excited state  $[Ar] 3d^{10} 4s^2 5s$  (denoted as  $5s^2 S_{1/2}$  in Fig. 5.36 b)). The wavelength



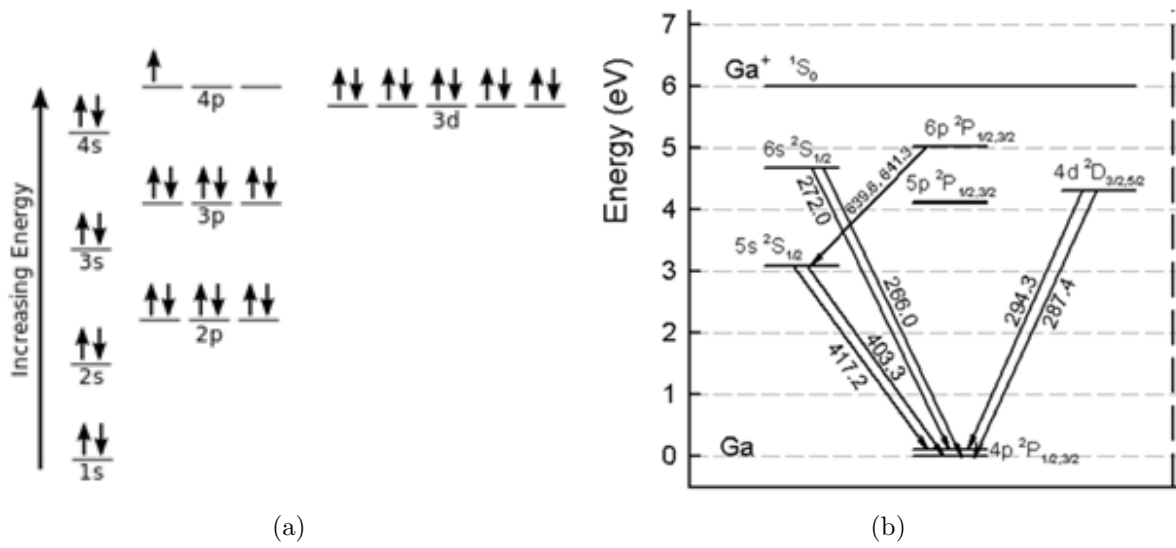


Figure 5.36.: Ga atom: a) electron configuration, b) energy levels

$\lambda' = 403.3$  nm of emission line is related to the difference between energy levels by the Bohr's frequency condition (Eq. 46) [188]

$$\Delta E = E_2 - E_1 = h\nu = hc/\lambda' \quad (46)$$

where:

$E_2$  - energy of the excited state  $5s^2 S_{1/2}$ ,

$E_1$  - energy of the ground state  $4p^2 P_{1/2}$ ,

$\nu$  - frequency of emitted photon,

$\lambda'$  - wavelength of the emission line,

$h$  - Planck constant.

The probability of such a transition is defined by the Einstein coefficient for spontaneous emission  $A_{ki}$  and equals  $0.485 \times 10^8 s^{-1}$ . Data for all the five mentioned persistent lines of neutral Gallium (Ga I) is collected in Table 3. It includes their wavelengths, corresponding transitions between energy levels, transition probabilities and configurations.

where:  $A_{ki}$  - transition probability,  $J$  - total angular momentum quantum number

Table 3.: Persistent lines of Ga [116]

$\lambda$ [Å]	$A_{ki}(10^8 s^{-1})$	Energy levels (cm <sup>-1</sup> )	conf.	Terms	J
2874.235	1.17	0.000	$4s^2 4p$	$^2P^\circ$	1/2
		34781.66	$4s^2 4d$	$^2D$	3/2
2943.636	1.34	826.19	$4s^2 4p$	$^2P^\circ$	3/2
		34787.85	$4s^2 4d$	$^2D$	5/2
2944.173	0.261	826.19	$4s^2 4p$	$^2P^\circ$	3/2
		34781.66	$4s^2 4d$	$^2D$	3/2
4032.984	0.485	0.000	$4s^2 4p$	$^2P^\circ$	1/2
		24788.530	$4s^2 4d$	$^2S$	1/2
4172.042	0.945	826.19	$4s^2 4p$	$^2P^\circ$	3/2
		24788.530	$4s^2 4d$	$^2S$	1/2

Interaction of Ga vapour with MW nitrogen plasma at elevated pressures 200 - 800 mbar does not lead to the extinction of the latter. The results imply rather that Ga vapour and/or droplets do not severely affect the plasma formation, contrary to small water droplets, which can extinct the plasma in RT high pressure microwave sources, like in the case of CYRANNUS sources [189]. However, the influence of Ga on emission processes in plasma has been revealed. The observed phenomena and interplay between Ga and other components of plasma is discussed in the following part of the section.

Apart from sharp Ga lines, broad ‘bands’ of emission frequencies are revealed in the course of measurements (Figures 5.34 and 5.35). The origin of these more complicated molecular spectra was explained in Subsection 3.4.1. Bands of molecular nitrogen, cyano-group and NH group have been observed. The recorded bands of molecular nitrogen (all of them degraded to the shorter wavelength) with band heads at 297.68 nm, 315.93 nm, 337.13 nm, 357.69 nm belong to the second positive nitrogen system (SPS) ( $C^3\Pi_u - B^3\Pi_g$ ). The second positive nitrogen system occurs in most sources, notably through pure nitrogen [190]. Data on the bands in the SPS is collected in Appendix D. In the regions of 358 - 360 nm, 380 - 390 nm and 415 - 420 nm bands constituting the cyano-group (CN) violet system were observed. The functional CN group sticks together by a triple bond [191]. The CN violet system is the result of radiative transitions be-

tween the  $B^2\Sigma^+$  (3.32 eV) and  $X^2\Sigma^+$  (0 eV) electronic states. Numerous theoretical and experimental studies on the spectrum of diatomic CN molecule have been carried out. The CN violet bands have been recorded in most of plasmas (all the types of electrical discharges, laser induced plasmas, etc.), excited in the atmosphere containing both nitrogen and carbon [192, 193]. Comprehensive analysis of the obtained data showed that the vapour system in the growth region is the Ga –  $N_2^*$  - CN one, rather than the pure Ga –  $N_2^*$  only. Mutual interactions between Ga,  $N_2^*$  and CN, and dependencies on the process parameters (T, p, MW power, carrier gas flow) have been observed.

When with increasing source temperature Ga vapour reaches the MW discharge, the intensity of Ga lines (403.3 nm, 417.2 nm) increases and the intensity of  $N_2^*$  and CN lines decreases. Figures 5.37 a) depicts spectra recorded at RT and 5.37 b) at growth conditions (p = 200 mbar, MW power  $\approx$  600 W,  $N_2$  carrier gas flow 0.1 slm).

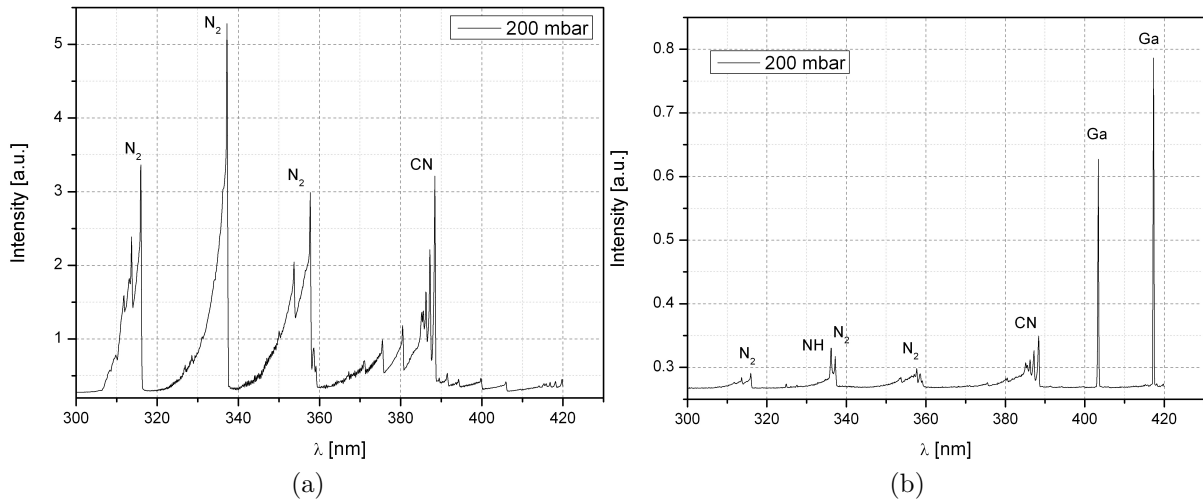


Figure 5.37.: OE spectrum recorded at a) RT, b)  $T_{source} = 1200$  °C,  $T_{seed} = 1000$  °C

At RT recorded relative intensity of the band heads of excited molecular nitrogen equalled 3.36 (316 nm), 5.28 (337.2 nm), 2.99 (357.7 nm) and CN band head 3.21 (388.4 nm), whereas at  $T_{seed} = 1000$  °C intensity dropped significantly to the following levels: 0.30 (316 nm), 0.36 (337.2 nm), 0.31 (357.7 nm) and for CN 0.42 (388.4 nm). Concurrently strong Ga lines at 403.3 nm and 417.2 nm were unquestionably detected at the growth temperature of  $T_{seed} = 1000$  °C. As soon as Ga appears in the growth

region, intensity of nitrogen lines decreases. The most probable explanation is related to the fact that energy levels of excited states of Ga atoms are located below the energy levels of excited states of nitrogen (Fig. 5.36). Excitation threshold of the 403.3 nm and 417.2 nm Ga lines equals 3.07 eV [194]. Excitation thresholds of the nitrogen bands are significantly higher. The  $A^3\Sigma_u^+$  state of excited nitrogen molecule has energy of 6.17 eV. The zero vibrational level of triplet state molecule  $B^3\Pi_g$  (emitting 1st positive system of the molecular nitrogen) lies 7.35 eV above the ground state nitrogen molecule, whereas the zero vibrational level of  $C^3\Pi_u$  state molecule (emitting 2nd positive system, in the range of 300 – 360 nm) equals 11.03 eV [111]. Dissociation energy of  $N_2$  is also considerably high, with the value of around 9.8 eV [195] that is even higher than Ga ionization energy of 5.99 eV [116]. When it comes to the CN band at 388.3 nm, its excitation energy of 3.19 eV [196] is only slightly higher than 3.07 eV, yet much lower than Ga energy level for emission at 287.4 nm and 294.3 nm (4.31 eV). Under the assumption that discharge is carbonaceous, the CN violet band at 388.3 nm accompanies the persistent lines of Ga at 287.4 nm and 294.3 nm.

Experiments in the carbon free setup have been conducted to study Ga -  $N_2^*$  interactions in plasma. The most important parameters were typically set to the following values:  $T_{source} = 1200$  °C,  $T_{seed} = 900$  °C,  $p = 200$  mbar,  $N_2$  carrier gas flow 0.1 slm.  $T_{max}$  for operation of our isolation material (Altraform KVS 184/400) in vacuum is 1800 °C. Owing to the high porosity of the Altraform felt, the reactor's atmosphere was contaminated with oxygen during the experiment. Growth experiments in the Ga -  $N_2^*$  - O system resulted in the deposition of amorphous gallium oxide rather than GaN on the seed. It is known that synthesis of oxides is more favourable than nitrides, since bonding in the  $O_2$  molecule is much weaker (498.3 kJ/mol) than in the  $N_2$  molecule (945.3 kJ/mol). Spectra recorded during the growth in the atmosphere containing oxygen, revealed Ga lines (287.4 nm, 294.3 nm, 403.3 nm and 417.2 nm) and NH band, with a band head at 336 nm.

The Altraform felt was replaced with a new graphite felt, covered by a dense pyrolytic carbon layer, and being the only component of the setup that contains carbon. This

version of the growth system is denoted as the growth setup with greatly reduced carbon content (see description in Subsection 5.1.1), used for studies of Ga - N<sub>2</sub><sup>\*</sup> interactions, without the carbon influence. Figure 5.38 presents the results of the experiment under the following conditions:  $p = 200$  mbar, MW power  $\approx 350$  W, N<sub>2</sub> carrier gas flow was turned off to prevent unintentional transport of graphite particles from the bottom of the reactor, which had been used for the experiments in the graphite environment before.

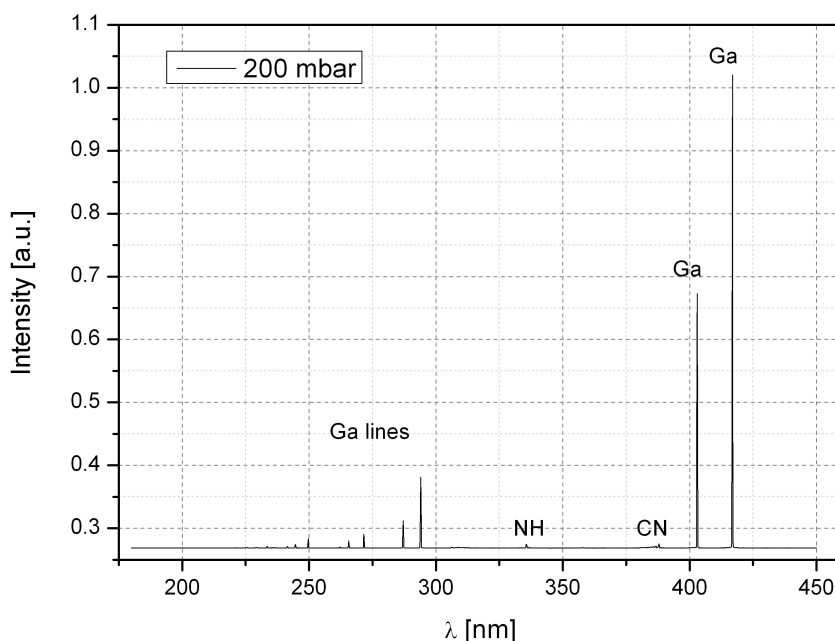
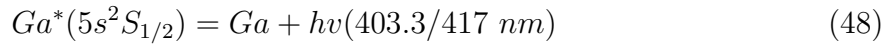


Figure 5.38.: OE spectrum recorded at  $T_{source} = 1100$  °C,  $T_{flange} = 700$  °C (temp. of the flange covering the resonance cavity from the top)

Spectra recorded at growth temperature do not contain any visible bands of molecular nitrogen, being dominated by Ga lines. There are two strong lines at 403.3 nm and 417.2 nm, as well as the whole series of lines lying below 300 nm, with higher excitation energies (given in brackets), however still below the excitation energy level of the SPS of nitrogen (10.9 eV). These are lines at 294.4 nm and 287.4 nm (4.31 eV), 271.9 nm and 265.9 nm (4.66 eV), 250 nm and 245 nm (5.06 eV), 241.8 nm and 237.1 nm (5.23 eV) and 233.8 nm (5.4 eV). Bands of NH (336 nm) and CN (388.3 nm) can be resolved as well, yet their intensity is far lower than of Ga lines. The obtained results are consistent with the observations reported by Corr et al. [187], who studied the remote plasma chemical

vapour deposition of GaN. Optical emission spectrum of pure nitrogen plasma near the substrate did not contain any bands of molecular nitrogen, neither of the SPS or the FPS. The intensive lines of Ga at 403.3 nm and 417 nm were present, though. Corr et al. [187] suggested that the excitation of Ga atoms is caused by their collisions with excited nitrogen from the long-lived  $N^*(^2P)$  metastables



Finally, the following mechanisms of interaction of Ga vapour with nitrogen plasma, are proposed. Most of the MW energy is consumed by Ga atoms, while their transitions from the ground state to the low-lying excited states. This phenomenon is in accordance with the observations made during the interaction of Ga vapour with hydrogen plasma [197]. Due to inelastic collisions of electrons with Ga, fast electrons quickly lose their energy. Thus, the number of fast electrons, which could excite nitrogen, decreases significantly. The immediate result is that lower intensity of  $N^*(^2P)$  emission could be detected (Fig. 5.37) or lines representing emission from  $N^*(^2P)$  states are not detectable at all (Fig. 5.38). Furthermore, Ga atoms are excited in the collisions with the excited nitrogen species, as described by Corr et al. [187]. Their subsequent transition to the ground state results in the strong emission in VIS/UV region of spectra.

## 5.5. Deposition experiments as optimisation tool

The following section is intended to present results of deposition experiments, which were utilised as input for optimization of the growth setup. Obstacles for the growth control have been identified and minimized by the implementation of improvements in the system. Importance of the choice of appropriate materials for the setup is stressed, as their resistance to the reactor's atmosphere is crucial for the reproducible crystal

growth. Influence of high temperature MW plasma on setup components is shown. There is a number of parameters to handle with during the deposition/growth experiments, including pressure in the reactor  $p$ , temperature of the Ga source  $T_{source}$ , temperature of seed  $T_{seed}$ , growth time  $t_{growth}$  and MW power. Full set of chosen parameters' values is provided for each deposition experiment, described in this section.

The first series of deposition experiments was conducted in a preliminary version of the growth setup. Due to the lack of an optical access to the top of the seed, pyrometer was not useful in terms of measurements of the seed temperature. Therefore, temperature of the top flange was measured instead, using a type K thermocouple (measurements range up to 1350 °C). It was assumed that the temperature of the seed can be approximated by the temperature of the flange. Due to the indirect measurements of the seed temperature, seeds resistant to higher temperature than GaN templates were favoured. Either double side polished (DSP) sapphire, thermally stable up to 1600 °C [198], AlN (700 nm thick) templates on sapphire, or Al<sub>0.28</sub>Ga<sub>0.72</sub>N (20 nm thick, 28 %) on GaN (2 µm thick) on sapphire were utilised. Decomposition of AlN in vacuum without the presence of active nitrogen starts at 1400 °C [199], implying that AlN templates are stable under our growth conditions. In few later experiments GaN (2 µm thick) templates on sapphire were utilised.

Seeds were cut out of 2 in substrates, using a diamond blade. Typical dimensions of prepared samples were around 10 x 5 mm. DSP sapphire wafers were delivered by PB-Technik AG (Switzerland) (c- orientation, thickness 400+/-25 µm, epi ready polished), whereas AlN templates on sapphire came from FBH Berlin. After cutting, sapphire seed was cleaned in acetone and isopropanol solvents for 10 min each, and subsequently rinsed in de-ionized water and dried in nitrogen flow. AlN seed was also degreased by acetone and iso-propanol, and rinsed in de-ionized water. Afterwards the seed was additionally etched in H<sub>2</sub>SO<sub>4</sub> : H<sub>2</sub>O<sub>2</sub> : H<sub>2</sub>O (3 : 1 : 1) solution, rinsed in de-ionized water, and finally dried in nitrogen flow prior to the experiment. Accurate control of the seed temperature is decisive for GaN growth from the vapour. The deposition experiments with the indirect control of the seed temperature were only partially successful. Nevertheless, in one of the

## 5. Experimental - MW plasma enhanced growth

---

first experiments GaN crystallites of  $\mu\text{m}$  size were locally grown on  $\text{Al}_2\text{O}_3$  (Fig. 5.39), showing feasibility of this method for growth of GaN. Parameters of the experiment (see MP2 in Table 7 in Appendix C) leading to the first growth of GaN material, using microwave plasma enhanced setup at relatively high pressure (200 - 800 mbar), were the following:  $p = 200$  mbar,  $T_{\text{source}} = 1450$  °C,  $T_{\text{flange}} = 1100$  °C,  $\text{N}_2$  carrier gas flow = 0.2 slm, MW power  $\approx 300$  W. Ga weight loss was equal to 3.51 g, while the seed gained 0.02 g.

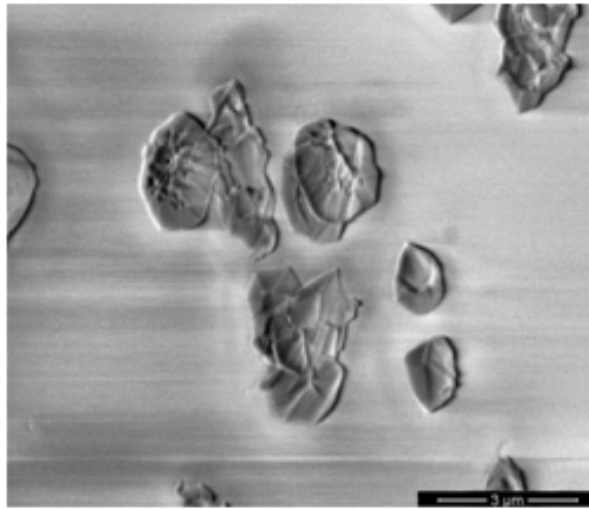


Figure 5.39.: GaN crystallites

Optical path for pyrometer was established by changing the mounting of the inner coaxial tube and the ceramic tube. The new supporting system, composed of two ceramic (Alsint 99.7) pins, was introduced to carry the total weight of the ceramic tube, inner coaxial tube and the seed-holder. Round graphite tablet, diameter of 8 mm, was placed on the seed's backside for temperature measurements by pyrometer. Another drawback of the preliminary version of the setup was the seed-holder itself. Its cross-section and bottom view are depicted in Fig. 5.40.

The first version of seed-holder revealed its disadvantages, while operation in the vicinity of burning plasma. Sharp edges of tantalum clamps and of the seed-holder itself led to the formation of electric arcs in plasma (see Fig. 5.41).

Arc discharges between metal parts of the seed-holder and in a burning plasma, en-



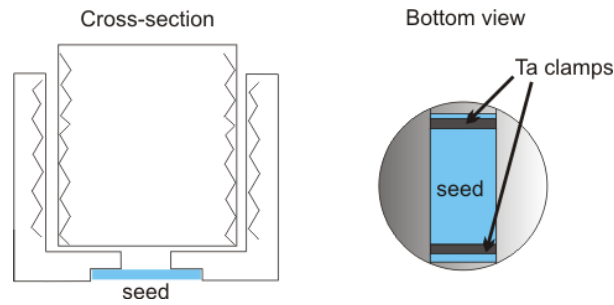


Figure 5.40.: The first version of seed-holder

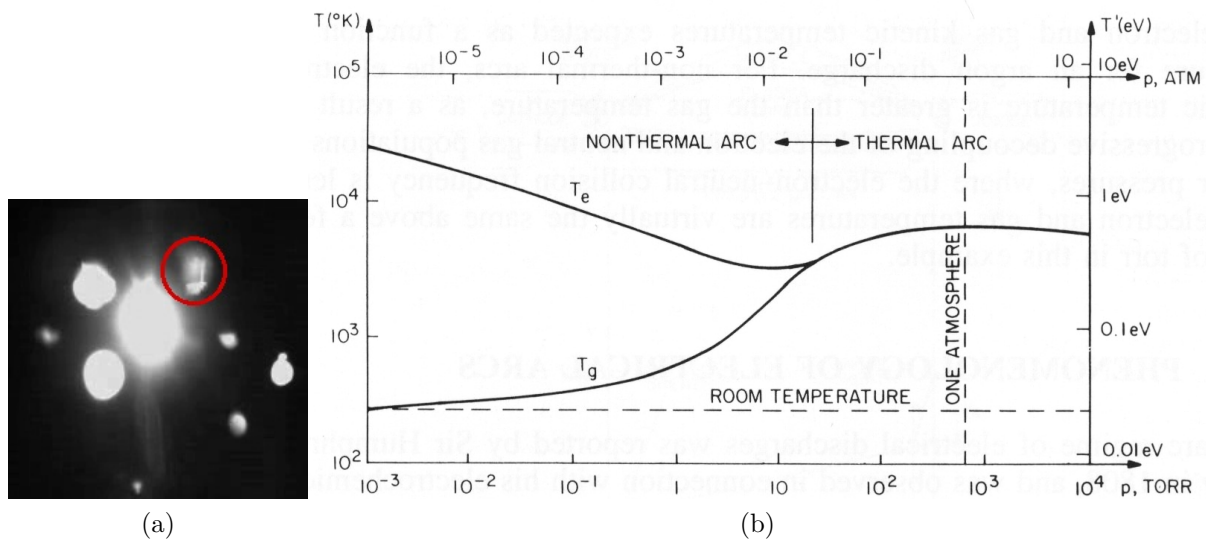


Figure 5.41.: a) arc discharge, b) the operation of arcs as a function of pressure [98]

hanced decomposition of the AlN template. Arcs are characterised by high currents and high currents density. Within the range of pressures (200 – 800 mbar) used in the described experiments, one speaks about thermal arcs (Fig. 5.41 b)). Their high currents, from 50 to  $10^4$  A [98] could easily cause local evaporation/decomposition of AlN, as the value of current arc multiplied by electric field intensity in thermal arcs exceeds 1 kW [98].

In Fig. 5.42 a) SEM picture of cutaway of surface of AlN template after 6 h long experiment is presented. The experiment's conditions were:  $p = 600$  mbar,  $T_{source} = 1345$  °C,  $T_{flange} = 905$  °C,  $N_2$  carrier gas = 0.2 slm,  $N_2$  background gas 0.1 slm, MW power  $\approx 520$  W (see also MP4 in Table 7 in Appendix C). Ga weight loss was equal to 0.53 g,

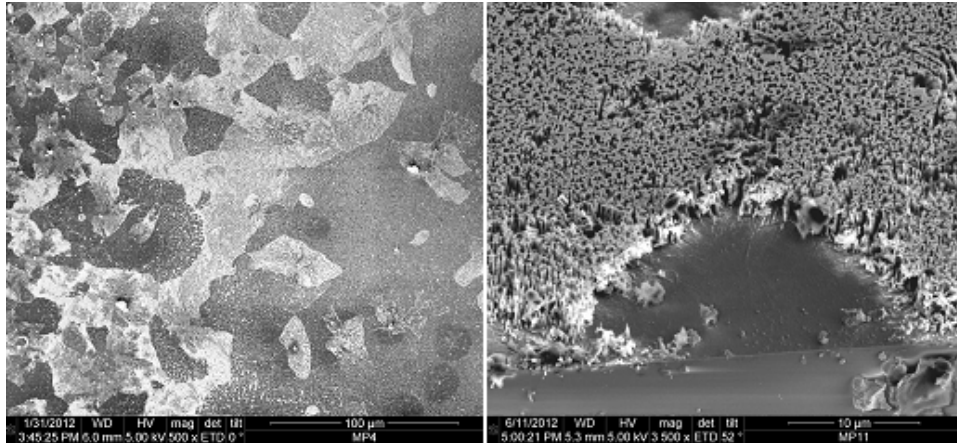


Figure 5.42.: a) locally etched AlN template, b) decomposed GaN template

while seed lost 0.03 g of its weight. Growth was not observed. The AlN template was locally decomposed due to the high temperature action of high-thermal arcs. Negative impact of arcs on the GaN template is shown in Fig. 5.42 b), as vertical tunnels have been etched in the GaN layer. Some areas of the GaN layer have been even completely removed, revealing the underlying sapphire substrate.

Results of another experiment from the first series of deposition tests suggest undesired interaction of Ta clamps and the seed. An island containing solidified tantalum was found on the seed surface. Picture taken with SEM is presented in Fig. 5.43 a), whereas island elemental composition is depicted in Fig. 5.43 b) (EDX scan).

Since melting temperature of tantalum equals 2996 °C [200], it indicates that during the 4 h growth phase, temperature of tantalum stripe exceeded its melting temperature. Such high temperature, appearing (even only locally) on the seed, makes growth of GaN impossible. Local increase of the temperature above 3000 °C can result from thermal arcs or heating by thermal plasma burning at the seed. Darker oval regions visible in Fig. 5.43 next to the Ta island are Ga droplets, transported from the Ga source and deposited on the seed. Parameters of the experiment described above were as follows:  $p = 200$  mbar,  $T_{source} = 1430$  °C,  $T_{flange} = 990$  °C,  $N_2$  carrier gas  $\approx 0.2$  slm, MW power  $\approx 550$  W (see also MP5 in Table 7 in Appendix C). Ga source weight loss was equal to 4.33 g, while the seed gained 0.01 g. In order to overcome problems with arc

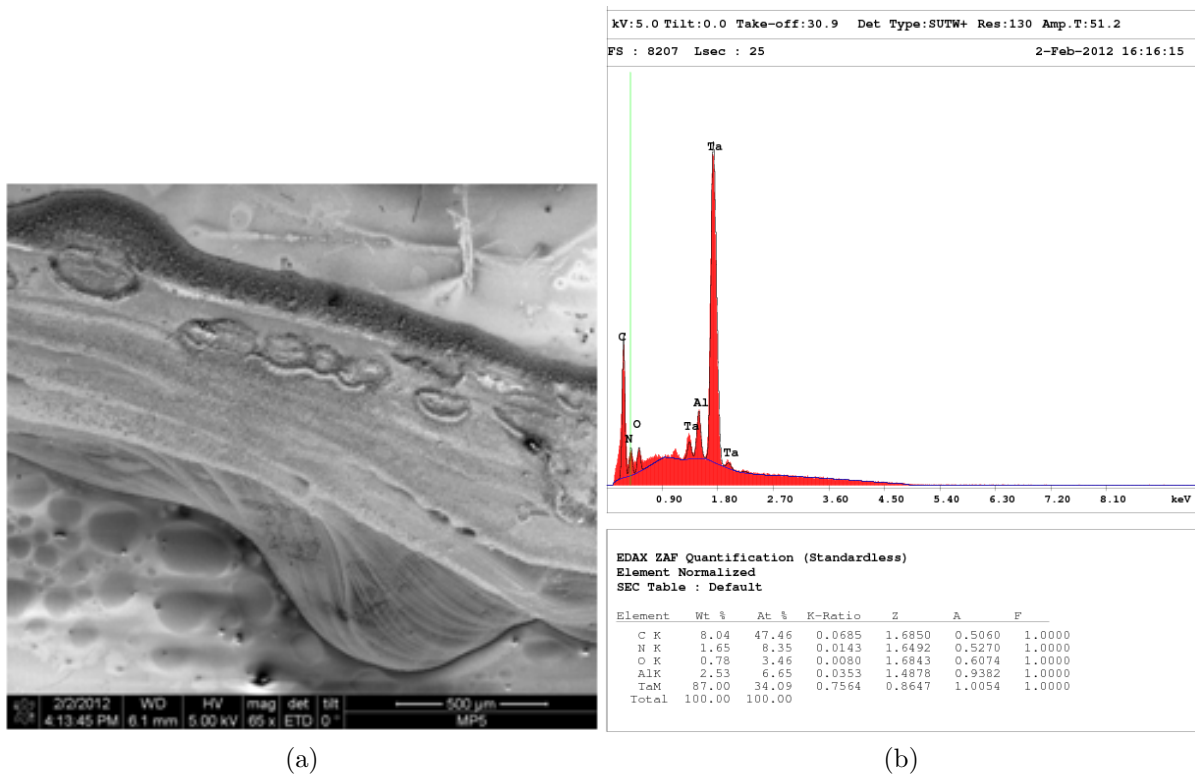


Figure 5.43.: Ta melted during the experiment: a) SEM picture, b) EDX scan

formation in the vicinity of the seed and to improve seed's mounting system, the new seed-holder was designed and manufactured.

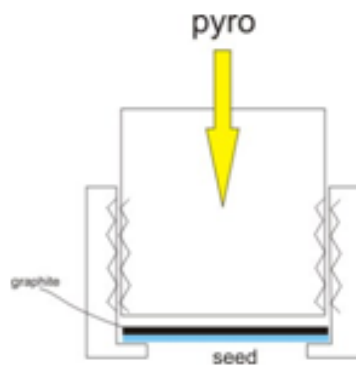


Figure 5.44.: Seed-holder

Rounded edges should prevent formation of excessive electric field strength and reduce the probability of arc discharge. Seed was shifted 1 mm into the seed-holder, so to

prevent its direct contact with hot plasma and reduce decomposition rate of the growing GaN layer. Owing to nitridation of the titanium cavity, its mechanical strength severely decreased, especially on welds. During removal of the cavity from the system, it was unintentionally tapped. Thereby, the lid was separated from the cavity walls (Fig. 5.45). Hence, a cavity made of molybdenum was used in the further experiments. Since molybdenum is much more resistant to nitridation than titanium, emergence of yellowish/brownish nitride layer on its surface was not visible, even after several experiments.

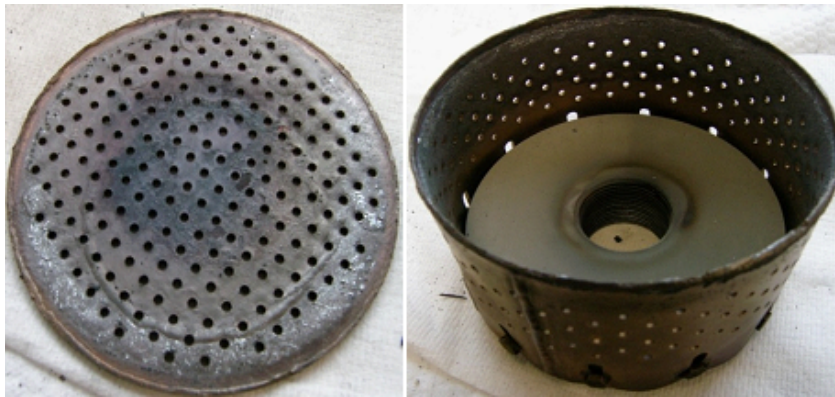


Figure 5.45.: Titanium cavity after few experiments

Outcome of the continuous efforts to optimize growth parameters and growth procedure are discussed below. Formation of needle-like GaN structures (Fig. 5.46) was associated to extremely high supersaturation of Ga vapour ( $\Delta T \approx 400 K$ ), (see MP22 in Table 7 in Appendix C). Needles were grown horizontally, following a certain pattern on the seed surface. Most of angles between the needles equal  $120^\circ$ , giving an impression of hexagonal structures built by the needles. In the subsequent experiments level of supersaturation was decreased. The case, in which growth conditions were not homogeneous over the whole seed surface, is presented in Fig. 5.46 b) (for growth parameters see MP26 in Table 7 in Appendix C). Well oriented GaN crystal islands along with the GaN needles, similar to those visible in Fig. 5.46 a), have been formed.

Further reduction of Ga supersaturation promoted growth of GaN islands only. They are composed of 5 – 10  $\mu\text{m}$  size GaN crystallites of hexagonal shape, growing in the c

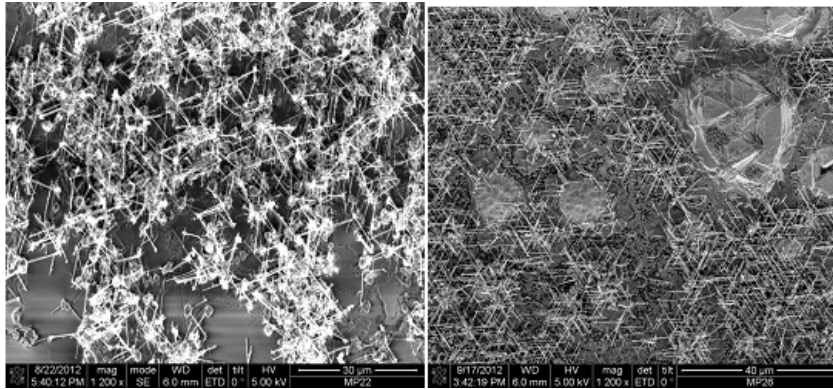


Figure 5.46.: GaN needles grown on a)  $\text{Al}_2\text{O}_3$  and b) GaN template on  $\text{Al}_2\text{O}_3$

direction on the AlGaN/GaN template on sapphire c plane seed (Fig. 5.47). Formation of c-facets is a result of lower growth rate in c-direction than in a- or m-direction. GaN crystallite grown on the top of c-facet may be a result of supercritical supersaturation. Parameters of this deposition experiment were as follows:  $p = 400$  mbar,  $T_{\text{source}} = 1300$  °C,  $T_{\text{seed}} = 865$  °C (reduced temperature due to problems with plasma stability at temperatures higher than 900 °C), MW power  $\approx 400$  W,  $\text{N}_2$  carrier gas flow = 0.1 slm (see also MP30 in Table 7 in Appendix C).

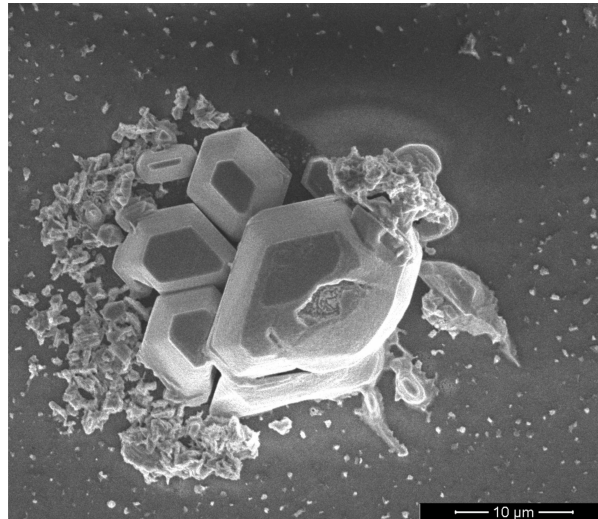


Figure 5.47.: GaN crystallites grown on AlGaN template

Subsequent optimization of the process and improved plasma stability resulted in the

growth of single crystalline GaN layers, which are studied in the next Section 5.6.

## 5.6. Growth of GaN single crystalline layers

This section is intended to present the results of MW plasma enhanced growth of GaN single crystalline layers at sub-atmospheric pressures within the 200 - 800 mbar range. In Subsection 5.6.1 the most important steps of the experimental procedure are described, whereas Subsection 5.6.2 is devoted to the characterisation of the grown GaN layers. Based on the conclusions from previous sections and on the analysis of characterisation, possible growth scenarios are discussed.

### 5.6.1. Experimental procedure

For simplicity the experimental procedure was divided into eight stages. Starting from the cleaning of the seed, through the installation of the growth setup and adjustment of the cavity, up to the actual growth procedure.

1. Cleaning of the seed.

Before placing in the seed-holder, each seed was cleaned, following the recipe described in Section 5.5.

2. Adjustment of the cavity.

Adjustment of the vertical position of the cavity is conducted in the system configuration nr 1 (see Subsection 5.1.1). To compensate shift of the resonance frequency because of the thermal expansion of the growth setup elements (cavity, inner coax tube and seed-holder), the resonance frequency is set initially to higher values. Usually it is 2.49 GHz instead of 2.45 GHz.

3. Growth setup installation.

This step comprises placing the Ga source in the crucible, removal of gallium oxide layer from the top of liquid Ga, and installation of the cavity inside the reactor.

Each time it was assured that thermocouple is in contact with the Ga crucible and pyrometer has an optical access to the graphite platelet in the seed-holder.

4. Pumping and purging the reactor with nitrogen.

Pumping down to around  $2 \times 10^{-5}$  mbar and purging with N<sub>2</sub> up to 800 mbar. This procedure is repeated twice.

5. Heating up the system.

The growth setup kept at approx. 60 mbar is gradually heated by the induction coil, until  $T_{seed}$  reaches the desired value, max. 850 °C (in case of GaN template) or around 1000 °C (in case of Al<sub>2</sub>O<sub>3</sub>, AlN template).

6. Plasma ignition

When, due to external heating, the resonant freq. has been shifted to approx. 2.45 GHz, the network analyzer is detached and the magnetron is attached to the reactor (see configuration nr 2 in Subsection 5.1.1). Plasma is ignited with the lowest possible value of MW power in the CW operation mode of the magnetron, i.e. 300 W.

7. Growth experiment

Further heating of the setup and increase of the total pressure in the reactor, followed by the turning on the flow (typically 0.1 slm) of the N<sub>2</sub> carrier gas that defines the beginning of the growth. OES of MW plasma are recorded during experiment.

8. Post-growth procedure.

It comprises turning off the carrier gas and the inductive heating, cooling down the setup by convection and turning off plasma, when Ga no longer evaporates and  $T_{seed}$  comes below the critical decomposition T (800 °C). Subsequently the reactor is pumped down and purged with nitrogen.

### 5.6.2. Characterisation of GaN layers

Single crystalline GaN layers were grown both on Al<sub>2</sub>O<sub>3</sub> and GaN templates. Morphology of their surfaces was studied by scanning electron microscopy (SEM), whereas the elemental analysis of the samples was done by energy-dispersive X-ray spectroscopy (EDX). With the use of secondary ion mass spectrometry (SIMS), trace analysis of C impurities was conducted. High resolution X-ray diffraction (HRXRD) provided data on the crystallographic structure of the grown films. The results of the characterisation, together with the optical emission spectra of the growth region are used as a starting point for the discussion of plausible paths of the GaN synthesis.

Figures 5.48 a) and b) show typical GaN layers after 4 h growth on sapphire a)  $T_{source} = 1400$  °C,  $T_{seed} = 990$  °C, carrier N<sub>2</sub> flow = 0.1 slm, p = 400 mbar, MW power  $\approx 400$  W (see MP21 in Table 7 in Appendix C), b)  $T_{source} = 1240$  °C,  $T_{seed} = 940$  °C, carrier N<sub>2</sub> flow = 0.1 slm, p = 400 mbar, MW power  $\approx 380$  W (see MP32 in Table 7 in Appendix C), and etching of Ga excess in HCl:H<sub>2</sub>O (1:2). In case of sample a), plasma was not burning steadily during the whole growth time, and a large amount of Ga excess was found on the grown interface after the process. Ga is known to catalyse GaN decomposition in vacuum and a similar behaviour is expected at moderate pressure [45]. The etching action of excess Ga hinders the coalescence of crystallites, and leads to the formation of small pits on their top surface. It is known that small amount hydrogen, which was not present in the reactor, improves the morphology of GaN layers [201]. The crystallites shown in Figure 5.48 b) are smaller, without top surface pits and have been grown without visible excess of Ga.  $T_{seed}$  was 50 °C lower than in case of sample a), which resulted in faster nucleation (smaller critical radius  $r^*$ ).

In Fig. 5.49 a tilted view of the GaN grown on sapphire is presented. Layer is composed of pyramidal structures, which are typical for growth of GaN on sapphire [202]. The 3D growth mode is preferred, resulting in several islands, rather than a flat, coalesced surface. Predominantly rounded facets suggest growth under high supersaturation of Ga.

EDS maps (Fig. 5.50) confirmed that the obtained crystallites consist of GaN. Alu-



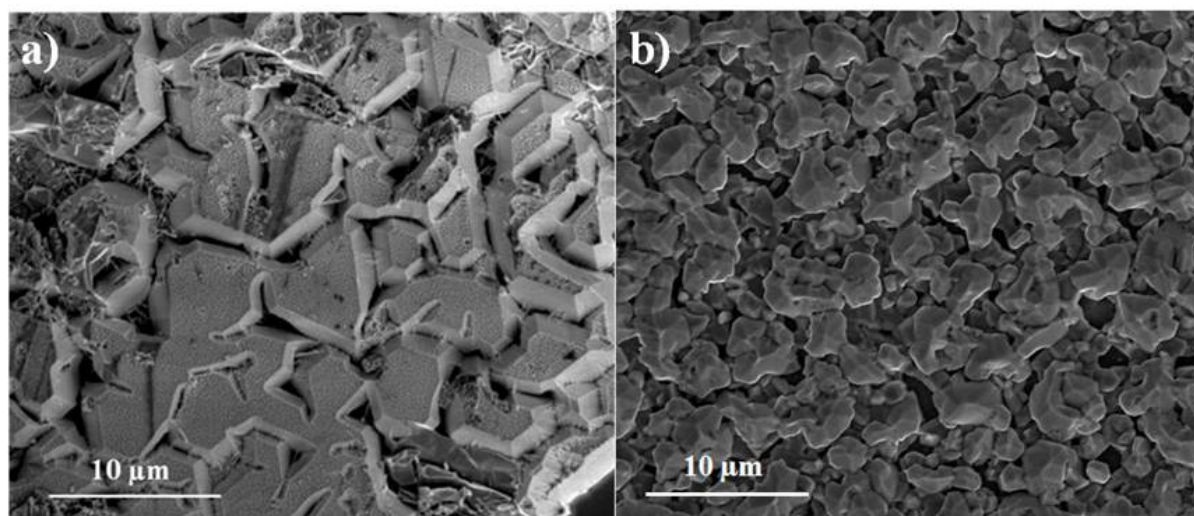


Figure 5.48.: Sample surfaces of GaN crystallites on sapphire grown with a) Ga excess b) and without visible Ga excess (SEM image). Both images were taken after etching the sample in HCl:H<sub>2</sub>O (1:2)

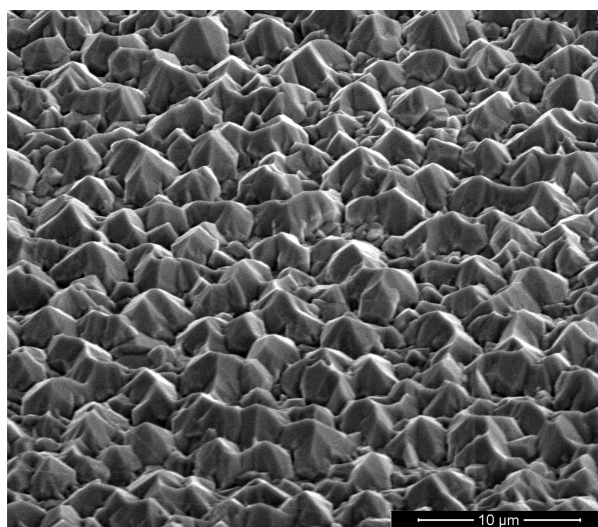


Figure 5.49.: Single crystalline GaN grown on sapphire

minium and oxygen, most probably coming from the sapphire substrate, were found at a lower concentration than Ga and N. Plasma was surrounded by the Mo cavity, and did not come in direct contact with graphite parts. Yet image C of Figure 5.50 shows three 'particles' (see the three spots on the right hand side of the carbon map), which might be tiny dust from the surrounding graphite susceptor and isolation felt.

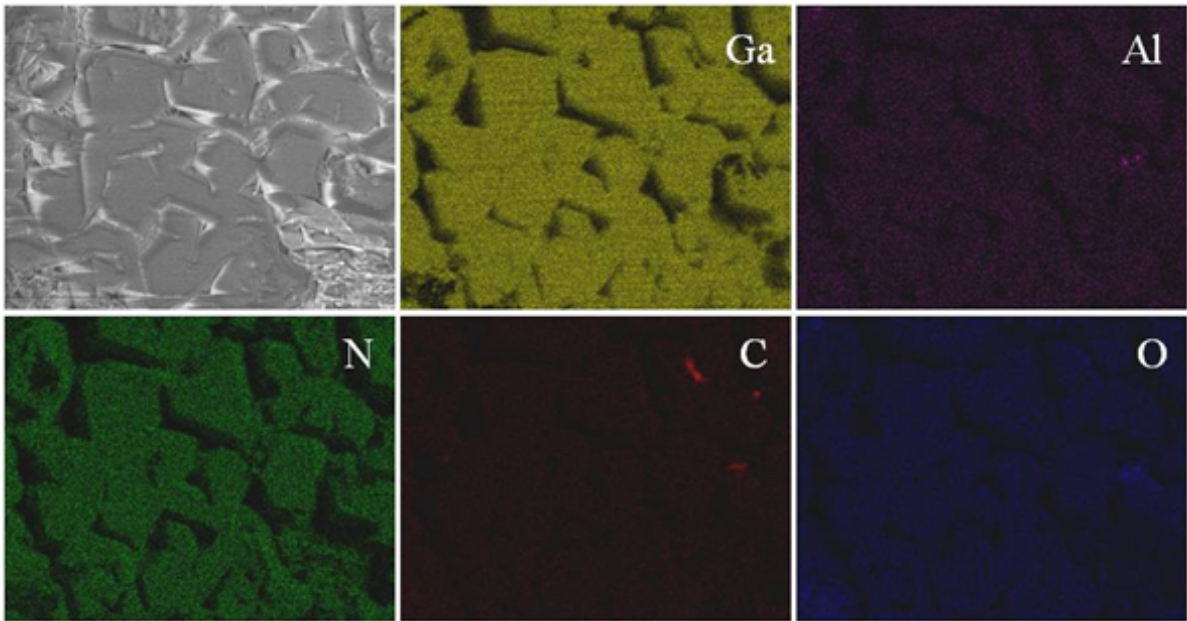


Figure 5.50.: SE image and EDS maps for gallium, nitrogen, aluminium, oxygen and carbon (incident electron energy of 5 keV)

The composition of the deposit was independently confirmed by HRXRD measurements (Fig. 5.51). These detected mainly GaN, however sapphire ( $\text{Al}_2\text{O}_3$ ) substrate (peak not shown) was also found, as the GaN layer was not completely closed. The full width at half maximum (FWHM) was 0.60 deg (2160 arcsec). This is much more than the (0002) FWHM range of 80 to 230 arcsec published for 300  $\mu\text{m}$  thick freestanding HVPE layers [203].

GaN crystallites grown within 4 h on the GaN/sapphire template are depicted in Fig. 5.52. Due to the difficulties with stable plasma operation,  $T_{seed}$  was limited to 900  $^\circ\text{C}$  only (see MP46 in Table 7 in Appendix C). This much too low temperature obstructed the formation of fully consolidated layer. Typical diameter of GaN islands is around 20  $\mu\text{m}$  and the distance between the neighbour islands does not exceed 10  $\mu\text{m}$ . EDX measurements revealed Ga and N in the crystals composition, as well as C, like in the case of GaN grown on sapphire.

In-situ observation of the growth region by the OES supported studies on the growth model for GaN in this MW plasma enhanced growth method. Two routes of GaN synthe-

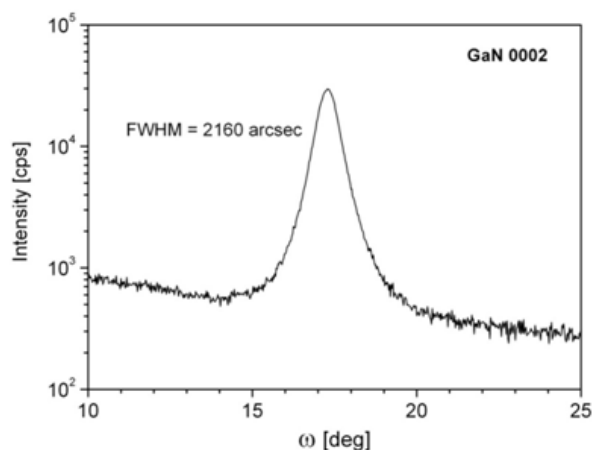


Figure 5.51.: HRXRD rocking curve of GaN (0002), sample on sapphire

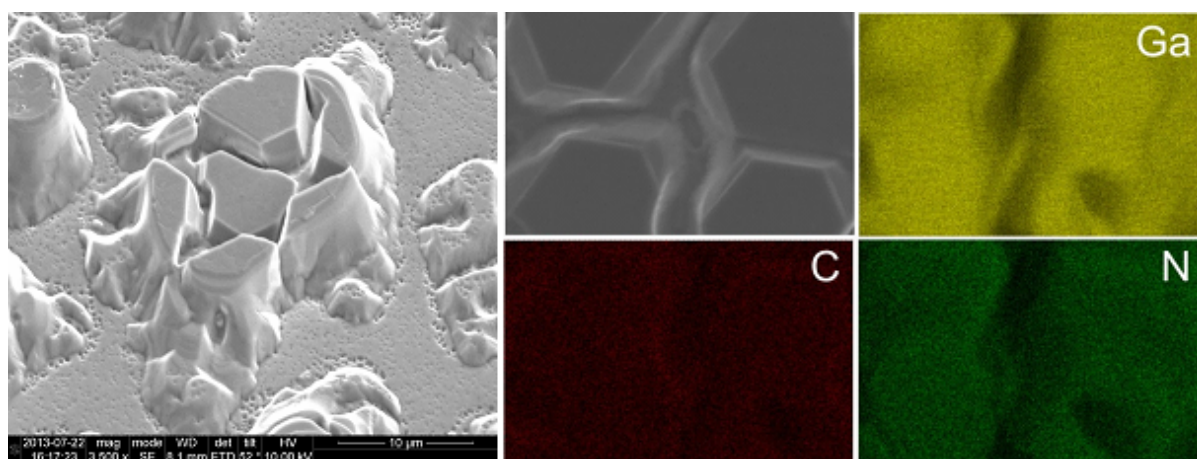


Figure 5.52.: GaN on GaN. GaN crystallites grown on GaN template: a) SEM picture, b) EDS maps. Incident electron energy of 5 keV

sis have been taken under consideration. The first one assumes reaction between excited Ga and  $N_2$  in the vapour phase, while the second one predicts formation of GaN only on the seed surface and comprises two possible paths (see Fig. 5.53).

Reaction between excited Ga and  $N_2$  in the vapour would mean that its product, GaN molecule, exists in the vapour as well and it is then successfully transported to the growing interface. To the author's best knowledge, there are no spectroscopic data for GaN molecules available and no one has reported on identification of GaN molecule in the vapour so far. Existing literature is confined to theoretical studies of the spectroscopic

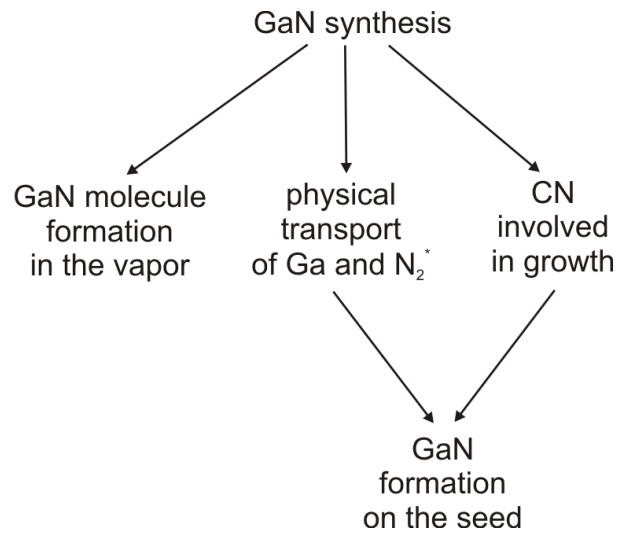


Figure 5.53.: Routes of GaN synthesis

constants [204] and electronic states of the GaN molecule. Calculations performed by various research groups [204, 121, 205] are convergent and indicate that the ground state is  $3\Sigma^-$  and the first excited state is the low lying  $3\Pi$ , hence the energy separation of these two states ranges from 0.5 eV [204] to 0.08 eV [121]. Hirako et al. [206] proposed the main reaction pathway of GaN growth in MOVPE by employing computational fluid dynamics simulation study. Their model includes formation of GaN molecules in vapour, close to the substrate. In case of our MW plasma enhanced growth of GaN, GaN species were not identified in the plasma. Spectra recorded in the range from 200 nm to 1100 nm, at RT and under growth conditions, did not reveal any bands that could be possibly assign to GaN molecule. Even if GaN molecules were formed in the vapour, it is highly possible that high temperature of plasma would immediately cause its decomposition.

In Fig. 5.54 comparison of the measured spectra of  $N_2$  with its simulation in Specair [207] is presented. There is a good agreement between measured spectra of  $N_2$  and its simulation, when both  $T_{rot}$  and vibrational temperature ( $T_{vib}$ ) were set to 3500 K. Under the assumption described in Section 3.4, one can thus estimate gas temperature of plasma at 3500 K. It is well above the threshold temperature (800 °C) for the thermal decomposition of both, polycrystalline GaN powder [45] and GaN on  $Al_2O_3$  template in the environment without reactive  $N_2$  [61]. To reduce thermal load of hot plasma,

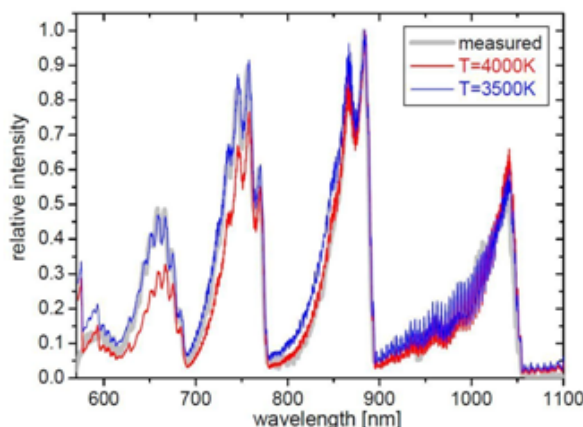


Figure 5.54.: Plasma temperature, MW power  $\approx 400$  W [197]

experiments under MW pulse mode were carried out. By applying rectangular wave with peak power value of 400 W,  $t_{ON} = 1$  ms and  $t_{OFF} = 2$  ms, the average MW power was decreased to around 133 W. Even though, experiment in the setup with reduced carbon content did not result in GaN growth.

Since the existence of GaN molecule in vapour could not be revealed by means of in situ OES and high plasma temperature prevents the formation of GaN from thermodynamic point of view, the hypothesis of Ga reacting with  $N_2^*$  in the vapour could not be proven. Two paths of GaN synthesis on the substrate at the growth conditions in our setup have been considered: direct reaction between Ga atoms and excited  $N_2$  or a route encompassing more intermediate steps, with a CN molecule involved. Neither of both paths would exclude the other one and in principle combination of these two ways would be also feasible. In the cavity, plasma burns not directly at the seed, but within the distance of couple mm (1 - 3 mm). In the model, presuming the reaction of Ga with excited  $N_2$  on the substrate, the excited nitrogen species would need to cover this distance without coming back to its ground state. In the MW pulse mode operation, the upper limit of 3 ms for  $t_{OFF}$ , still sustaining discharge, was experimentally determined.

However, all the spectra recorded under the growth conditions did not reveal bands of molecular nitrogen, but in the carbon containing setup the CN bands instead (Fig. 5.55). It indicates that CN molecule rather than the excited nitrogen itself contributes to the

GaN synthesis. In Figure 5.55 the spectrum of the growth atmosphere is shown in the range from 280 – 425 nm. The lines of neutral and ionized molecules,  $N_2^*$  and  $N_2^+$ , and atomic nitrogen N could not be detected at the growth temperature.

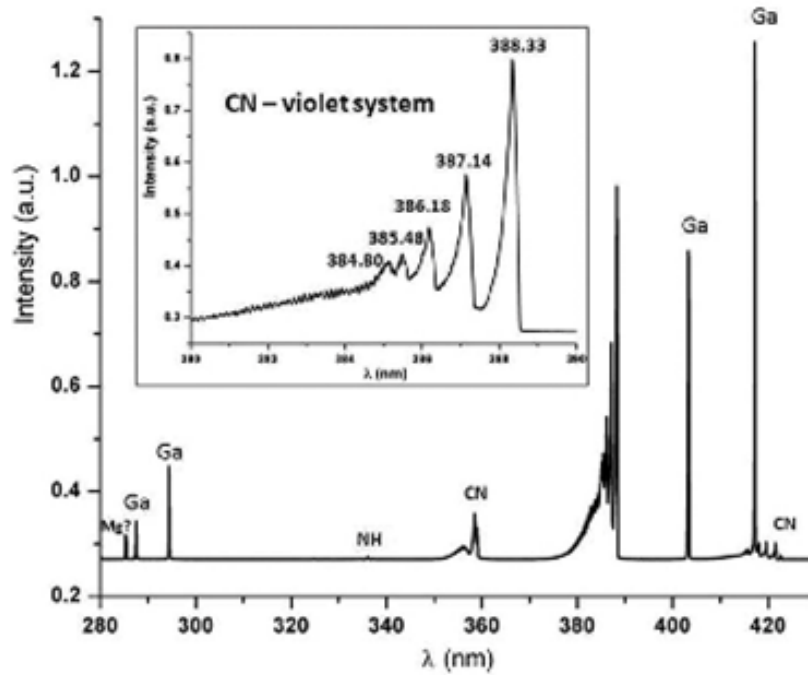
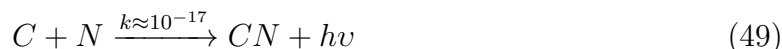


Figure 5.55.: OE spectrum of nitrogen plasma and Ga vapour under growth conditions ( $T_s = 1300\text{ }^\circ\text{C}$ ,  $p_{N_2} = 400\text{ mbar}$ ), insert: violet system of CN molecule in higher resolution. Published in [208]

Reactive nitrogen was indeed present and reacted with carbon from insulation felt and the susceptor's graphite (compare with Fig. 5.50). Moreover, the lines at 287.42, 294.4, 403.3 and 417.2 nm can be related to Ga [116]. One spectroscopic line at  $(285.23 \pm 0.15)$  nm could not be identified. The wavelength agrees with the most element-sensitive line of Mg [209], but the positions of other element sensitive lines are overlapped with strong CN emission. Furthermore, the source of Mg is unknown and the presence of Mg could not be unambiguously confirmed. CN violet system in the spectra is solid evidence that excited CN molecules are indeed present in the vapour phase. In order to exclude influence of Ga on the interactions between carbon and excited nitrogen, studies at RT have been conducted. The most effective way of CN production is the reaction between C (neutral

or excited and negatively charged) and N [196]



Cai et al. [210] suggested that the degradation of the graphite parts in their AlN sublimation equipment is the consequence of the following formation  $C(s) + x/2N_2(g) \rightarrow CN_x(g)$ . The transport of C in nitrogen plasma has been described/studied by Veprek [211], showing reaction of carbon with atomic nitrogen (weakly exothermic,  $\Delta H_{298}^0 = -4$  kcal/mole) or molecular nitrogen (strongly endothermic,  $\Delta H_{298}^0 = 109$  kcal/mole) as two possible ways of CN synthesis. Since bands of excited molecular nitrogen have been unambiguously detected in the cavity at RT, reaction of C with excited molecular nitrogen is the most likely path of CN production in the MW plasma enhanced growth of GaN at elevated pressures



The most plausible sources of carbon, necessary for the synthesis of CN, are the graphite parts in the setup, especially the isolation felt. It is made of carbon-bonded carbon fibre that tends to crumble when unintentionally scratched. Carbon dust might be formed each time during the installation of the cavity inside the reactor and the process preparation phase. It falls down onto the bottom of the susceptor, being later transported into the cavity by the rapid air flow emerging at the beginning of the pumping down or/and by the nitrogen carrier gas (its inlet is in the bottom of the crucible). Once carbon dust appears in the plasma, it stays there until being completely consumed. In the series of experiments it has been shown that intensity of CN lines increased with the MW power absorbed in the plasma.

Another aspect is the dependency of plasma composition on the total pressure in the reactor. With the increase of pressure, more carbon dust is present in the discharge

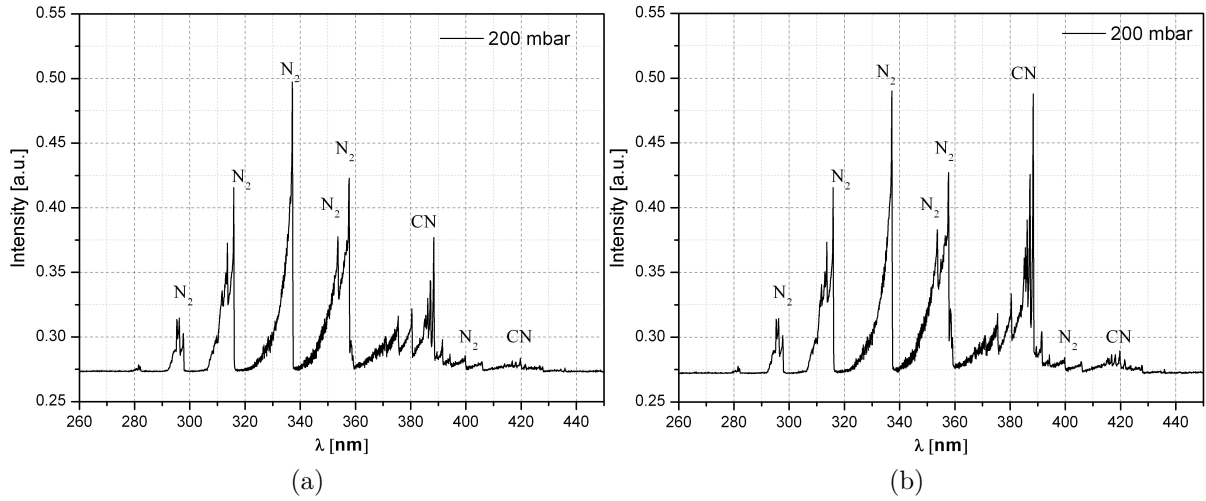
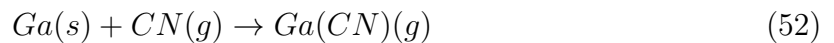


Figure 5.56.: OES recorded at RT,  $p = 200$  mbar, MW power: a)  $\approx 280$  W b)  $\approx 345$  W. Published in [208]

region. It is reflected in recorded spectra by escalating intensity of the CN bands. Concurrently, the intensity of the SPS of nitrogen has decreased (see Fig. 5.57 and 5.58).  $N_2$  has been consumed to produce CN. The observed phenomenon is in accordance with the results published by Ellahi and Ahmad [196], who studied formation of CN in  $N_2/He$  discharges in graphite hollow cathodes. The glow discharge sputters the inner walls of the graphite cathode, introducing carbon species into the plasma. Sputtering efficiency is proportional to the value of the discharge current  $i_{dis}$ , thus the higher values of  $i_{dis}$  result in the increased share of carbon dust in the plasma composition.

In 2010 our research group has identified a chemical transport by means of CN-based compounds [14] and exploited it to grow a free-standing thick bulk GaN on  $\beta$ - $Ga_2O_3$  (100) [78]. In the pseudo-HVPE technique HCN molecules are formed in the reaction of C with  $NH_3$ , which is not in use in our process. In the  $NH_3$ -free environment cyano-transport would follow the reaction of Ga with cyanide ion (Equation 52), whose formation is discussed above.





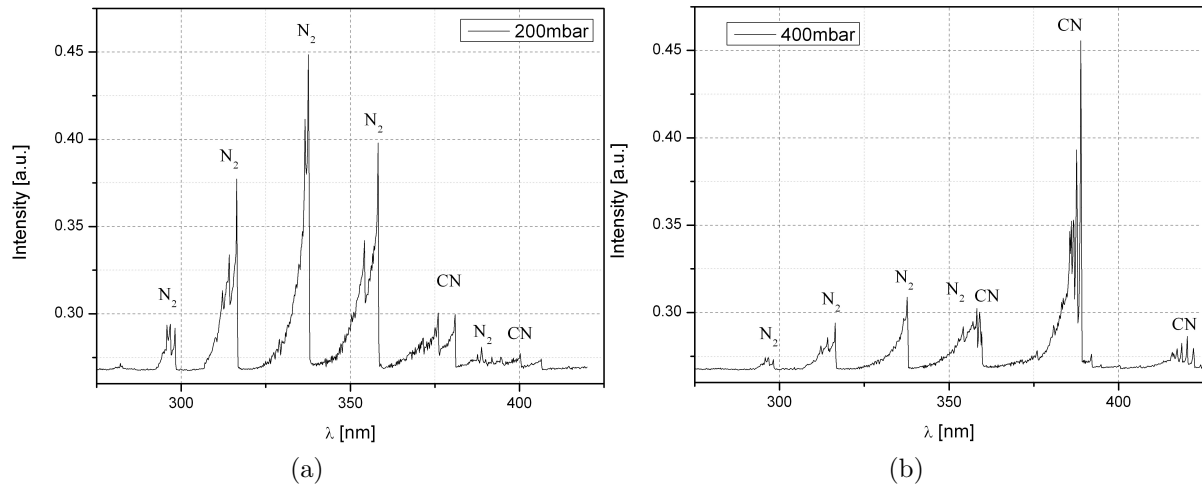


Figure 5.57.: OE spectrum recorded at RT, MW power  $\approx 400$  W, a)  $p = 200$  mbar b)  $p = 400$  mbar

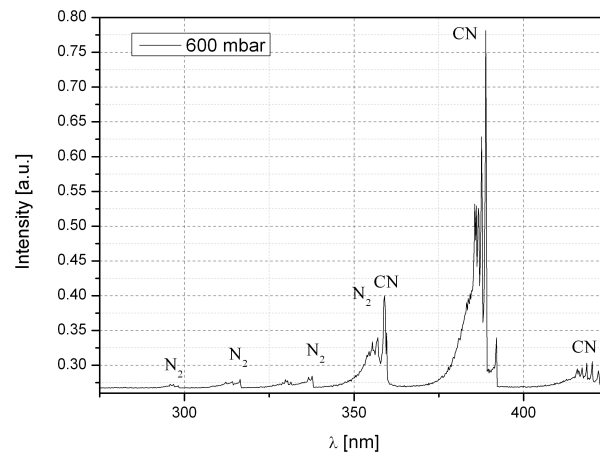
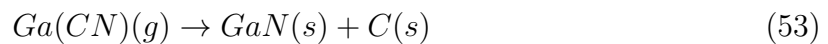


Figure 5.58.: OE spectrum recorded at RT, MW power  $\approx 400$  W,  $p = 600$  mbar

The  $Ga(CN)$  molecule would be subsequently decomposed on the seed surface into GaN and C.



C doping in GaN has been studied by many research groups. It is known, that C can act as acceptor in GaN (when located on nitrogen sites), compensating n- type residual doping by Si or O.

Traces of C have been found in the grown GaN layers, both on the surface by EDS (see Fig. 5.50 and 5.52) and beneath it by SIMS. Comparison of SIMS measured C content in GaN layers grown by Na-flux, PHVPE and MW plasma enhanced VPE (MWVPE) is presented in Fig. 5.59.

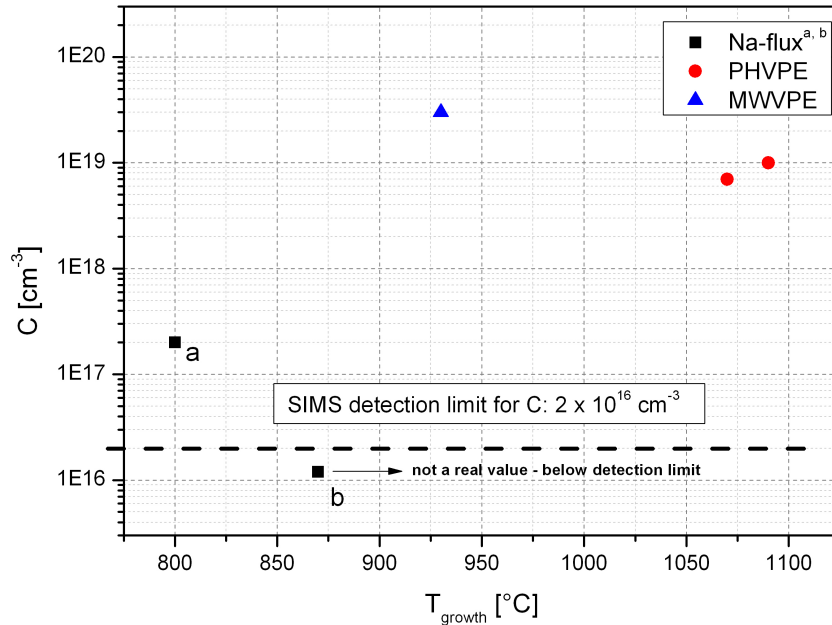


Figure 5.59.: C content in GaN layers grown by Na-flux: a [37] and b [212], PHVPE [grown by our group in IKZ, not published], and MWVPE. Measured by SIMS

Incorporation of C into growing GaN layer increases exponentially with the growth temperature  $T_{growth}$ . This tendency is visible for both PHVPE samples and one Na-flux sample, denoted as a. GaN layer grown at 930 °C by means of MWVPE revealed higher C content ( $3 \times 10^{19} cm^{-3}$ ), than in GaN PHVPE sample grown at 1070 °C ( $1 \times 10^{19} cm^{-3}$ ), though. Elevated level of C impurities might be related to local overheat of the seed surface by sub-atmospheric MW plasma, which would not be revealed by measurements of  $T_{seed}$  on the seed backside. Energy harvested in the plasma discharge by C containing species could also allow for enhanced C incorporation. Mori et al. [212] reported recently on GaN crystals with C content (denoted as b in Fig. 5.59) below SIMS detection limit, although the starting composition contained around 0.5 mol% of C.

# Chapter 6

## Summary and Outlook

Novel, MW plasma enhanced method to synthesize GaN from vapour at moderate pressure (200 - 800 mbar) has been developed. OES has been utilised for the in-situ studies of the growth atmosphere in the vicinity of the seed. GaN single crystalline layers have been grown on sapphire and on GaN templates, and characterised by means of SEM, EDX, HRXRD and SIMS.

A high-pressure plasma source was specifically designed and implemented into an existing sublimation furnace, allowing for successful,  $\text{NH}_3$ -free synthesis of GaN. Choice of materials, used for plasma source construction, was preceded by thorough studies of materials properties. In addition, the proper growth setup configuration and induction coil position was found by modelling done in HEpiGaN software. Refractory metals (Mo, Ta), in combination with Alsint 99.7 ceramics proved to be resistant to Ga vapour and high-temperature nitrogen plasma under typical growth conditions ( $T_{source} = 1300 - 1400 \text{ }^\circ\text{C}$ ,  $T_{seed} = 900 - 1000 \text{ }^\circ\text{C}$ ,  $p = 200 - 800 \text{ mbar}$ ). The MW plasma source was developed in cooperation with Dr. A. Vodopyanov from the Institute of Applied Physics of the Russian Academy of Sciences (IAP RAS) in Nizhny Novgorod, Russia. Dimensions of the resonant cavity were chosen, so as to obtain the maximum electric field intensity (at 2.45 GHz) just below the seed-holder. The selection was based on EM simulations conducted with CST MWS software. Openings in the cavity walls enabled optical access into the growth region and OES measurements.

In-situ OES studies of the reactor atmosphere revealed that the vapour in the growth region is composed of Ga,  $\text{N}_2^*$  and CN, rather than only Ga and  $\text{N}_2^*$ . CN bands, constituting the CN violet system were observed in the regions of 358 - 360 nm, 380 - 390 nm and 415 - 420 nm. The recorded bands of molecular nitrogen with band heads at 297.68 nm,

315.93 nm, 337.13 nm, 357.69 nm belong to the second positive nitrogen system (SPS) ( $C^3\Pi_u - B^3\Pi_g$ ). Sharp Ga lines appeared in spectra with increase of  $T_{source}$ , thus increase of Ga vapour pressure in the reactor. The most prominent Ga lines were recorded at 403.3 nm and 417.2 nm and belong to the so called persistent lines of Ga. Interaction of Ga vapour with MW nitrogen plasma in the pressure range of 200 - 800 mbar does not lead to the extinction of the latter. Nevertheless, influence of Ga on emission processes in high-temperature plasma has been disclosed. As soon as Ga vapour reaches the MW discharge, intensity of Ga lines increases, being accompanied by the decrease of CN and  $N_2^*$  bands intensity. This phenomenon has been explained by the fact that energy levels of Ga excited states (for instance 3.07 eV for 403.3 nm and 417.2 nm lines) are located below the energy levels of excited nitrogen (6.17 eV for  $A^3\Sigma_u^+$  state) and CN (3.19 eV for the band at 388.3 nm). In order to rule out the C impact on Ga -  $N_2^*$  interactions, experiments in C-free setup have been carried out. They were not successful, due to lack of carbon, which would normally reduce residual oxygen present in the reactor. Therefore, studies in the growth setup with reduced C content have been conducted. Their results suggest that most of the MW energy is consumed by Ga atoms and the number of fast electrons able to excite nitrogen decreases significantly. Furthermore, the outcomes are consistent with observations made by Corr et al. [187], stating that Ga atoms are excited in the collisions with the excited nitrogen species. Consequently, transition of Ga atoms to the ground state results in the strong emission in VIS/UV region of spectra.

Experimental procedure for growth of GaN single crystalline layers from vapour by means of MW plasma enhanced method has been developed. Morphology of GaN film surface has been studied by SEM. In case of GaN growth on sapphire, typical, pyramidal structures have been observed. Growth under Ga excess lead to an uncoalesced GaN layer with small pits on their top surface, as Ga is known to etch GaN. Formation of GaN on the GaN template was hindered by the unstable plasma operation, thus limiting  $T_{seed}$  to 900 °C. Therefore, 3D growth mode prevailed and GaN islands were not completely consolidated.

Plausible paths for GaN formation in the MW plasma assisted process have been dis-

---

cussed. GaN molecules have not been identified in spectra recorded in the 200 - 1100 nm range. Even if GaN were formed in vapour, they would be immediately decomposed by high plasma temperature ( $T \approx 4000\text{ K}$ ). Accordingly, GaN formation on the seed has been taken under consideration. It has been found out that CN molecule rather than  $\text{N}_2^*$  contributes to the GaN synthesis. Growth of GaN was observed only in the growth setup containing C, and consequently C has been found in the grown GaN layers by EDX and SIMS. Furthermore, none of the OE spectra recorded under the growth conditions disclosed bands of  $\text{N}_2^*$ , yet CN violet system. Therefore, it is proposed that GaN formation in our  $\text{NH}_3$ -free growth system resembles pseudo-HVPE technique. Reaction of Ga and CN in the vapour produces GaCN, which is further decomposed on the seed surface into GaN and C.

The presented studies demonstrate the development of a new technique to grow GaN single crystalline layers from vapour. Its novelty lies in concurrent formation of MW nitrogen plasma in the vicinity of the seed, at moderate pressure (200 – 800 mbar) and combined PVT and CVT of Ga to the seed. Furthermore, thermally unstable, aggressive and poisonous  $\text{NH}_3$  has been replaced in the system by nitrogen plasma. It has been demonstrated that this method is able to provide GaN single crystalline layers in the  $\text{H}_2$ -free environment. On the other hand, it is not favourable for GaN bulk growth and not competitive with HVPE. Improved control of the CN formation in the growth region and long-term plasma stability could result in thick GaN layers. Yet, for controlled C doping of GaN, PHVPE without MW plasma source can be utilised as well. The in situ OES studies of the growth region proved the absence of GaN molecule in the vapour.



# Appendices





# Appendix A

## Material properties

### A.1. Ceramics

Table 4.: Ceramics

material	data source	$T_{max}$ [°C]	$\rho$ [ $\Omega cm$ ]		
			RT	500 °C	1000 °C
Al <sub>2</sub> O <sub>3</sub>	Createc, Al300	1650	$> 10^{14}$	<sup>a)</sup> $2.3 \times 10^{10}$	$5 \times 10^8$
	BCE- ceramics	1650	$> 10^{14}$	<sup>b)</sup> $10^{12}$	$10^7$
	Friatec, F99.7	1650	$10^{15}$	$10^{11}$	$10^7$
	Degussit	1950	$10^{14}$	<sup>b)</sup> $10^{11}$	-
MgO	-	-	$10^{14}$	<sup>a)</sup> $10^9$	-
MgO	[213], p.404	-	$1.3 \times 10^{15}$	-	$(0.2 - 1) \times 10^8$
AlTi	ATI	900 - 1600	$10^{14}$	-	$10^9$
BN	BCE, BN500	<sup>c)</sup> 2400	$10^{14}$	-	$10^9$
	[213], p.404	-	-	-	$3 \times 10^4$
BeO	[213], p.408	$> 2000$	$> 10^{17}$	$(1 - 5) \times 10^{15}$	$(4 - 7) \times 10^{15}$
Y <sub>2</sub> O <sub>3</sub>	[214]	2680	$> 10^{15}$	$1.2 \times 10^{10}$	$(5 - 10) \times 10^4$
ZrC	[213], p.404	-	-	-	$1.4 \times 10^8$
ZrN	[213], p.404	-	-	-	<sup>d)</sup> $3.2 \times 10^8$
TiN	[213], p.404	-	-	-	<sup>d)</sup> $3.4 \times 10^8$
MoSi <sub>2</sub>	[213], p.404	-	-	-	<sup>e)</sup> $(7.5 - 8) \times 10^7$

a) at 600 °C, b) at 400 °C, c) O<sub>2</sub> free, d) at its melting point  $T_m$ , e) at 1600 °C

## A.2. Refractory metals

Table 5.: Refractory metals [159, 162, 200, 215, 216]

material	<sup>a)</sup> r	<sup>b)</sup> T <sub>m</sub> [°C]	<sup>c)</sup> Φ[eV]	<sup>d)</sup> λ[W/mK]	<sup>e)</sup> σ[1/Ωm]	<sup>f)</sup> T <sub>r</sub> [°C]
Mo	421	2620	4.39	140	17.9 × 10 <sup>6</sup>	900 - 1100
W	340	3420	4.54	164	18 × 10 <sup>6</sup>	1300 - 1500
Ta	380	2966	4.25	54	8 × 10 <sup>6</sup>	900 - 1450
Nb	390	2468	4.36	52	7 × 10 <sup>6</sup>	900 - 1450
Ti	336	1668	4.33	22	2.5 × 10 <sup>6</sup>	885

a) sputter rate - measured for E = 500 eV Argon ions at 1 mA/cm<sup>2</sup>, normal ion beam incidence, b) melting point, c) electron work function, d) thermal conductivity (at 20 °C), e) electrical conductivity (at 20 °C), f) recrystallization temperature

Table 6.: Refractory metals [159, 162, 200, 215, 216]

material	resistance towards molten Ga	resistance towards nitrogen	*hardness		weldability
			cold- worked	recrystallized	
Mo	< 300 °C	resistant	200 – 250	160 – 210	TIG, EB <sup>a)</sup>
W	< 1000 °C	resistant	> 460	360	TIG <sup>b)</sup> , EB <sup>a)</sup>
Ta	< 450 °C	< 700 °C	120 – 220	80 – 125	TIG, EB <sup>a)</sup> , laser
Nb	< 400 °C	< 300 °C	110 – 180	60 – 110	TIG, EB <sup>a)</sup> , laser
Ti	< 400 °C	< 538 °C	180 – 240	140 – 155	TIG

\*hardness in diamond pyramide scale HV10 HV30

a) in vacuum, b) in a glove box

# Appendix B

## Calculations

### B.1. Thermal expansion coefficient of Mo

Interpolation formula for thermal expansion coefficient for molybdenum within RT – 1500 °C range.

$$y = ax + b$$

$$\alpha_1(@400\text{ °C}) = 5.4 [m/(mK)] \times 10^{-6}$$

$$\alpha_2(@1200\text{ °C}) = 6 [m/(mK)] \times 10^{-6}$$

$$\begin{cases} 6 \times 10^{-6} = 1200a + b \\ 5.4 \times 10^{-6} = 400a + b \end{cases} \quad \begin{cases} a = 0.075 \times 10^{-8} [m/(mK^2)] \\ b = 5.1 \times 10^{-6} [m/(mK)] \end{cases}$$

$$\alpha_L = 0.075 \times 10^{-8} [m/mK^2] \times T [^\circ\text{C}] + 5.1 \times 10^{-6} [m/(mK)] \quad (54)$$

### B.2. Change of the cavity diameter

Change of the cavity diameter  $\Delta D$  due to thermal expansion while heating up from RT to 1330 °C

$$\begin{cases} \alpha_L = 0.075 \times 10^{-8} [m/mK^2] \times T [^\circ\text{C}] + 5.1 \times 10^{-6} [m/(mK)] \\ \alpha_L = \frac{1}{D} \frac{dD}{dT} \\ \Delta D = D \int_{T_1}^{T_2} \alpha_L dT \end{cases}$$

$$\Delta D = D \int_{30}^{1330} (0.075 \times 10^{-8} \times T + 5.1 \times 10^{-6}) dT = 0.6564 \text{ mm}$$

### **B.3. Resonance frequency shift - estimations**

Estimations of the resonant frequency shift by changing the axial position of the cavity.

- initial position of the cavity  $\rightarrow f_r = 2.45$  GHz

- final position of the cavity  $\rightarrow f_r = 2.404$  GHz

$$\Delta f_r = 0.046 \text{ GHz}$$

- distance traveled by the cavity axially: 4 mm

$$\Delta f_r \text{ per } 1 \text{ mm} = 0.0092 \text{ GHz/mm}$$

# Appendix C

## Experiments

Table 7.: Experiments described in the thesis - parameters

Exp.	p [mbar]	T <sub>seed</sub> [°C]	T <sub>source</sub> [°C]	<sup>a)</sup> N <sub>2</sub> [slm]	MW power [W]	t <sub>growth</sub> [h]	seed
MP2	200	<sup>b)</sup> 1100	1450	0.2	300	4.5	1)
MP4	600	<sup>b)</sup> 905	1345	0.2	520	6	2)
MP5	200	<sup>b)</sup> 990	1430	0.2	550	4.5	2)
MP11	200	1000	1225	0.1	400	3	3)
MP21	400	990	1400	0.1	430	5	1)
MP22	600	990	1370	0.2	450	5	1)
MP26	600	980	1300	0.2	450	5	3)
MP30	400	865	1300	0.1	400	5	4)
MP32	400	940	1240	0.1	380	5	1)
MP46	200	900	1300	0.1	400	5	3)

a) carrier gas flow, b) T<sub>flange</sub> measured with thermocouple,

1) Al<sub>2</sub>O<sub>3</sub>, 2) AlN/Al<sub>2</sub>O<sub>3</sub> template, 3) GaN/Al<sub>2</sub>O<sub>3</sub> template, 4) AlGaN/GaN/Al<sub>2</sub>O<sub>3</sub> template



# Appendix D

## Second positive system of N<sub>2</sub>

Table 8.: Second Positive System of N<sub>2</sub>, in the range of 280 - 450 nm

$\lambda$ [nm]	I (rel.)	E [eV]	Transition	Quantum number
281.4300	100	7.39 - 11.05	$B^3\Pi_g - C^3\Pi_u$	1 - 4
281.9800	100	7.39 - 11.05	$B^3\Pi_g - C^3\Pi_u$	0 - 3
295.3200	600	7.39 - 11.05	$B^3\Pi_g - C^3\Pi_u$	2 - 4
296.2000	600	7.39 - 11.05	$B^3\Pi_g - C^3\Pi_u$	1 - 3
297.6800	600	7.39 - 11.05	$B^3\Pi_g - C^3\Pi_u$	0 - 2
297.6800	600	7.39 - 11.05	$B^3\Pi_g - C^3\Pi_u$	0 - 2
310.4000	300	7.39 - 11.05	$B^3\Pi_g - C^3\Pi_u$	3 - 4
311.6700	600	7.39 - 11.05	$B^3\Pi_g - C^3\Pi_u$	2 - 3
313.6000	800	7.39 - 11.05	$B^3\Pi_g - C^3\Pi_u$	1 - 2
315.9300	900	7.39 - 11.05	$B^3\Pi_g - C^3\Pi_u$	0 - 1
326.8100	400	7.39 - 11.05	$B^3\Pi_g - C^3\Pi_u$	4 - 4
328.5300	300	7.39 - 11.05	$B^3\Pi_g - C^3\Pi_u$	3 - 3
330.9000	200	7.39 - 11.05	$B^3\Pi_g - C^3\Pi_u$	2 - 2
333.9000	200	7.39 - 11.05	$B^3\Pi_g - C^3\Pi_u$	1 - 1
337.1300	1000	7.39 - 11.05	$B^3\Pi_g - C^3\Pi_u$	0 - 0
350.0500	400	7.39 - 11.05	$B^3\Pi_g - C^3\Pi_u$	3 - 2
353.6700	800	7.39 - 11.05	$B^3\Pi_g - C^3\Pi_u$	2 - 1
357.6900	1000	7.39 - 11.05	$B^3\Pi_g - C^3\Pi_u$	1 - 0
364.1700	300	7.39 - 11.05	$B^3\Pi_g - C^3\Pi_u$	6 - 4
367.1900	600	7.39 - 11.05	$B^3\Pi_g - C^3\Pi_u$	5 - 3
371.0500	800	7.39 - 11.05	$B^3\Pi_g - C^3\Pi_u$	4 - 2
375.5400	1000	7.39 - 11.05	$B^3\Pi_g - C^3\Pi_u$	3 - 1
380.4900	1000	7.39 - 11.05	$B^3\Pi_g - C^3\Pi_u$	2 - 0
385.7900	500	7.39 - 11.05	$B^3\Pi_g - C^3\Pi_u$	7 - 4
389.4600	700	7.39 - 11.05	$B^3\Pi_g - C^3\Pi_u$	6 - 3
394.3000	800	7.39 - 11.05	$B^3\Pi_g - C^3\Pi_u$	5 - 2
399.8400	900	7.39 - 11.05	$B^3\Pi_g - C^3\Pi_u$	4 - 1
405.9400	800	7.39 - 11.05	$B^3\Pi_g - C^3\Pi_u$	3 - 0
409.4800	400	7.39 - 11.05	$B^3\Pi_g - C^3\Pi_u$	8 - 4
414.1800	500	7.39 - 11.05	$B^3\Pi_g - C^3\Pi_u$	7 - 3
420.0500	600	7.39 - 11.05	$B^3\Pi_g - C^3\Pi_u$	6 - 2
426.9700	500	7.39 - 11.05	$B^3\Pi_g - C^3\Pi_u$	5 - 1
434.3600	400	7.39 - 11.05	$B^3\Pi_g - C^3\Pi_u$	4 - 0
435.5000	400	7.39 - 11.05	$B^3\Pi_g - C^3\Pi_u$	9 - 4
441.6700	300	7.39 - 11.05	$B^3\Pi_g - C^3\Pi_u$	8 - 3
449.0200	300	7.39 - 11.05	$B^3\Pi_g - C^3\Pi_u$	7 - 2





# Bibliography

- [1] H. P. Maruska, “The preparation and properties of vapor-deposited single-crystalline GaN,” *Applied Physics Letters*, vol. 15, no. 10, p. 327, 1969. [Online]. Available: <http://link.aip.org/link/?APL/15/327/1&Agg=doi>
- [2] J. I. Pankove, “GaN Electroluminescent Diodes,” *RCA Review*, vol. 32, pp. 383–392, 1971.
- [3] I. Akasaki, H. Amano, Y. Koide, K. Hiramatsu, and N. Sawaki, “Effects of AlN buffer layer on crystallographic structure and on electrical and optical properties of GaN and GaAlN films grown on sapphire substrate by MOVPE,” *Journal of Crystal Growth*, vol. 98, no. 1-2, pp. 209–219, 1989. [Online]. Available: <http://www.sciencedirect.com/science/article/pii/0022024889902005>
- [4] S. Nakamura, T. Mukai, and M. Senoh, “Candela-class high-brightness InGaN/AlGaIn double-heterostructure blue-light-emitting diodes,” *Applied Physics Letters*, vol. 64, no. 13, p. 1687, Mar. 1994. [Online]. Available: <http://scitation.aip.org/content/aip/journal/apl/64/13/10.1063/1.111832>
- [5] S. Nakamura, M. Senoh, S.-i. Nagahama, T. Matsushita, H. Kiyoku, Y. Sugimoto, T. Kozaki, H. Umemoto, M. Sano, and T. Mukai, “Violet InGaIn/GaN/AlGaIn-Based Laser Diodes Operable at 50°C with a Fundamental Transverse Mode,” *Japanese Journal of Applied Physics*, vol. 38, no. 3, pp. L226–L229, Mar. 1999. [Online]. Available: <http://jjap.jsap.jp/link?JJAP/38/L226/>
- [6] Pcmag.com, “Samsung Ships the First Blu-Ray Player,” 2006. [Online]. Available: <http://www.pcmag.com/article2/0,2817,1977327,00.asp>
- [7] Techspot.com, “Sony ships their first Blu-Ray player,” 2006. [Online]. Available: <http://www.techspot.com/news/23726-sony-ships-their-first-blu-ray-player.html>
- [8] E. F. Schubert, *Light-Emitting Diodes*. Cambridge University Press, 2006.
- [9] Ioffe Institute, “NSM Archive - Gallium Nitride (GaN).” [Online]. Available: <http://www.ioffe.rssi.ru/SVA/NSM/Semicond/GaN/index.html>
- [10] W. Utsumi, H. Saitoh, H. Kaneko, T. Watanuki, K. Aoki, and O. Shimomura, “Congruent melting of GaN at 6 GPa and its application to single-crystal growth,” *Nature materials*, vol. 2, no. 11, pp. 735–738, 2003.
- [11] H. Morkoc, *Handbook of Nitride Semiconductors and Devices*. Weinheim: John Wiley & Sons, 2009, vol. 1.
- [12] J. Karpinski and S. Porowski, “High Pressure Thermodynamics of GaN,” *Journal of Crystal Growth*, vol. 66, pp. 11–20, 1984. [Online]. Available: <http://www.sciencedirect.com/science/article/pii/002202488490071X>
- [13] Z. Sitar and R. Schlessler, “Growth of Single Crystals and Fabrication of GaN and AlN Wafers,” North Carolina State University, Raleigh, Tech. Rep., 2006. [Online]. Available: <http://www.dtic.mil/dtic/tr/fulltext/u2/a444058.pdf>

- [14] K. Jacobs, D. Siche, D. Klimm, H.-J. Rost, and D. Gogova, "Pseudohalide vapour growth of thick GaN layers," *Journal of Crystal Growth*, vol. 312, no. 6, pp. 750–755, Mar. 2010. [Online]. Available: <http://linkinghub.elsevier.com/retrieve/pii/S002202480901152X>
- [15] E. Richter, M. Gründer, C. Netzel, M. Weyers, and G. Tränkle, "Growth of GaN boules via vertical HVPE," *Journal of Crystal Growth*, vol. 350, no. 1, pp. 89–92, Jul. 2012. [Online]. Available: <http://linkinghub.elsevier.com/retrieve/pii/S0022024811010499>
- [16] M. Bockowski, P. Strak, I. Grzegory, B. Lucznik, and S. Porowski, "GaN crystallization by the high-pressure solution growth method on HVPE bulk seed," *Journal of Crystal Growth*, vol. 310, no. 17, pp. 3924–3933, Aug. 2008. [Online]. Available: <http://linkinghub.elsevier.com/retrieve/pii/S0022024808004533>
- [17] Y. Mori, M. Imade, K. Murakami, H. Takazawa, H. Imabayashi, Y. Todoroki, K. Kitamoto, M. Maruyama, M. Yoshimura, Y. Kitaoka, and T. Sasaki, "Growth of bulk GaN crystal by Na flux method under various conditions," *Journal of Crystal Growth*, vol. 350, no. 1, pp. 72–74, Jul. 2012. [Online]. Available: <http://linkinghub.elsevier.com/retrieve/pii/S0022024811010451>
- [18] R. Dwiliński, R. Doradziński, J. Garczyński, L. Sierzputowski, a. Puchalski, Y. Kanbara, K. Yagi, H. Minakuchi, and H. Hayashi, "Excellent crystallinity of truly bulk ammonothermal GaN," *Journal of Crystal Growth*, vol. 310, no. 17, pp. 3911–3916, Aug. 2008. [Online]. Available: <http://linkinghub.elsevier.com/retrieve/pii/S002202480800451X>
- [19] Y. Mikawa, H. Fujisawa, K. Kamada, M. Saito, S. Kawabata, Y. Kagamitani, and T. Fujimori, "Bulk GaN crystals grown by Acidic Ammonothermal Technology," in *IWN 2012*, vol. 1041, no. 2009, Sapporo, Japan, 2012, pp. 1–2.
- [20] T. Ozawa, M. Dohi, T. Matsuura, and Y. Hayakawa, "Solution growth of GaN on sapphire substrate under nitrogen plasma," *Journal of Crystal Growth*, vol. 311, no. 3, pp. 440–442, Jan. 2009. [Online]. Available: <http://linkinghub.elsevier.com/retrieve/pii/S0022024808008361>
- [21] S. V. Novikov, C. R. Staddon, R. E. L. Powell, a. V. Akimov, a. J. Kent, and C. T. Foxon, "Plasma-assisted electroepitaxy as a novel method for the growth of GaN layers," *Physica Status Solidi (C)*, vol. 9, no. 3-4, pp. 538–541, Mar. 2012. [Online]. Available: <http://doi.wiley.com/10.1002/pssc.201100297>
- [22] S. Porowski, "High pressure growth of GaN – new prospects for blue lasers," *Journal of Crystal Growth*, vol. 166, no. 1-4, pp. 583–589, 1996. [Online]. Available: <http://www.sciencedirect.com/science/article/pii/0022024896001169>
- [23] P. Bhattacharya, R. Fornari, H. Kamimura, and R. Fornari, "Bulk Crystal Growth of Semiconductors: An Overview," in *Comprehensive Semiconductor Science and Technology*, 2011, pp. 1–35. [Online]. Available: <http://www.sciencedirect.com/science/article/pii/B9780444531537000882>
- [24] I. Grzegory, B. Łucznik, M. Boćkowski, and S. Porowski, "Crystallization of low dislocation density GaN by high-pressure solution and HVPE methods," *Journal*

- of *Crystal Growth*, vol. 300, no. 1, pp. 17–25, Mar. 2007. [Online]. Available: <http://linkinghub.elsevier.com/retrieve/pii/S0022024806011821>
- [25] M. Bockowski, B. Lucznik, T. Sochacki, B. Sadovyi, G. Nowak, E. Litwin-Staszewska, and I. Grzegory, “High nitrogen pressure solution growth of GaN in multi feed-seed configuration,” *Physica Status Solidi (C)*, vol. 9, no. 3-4, pp. 453–456, Mar. 2012. [Online]. Available: <http://doi.wiley.com/10.1002/pssc.201100366>
- [26] R. Dwiliński, R. Doradziński, J. Garczyński, L. Sierzputowski, R. Kucharski, M. Zając, M. Rudziński, R. Kudrawiec, W. Strupiński, and J. Misiewicz, “Ammonothermal GaN substrates: Growth accomplishments and applications,” *Physica Status Solidi (a)*, vol. 208, no. 7, pp. 1489–1493, Jul. 2011. [Online]. Available: <http://doi.wiley.com/10.1002/pssa.201001196>
- [27] M. D. Govindhan Dhanaraj, Kullaiyah Byrappa, Vishwanath Prasad, Ed., *Handbook of Crystal Growth*, 2010th ed. Springer, 2010.
- [28] R. Kucharski, M. Zając, R. Doradziński, M. Rudziński, R. Kudrawiec, and R. Dwiliński, “Non-polar and semi-polar ammonothermal GaN substrates,” *Semiconductor Science and Technology*, vol. 27, no. 2, p. 024007, Feb. 2012. [Online]. Available: <http://stacks.iop.org/0268-1242/27/i=2/a=024007?key=crossref.eb81ac41ca76b50d6e80569dfaced0c0>
- [29] T. Fukuda and D. Ehretraut, “Prospects for the ammonothermal growth of large GaN crystal,” *Journal of Crystal Growth*, vol. 305, no. 2, pp. 304–310, Jul. 2007. [Online]. Available: <http://linkinghub.elsevier.com/retrieve/pii/S002202480700382X>
- [30] R. Dwiliński, R. Doradziński, J. Garczyński, L. Sierzputowski, a. Puchalski, Y. Kanbara, K. Yagi, H. Minakuchi, and H. Hayashi, “Bulk ammonothermal GaN,” *Journal of Crystal Growth*, vol. 311, no. 10, pp. 3015–3018, May 2009. [Online]. Available: <http://linkinghub.elsevier.com/retrieve/pii/S0022024809000906>
- [31] K. Yoshida, K. Aoki, and T. Fukuda, “High-temperature acidic ammonothermal method for GaN crystal growth,” *Journal of Crystal Growth*, pp. 1–5, Sep. 2013. [Online]. Available: <http://linkinghub.elsevier.com/retrieve/pii/S0022024813006039>
- [32] D. Ehretraut, R. T. Pakalapati, D. S. Kamber, W. Jiang, D. W. Pocius, B. C. Downey, M. Mclaurin, and M. P. . D’Evelyn, “High Quality, Low Cost Ammonothermal Bulk GaN Substrates,” *Japanese Journal of Applied Physics*, vol. 52, no. 2, No.8, pp. 1–4, 2013. [Online]. Available: <http://jjap.jsap.jp/link?JJAP/52/08JA01/pdf>
- [33] Ammono, “www.ammono.pl.” [Online]. Available: [www.ammono.pl](http://www.ammono.pl)
- [34] H. Yamane, M. Shimada, S. J. Clarke, and F. J. DiSalvo, “Preparation of GaN Single Crystals Using a Na Flux,” *Chem. Mater.*, vol. 9, no. 2, pp. 413–416, 1997.
- [35] T. Shin, H. Lee, J. Lee, S.-W. Kim, S. Suh, and D. Yoon, “Bulk GaN single crystal growth and characterization using various alkali metal flux,” *Journal of Crystal Growth*, vol. 292, no. 2, pp. 216–220, Jul. 2006. [Online]. Available: <http://linkinghub.elsevier.com/retrieve/pii/S002202480600306X>

- [36] H. Yamane, D. Kinno, M. Shimada, T. Sekiguchi, and F. J. Disalvo, "GaN single crystal growth from a Na-Ga melt," *Journal of Materials Science*, vol. 35, no. 4, pp. 801–808, 2000. [Online]. Available: <http://link.springer.com/article/10.1023%2FA%3A1004713400790>
- [37] F. Kawamura, M. Morishita, M. Tanpo, M. Imade, M. Yoshimura, Y. Kitaoka, Y. Mori, and T. Sasaki, "Effect of carbon additive on increases in the growth rate of 2in GaN single crystals in the Na flux method," *Journal of Crystal Growth*, vol. 310, no. 17, pp. 3946–3949, Aug. 2008. [Online]. Available: <http://linkinghub.elsevier.com/retrieve/pii/S0022024808004569>
- [38] Y. Song, W. Wang, W. Yuan, X. Wu, and X. Chen, "Bulk GaN single crystals: growth conditions by flux method," *Journal of Crystal Growth*, vol. 247, no. 3-4, pp. 275–278, Jan. 2003. [Online]. Available: <http://linkinghub.elsevier.com/retrieve/pii/S0022024802020146>
- [39] W. C. Johnson, J. B. Parsons, and M. C. Crew, "NITROGEN COMPOUNDS OF GALLIUM," *J. Am. Chem. Soc.*, vol. 52, p. 2651, 1930.
- [40] F. Kawamura, M. Morishita, K. Omae, M. Yoshimura, Y. Mori, and T. Sasaki, "The effects of Na and some additives on nitrogen dissolution in the Ga-Na system: A growth mechanism of GaN in the Na flux method," *Journal of Materials Science: Materials in Electronics*, vol. 16, no. 1, pp. 29–34, Jan. 2005. [Online]. Available: <http://link.springer.com/10.1007/s10854-005-4955-8>
- [41] D. Elwell and M. M. Elwell, "Crystal growth of gallium nitride," *Prog. Crystal Growth and Charact.*, vol. 17, no. 1, pp. 53–78, 1988. [Online]. Available: <http://www.sciencedirect.com/science/article/pii/0146353588900056>
- [42] C. Balkaş, Z. Sitar, L. Bergman, I. Shmagin, J. Muth, R. Kolbas, R. Nemanich, and R. Davis, "Growth and characterization of GaN single crystals," *Journal of Crystal Growth*, vol. 208, no. 1-4, pp. 100–106, Jan. 2000. [Online]. Available: <http://linkinghub.elsevier.com/retrieve/pii/S0022024899004455>
- [43] R. B. Zetterstorm, "Synthesis and growth of single crystals of gallium nitride," *Journal of Materials Science*, vol. 5, p. 1102, 1970.
- [44] D. D. Manchon, A. S. Barker, P. J. Dean, and R. B. Zetterstrom, "Optical studies of the phonons and electrons in gallium nitride," *Solid State Comm.*, vol. 8, p. 1227, 1970.
- [45] R. C. Schoonmaker, A. Buhl, and J. Lemley, "Vaporization Catalysis. The Decomposition of Gallium Nitride," *The Journal of Physical Chemistry*, vol. 69, no. 10, pp. 3455–3460, 1965.
- [46] D. Siche, H.-J. Rost, K. Böttcher, D. Gogova, and R. Fornari, "Growth of GaN crystals from chlorine-free gas phase," *Journal of Crystal Growth*, vol. 310, no. 5, pp. 916–919, Mar. 2008. [Online]. Available: <http://linkinghub.elsevier.com/retrieve/pii/S002202480701041X>

- [47] C. Wetzel, D. Volm, B. K. Meyer, K. Pressel, S. Nilsson, E. N. Mokhov, and P. G. Baranov, "GaN epitaxial layers grown on 6H-SiC by the sublimation sandwich technique," *Applied Physics Letters*, vol. 65, no. 8, p. 1033, 1994. [Online]. Available: <http://link.aip.org/link/APPLAB/v65/i8/p1033/s1&Agg=doi>
- [48] S. Fischer, C. Wetzel, W. L. Hansen, E. D. Bourret-Courchesne, B. K. Meyer, and E. E. Haller, "Properties of GaN grown at high rates on sapphire and on 6H-SiC," *Applied Physics Letters*, vol. 69, no. 18, pp. 2716–2718, 1996. [Online]. Available: [http://homepages.rpi.edu/~sim\\$wetzel/Preprints/APLFischerGaNhighratesbySublimationAppl.Phys.Lett.69,2716%281996%29.pdf](http://homepages.rpi.edu/~sim$wetzel/Preprints/APLFischerGaNhighratesbySublimationAppl.Phys.Lett.69,2716%281996%29.pdf)
- [49] Y. A. Vodakov, E. N. Mokhov, A. D. Roenkov, M. E. Boiko, and P. G. Baranov, "High rate GaN epitaxial growth by sublimation sandwich method," *Journal of Crystal Growth*, vol. 183, no. 1-2, pp. 10–14, Jan. 1998. [Online]. Available: <http://linkinghub.elsevier.com/retrieve/pii/S0022024897004132>
- [50] Kurai Satoshi, "Growth and Characterization of Thick GaN by Sublimation Method and Homoepitaxial Growth by Metalorganic Vapor Deposition," *Japanese Journal of Applied Physics*, vol. 35, pp. 1637–1640, 1996. [Online]. Available: <http://jjap.jsap.jp/link?JJAP/35/1637/>
- [51] P. Ruterana, M. Albrecht, and J. Neugebauer, Eds., *Nitride Semiconductors: Handbook on Materials and Devices*. WILEY-VCH Verlag GmbH & Co.KGaA, 2006.
- [52] T. Liang, J. Tang, J. Xiong, Y. Wang, C. Xue, X. Yang, and W. Zhang, "Synthesis and characterization of heteroepitaxial GaN films on Si(111)," *Vacuum*, vol. 84, no. 9, pp. 1154–1158, Apr. 2010. [Online]. Available: <http://linkinghub.elsevier.com/retrieve/pii/S0042207X10000783>
- [53] J. Wang, H.-B. Ryu, M.-S. Park, W.-J. Lee, Y.-J. Choi, and H.-Y. Lee, "Epitaxy of GaN on Si(111) substrate by the hydride vapor phase epitaxy method," *Journal of Crystal Growth*, vol. 370, pp. 249–253, May 2013. [Online]. Available: <http://linkinghub.elsevier.com/retrieve/pii/S0022024812006033>
- [54] T. Sochacki, M. Amilusik, B. Lucznik, M. Bockowski, M. Fijalkowski, R. Kucharski, M. Zajac, R. Doradzinski, R. Dwilinski, and I. Grzegory, "HVPE GaN growth on misoriented ammonothermal GaN seeds," in *IWBNS VIII 2013*, Seon, 2013.
- [55] S. Park, M. Lee, D. Mikulik, J. Kim, Y. Tak, J. Kim, and Y. Park, "The fabrication of freestanding GaN on Si substrate by HVPE," in *IWBNS VIII 2013*, Seon, 2013.
- [56] K. Fujito, S. Kubo, H. Nagaoka, T. Mochizuki, H. Namita, and S. Nagao, "Bulk GaN crystals grown by HVPE," *Journal of Crystal Growth*, vol. 311, no. 10, pp. 3011–3014, May 2009. [Online]. Available: <http://linkinghub.elsevier.com/retrieve/pii/S002202480900089X>
- [57] Sumitomo, "Sumitomo Electric Industries, Ltd. | Press Release (2010) Sumitomo Electric announces the World's First 6-inch GaN Substrates for White LED Applications." [Online]. Available: [http://global-sei.com/news/press/10/10\\_23.html](http://global-sei.com/news/press/10/10_23.html)

- [58] H.-J. Rost, D. Siche, D. Gogova, M. Albrecht, K. Jacobs, and R. Fornari, “The role of carbon in transport processes during PVT growth of bulk GaN,” *Physica Status Solidi (C)*, vol. 1487, no. 6, pp. 1484–1487, 2009. [Online]. Available: <http://onlinelibrary.wiley.com/doi/10.1002/pssc.200881523/abstract>
- [59] R. E. Honig and D. A. Kramer, “Vapor pressure of Ga vs temperature,” RCA Laboratories, Princeton, Tech. Rep., 1968.
- [60] D. Siche, K. Kachel, R. Zwierz, S. Golka, A. Vodopyanov, I. Izotov, P. Sennikov, S. Golubev, K.-P. Franke, P. Sudhoff, and D. Gogova, “Chlorine-free plasma-based vapour growth of GaN,” *Physica Status Solidi (C)*, vol. 9, no. 3-4, pp. 440–444, Mar. 2012. [Online]. Available: <http://doi.wiley.com/10.1002/pssc.201100322>
- [61] H. W. Choi, M. a. Rana, S. J. Chua, T. Osipowicz, and J. S. Pan, “Surface analysis of GaN decomposition,” *Semiconductor Science and Technology*, vol. 17, no. 12, pp. 1223–1225, Dec. 2002. [Online]. Available: <http://stacks.iop.org/0268-1242/17/i=12/a=304?key=crossref.6ef9c7c1fe079502a6e997956bd65220>
- [62] P. Dryburgh, “The Estimation of Minimum Growth Temperature for Crystals Grown from the Gas Phase,” *Journal of Crystal Growth*, vol. 87, no. 4, pp. 397–407, 1988. [Online]. Available: <http://www.sciencedirect.com/science/article/pii/0022024888900851>
- [63] T. Sherwood and R. O. Maak, “The reaction of ammonia with carbon at elevated temperatures,” *Ind. Eng. Chem. Fundamen.*, vol. 1, no. 2, pp. 111–115, 1962.
- [64] P. B. Shevlin, D. W. Mcpherson, and P. Melius, “Reaction of Atomic Carbon with Ammonia. The Mechanism of Formation of Amino Acid Precursors,” *J. Am. Chem. SOC.*, vol. 105, pp. 488–491, 1983. [Online]. Available: <http://pubs.acs.org/doi/pdf/10.1021/ja00341a031>
- [65] D. S. Golka, “Personal communication, November 21, 2013.”
- [66] S. A. Kukushkin, A. V. Osipov, V. N. Bessolov, B. K. Medvedev, V. K. Nevolin, and K. A. Tcarik, “Substrates for epitaxy of gallium nitride: New materials and techniques,” *Rev. Adv. Mater. Sci.*, vol. 17, pp. 1–32, 2008. [Online]. Available: [http://www.ipme.ru/e-journals/RAMS/no\\_11708/kukushkin.pdf](http://www.ipme.ru/e-journals/RAMS/no_11708/kukushkin.pdf)
- [67] T. Kozawa, T. Kachi, H. Kano, H. Nagase, N. Koide, and K. Manabe, “Thermal stress in GaN epitaxial layers grown on sapphire substrates,” *Journal of Applied Physics*, vol. 77, no. 9, p. 4389, 1995. [Online]. Available: <http://link.aip.org/link/JAPIAU/v77/i9/p4389/s1&Agg=doi>
- [68] K. Hiramatsu, H. Amano, I. Akasaki, H. Kato, N. Koide, and K. Manabe, “MOVPE growth of GaN on a misoriented sapphire substrate,” *Journal of Crystal Growth*, vol. 107, no. 1-4, pp. 509–512, Jan. 1991. [Online]. Available: <http://linkinghub.elsevier.com/retrieve/pii/0022024891905124>
- [69] P. Brückner, M. Feneberg, K. Thonke, F. Habel, and F. Scholz, “High quality GaN layers grown on slightly miscut sapphire wafers,” *MRS Proceedings*, vol. 892, pp. 0892–FF21–04, Feb. 2011. [Online]. Available: [http://journals.cambridge.org/abstract\\_S1946427400043414](http://journals.cambridge.org/abstract_S1946427400043414)

- [70] T. Yuasa, Y. Ueta, Y. Tsuda, A. Ogawa, M. Taneya, and K. Takao, "Effect of Slight Misorientation of Sapphire Substrate on Metalorganic Chemical Vapor Deposition Growth of GaN," *Japanese Journal of Applied Physics*, vol. 38, no. 7A, pp. 703–705, 1999. [Online]. Available: <http://jjap.jsap.jp/link?JJAP/38/L703/>
- [71] S. Gu, R. Zhang, Y. Shi, Y. Zheng, L. Zhang, F. Dwikusuma, and T. Kuech, "The impact of initial growth and substrate nitridation on thick GaN growth on sapphire by hydride vapor phase epitaxy," *Journal of Crystal Growth*, vol. 231, no. 3, pp. 342–351, 2001. [Online]. Available: <http://www.sciencedirect.com/science/article/pii/S0022024801014646>
- [72] S. Keller, B. P. Keller, Y.-F. Wu, B. Heying, D. Kapolnek, J. S. Speck, U. K. Mishra, and S. P. DenBaars, "Influence of sapphire nitridation on properties of gallium nitride grown by metalorganic chemical vapor deposition," *Applied Physics Letters*, vol. 68, no. 11, p. 1525, 1996. [Online]. Available: <http://link.aip.org/link/APPLAB/v68/i11/p1525/s1&Agg=doi>
- [73] F. Widmann, G. Feuillet, B. Daudin, and J. L. Rouvière, "Low temperature sapphire nitridation: A clue to optimize GaN layers grown by molecular beam epitaxy," *Journal of Applied Physics*, vol. 85, no. 3, p. 1550, 1999. [Online]. Available: <http://link.aip.org/link/JAPIAU/v85/i3/p1550/s1&Agg=doi>
- [74] J. Lee, H. Paek, J. Yoo, G. Kim, and D. Kum, "Low temperature buffer growth to improve hydride vapor phase epitaxy of GaN," *Materials Science and Engineering: B*, vol. 59, no. 1-3, pp. 12–15, May 1999. [Online]. Available: <http://linkinghub.elsevier.com/retrieve/pii/S0921510798004048>
- [75] K. Hoshino, N. Yanagita, M. Araki, and K. Tadatomo, "Effect of low-temperature GaN buffer layer on the crystalline quality of subsequent GaN layers grown by MOVPE," *Journal of Crystal Growth*, vol. 298, pp. 232–234, Jan. 2007. [Online]. Available: <http://linkinghub.elsevier.com/retrieve/pii/S0022024806009730>
- [76] K. Shimamura, E. G. Villora, K. Domen, K. Yui, K. Aoki, and N. Ichinose, "Epitaxial Growth of GaN on (100)  $\beta$ -Ga<sub>2</sub>O<sub>3</sub> Substrates by Metalorganic Vapor Phase Epitaxy," *Japanese Journal of Applied Physics*, vol. 44, no. 1, pp. L7–L8, Jan. 2005. [Online]. Available: <http://jjap.jsap.jp/link?JJAP/44/L7/>
- [77] S. Ohira, N. Suzuki, H. Minami, K. Takahashi, T. Araki, and Y. Nanishi, "Growth of hexagonal GaN films on the nitridated  $\beta$ -Ga<sub>2</sub>O<sub>3</sub> substrates using RF-MBE," *Physica Status Solidi (C)*, vol. 4, no. 7, pp. 2306–2309, Jun. 2007. [Online]. Available: <http://doi.wiley.com/10.1002/pssc.200674877>
- [78] K. Kachel, M. Korytov, D. Gogova, Z. Galazka, M. Albrecht, R. Zwierz, D. Siche, S. Golka, A. Kwasniewski, M. Schmidbauer, and R. Fornari, "A new approach to free-standing GaN using  $\beta$ -Ga<sub>2</sub>O<sub>3</sub> as a substrate," *CrystEngComm*, vol. 14, no. 24, p. 8536, 2012. [Online]. Available: <http://xlink.rsc.org/?DOI=c2ce25976a>
- [79] Kymatech, "Gallium Nitride templates. Kymatech." [Online]. Available: <http://kymatech.com/>

- [80] PAM-XIAMEN, “Gallium Nitride template. PAM-XIAMEN.” [Online]. Available: <http://www.gantemplate.com/p/blog-page.html>
- [81] R. lambda, “Gallium Nitride templates. RF lambda.” [Online]. Available: [http://www.rflambda.com/product\\_gan\\_template.jsp](http://www.rflambda.com/product_gan_template.jsp)
- [82] Saint-Gobain, “Gallium nitride templates. Saint-Gobain.” [Online]. Available: <http://www.photonic.saint-gobain.com/GaN-Standard-Templates.aspx>
- [83] L. I. Berger, *Semiconductor Materials*. CRC Press, 1996.
- [84] S. Strite and H. Morkoc, “GaN, AlN, and InN: A review,” *J. Vac. Sci. Technol. B*, vol. 10, no. 4, pp. 1237–1266, 1992.
- [85] HexaTech, “AlN Wafer Sales, Aluminum Nitride Substrates, HexaTech, Inc.” [Online]. Available: <http://www.hexatechinc.com/aln-wafer-sales.html>
- [86] H. J. Scheel, “Historical aspects of crystal growth technology,” *Journal of Crystal Growth*, vol. 211, no. 1-4, pp. 1–12, Apr. 2000. [Online]. Available: <http://linkinghub.elsevier.com/retrieve/pii/S0022024899007800>
- [87] J. I. Pankove, T. D. Moustakas, A. Trampert, O. Brandt, and K. Ploog, “Chapter 7 Crystal Structure of Group III Nitrides,” *Semiconductors and Semimetals*, vol. 50, pp. 167–192, 1997. [Online]. Available: <http://www.sciencedirect.com/science/article/pii/S0080878408630884>
- [88] M. Losurdo, G. Bruno, T. Kim, S. Choi, A. Brown, and A. Moto, “Nucleation and growth mode of the molecular beam epitaxy of GaN on 4H–SiC exploiting real time spectroscopic ellipsometry,” *Journal of Crystal Growth*, vol. 284, no. 1-2, pp. 156–165, Oct. 2005. [Online]. Available: <http://linkinghub.elsevier.com/retrieve/pii/S0022024805008274>
- [89] D. Simeonov, E. Feltn, J.-F. Carlin, R. Buttéé, M. Ilegems, and N. Grandjean, “Stranski-Krastanov GaN/AlN quantum dots grown by metal organic vapor phase epitaxy,” *Journal of Applied Physics*, vol. 99, no. 8, p. 083509, 2006. [Online]. Available: <http://link.aip.org/link/JAPIAU/v99/i8/p083509/s1&Agg=doi>
- [90] J. Brault, S. Tanaka, E. Sarigiannidou, J.-L. Rouvière, B. Daudin, G. Feuillet, and H. Nakagawa, “Linear alignment of GaN quantum dots on AlN grown on vicinal SiC substrates,” *Journal of Applied Physics*, vol. 93, no. 5, p. 3108, 2003. [Online]. Available: <http://link.aip.org/link/JAPIAU/v93/i5/p3108/s1&Agg=doi>
- [91] F. Widmann, B. Daudin, G. Feuillet, Y. Samson, J. L. Rouvière, and N. Pelekanos, “Growth kinetics and optical properties of self-organized GaN quantum dots,” *Journal of Applied Physics*, vol. 83, no. 12, p. 7618, 1998. [Online]. Available: <http://link.aip.org/link/JAPIAU/v83/i12/p7618/s1&Agg=doi>
- [92] F. Scholz, P. Brückner, F. Habel, M. Peter, and K. Köhler, “Improved GaN layer morphology by hydride vapor phase epitaxy on misoriented Al<sub>2</sub>O<sub>3</sub> wafers,” *Applied Physics Letters*, vol. 87, no. 18, p. 181902, Oct. 2005. [Online]. Available: <http://scitation.aip.org/content/aip/journal/apl/87/18/10.1063/1.2120916>



- [93] J. Suda, K. Miura, M. Honaga, Y. Nishi, N. Onojima, and H. Matsunami, "Effects of 6H-SiC surface reconstruction on lattice relaxation of AlN buffer layers in molecular-beam epitaxial growth of GaN," *Applied Physics Letters*, vol. 81, no. 27, p. 5141, 2002. [Online]. Available: <http://link.aip.org/link/APPLAB/v81/i27/p5141/s1&Agg=doi>
- [94] R. F. Davis, S. M. Bishop, S. Mita, R. Collazo, Z. J. Reitmeier, and Z. Sitar, "Epitaxial Growth Of Gallium Nitride," *AIP Conference Proceedings*, vol. 916, pp. 520–540, 2007. [Online]. Available: <http://link.aip.org/link/APCPCS/v916/i1/p520/s1&Agg=doi>
- [95] M. Lada, "Effect of anneal temperature on GaN nucleation layer transformation," *Journal of Crystal Growth*, vol. 258, no. 1-2, pp. 89–99, Oct. 2003. [Online]. Available: <http://linkinghub.elsevier.com/retrieve/pii/S0022024803015173>
- [96] W. Crookes, "The bakerian lecture: On the illumination of lines of molecular pressure, and the trajectory of molecules," *Phil. Trans. R. Soc. London Pt I*, p. 135, 1879.
- [97] N. A. Krall and A. W. Trivelpiece, *Principles of plasma physics*. McGraw-Hill, 1973.
- [98] J. R. Roth, *Industrial Plasma Engineering: Volume 1: Principles*. Bristol: Institute of Physics Publishing, 2003.
- [99] H. Conrads and M. Schmidt, "Plasma generation and plasma sources," *Plasma Sources Science and Technology*, vol. 9, pp. 441–454, 2000. [Online]. Available: <http://iopscience.iop.org/0963-0252/9/4/301>
- [100] D. Korzec, F. Werner, R. Winter, and J. Engemann, "Scaling of microwave slot antenna (SLAN): a concept for efficient plasma generation," *Plasma Sources Science and Technology*, vol. 5, no. 2, pp. 216–234, May 1996. [Online]. Available: <http://iopscience.iop.org/0963-0252/5/2/015>
- [101] R. J. Meredith, *Engineers' Handbook of Industrial Microwave Heating*. The Institution of Engineering and Technology, 1998.
- [102] G. V. Vajenine, "Use of plasma-activated gases in synthesis of solid-state nitrides," *Dalton transactions (Cambridge, England : 2003)*, vol. 39, pp. 6013–6017, Jul. 2010. [Online]. Available: <http://pubs.rsc.org/en/Content/ArticleLanding/2010/DT/c000361a#!divAbstract>
- [103] A. Bogaerts, E. Neyts, R. Gijbels, and J. van der Mullen, "Gas discharge plasmas and their applications," *Spectrochimica Acta Part B: Atomic Spectroscopy*, vol. 57, no. 4, pp. 609–658, Apr. 2002. [Online]. Available: <http://linkinghub.elsevier.com/retrieve/pii/S0584854701004062>
- [104] B. Eliasson and U. Kogelschatz, "Nonequilibrium Volume Plasma Chemical Processing," *IEEE Transactions on Plasma Science*, vol. 19, no. 6, pp. 1063–1077, 1991. [Online]. Available: [http://ieeexplore.ieee.org/xpl/login.jsp?tp=&arnumber=125031&url=http%3A%2F%2Fieeexplore.ieee.org%2Fxppls%2Fabs\\_all.jsp%3Farnumber%3D125031](http://ieeexplore.ieee.org/xpl/login.jsp?tp=&arnumber=125031&url=http%3A%2F%2Fieeexplore.ieee.org%2Fxppls%2Fabs_all.jsp%3Farnumber%3D125031)
- [105] C. Tendero, C. Tixier, P. Tristant, J. Desmaison, and P. Leprince, "Atmospheric pressure plasmas: A review," *Spectrochimica Acta Part B: Atomic Spectroscopy*, vol. 61, no. 1, pp. 2–30, Jan. 2006. [Online]. Available: <http://linkinghub.elsevier.com/retrieve/pii/S0584854705002843>

- [106] D. H. Goebel and I. Katz, “Basic Plasma Physics,” in *Fundamentals of Electric Propulsion: Ion and Hall Thrusters*, jpl space ed., J. H. Yuen, Ed. California Institute of Technology, 2008, p. 493. [Online]. Available: [http://descanso.jpl.nasa.gov/SciTechBook/SciTechBook.cfm?force\\_external=0](http://descanso.jpl.nasa.gov/SciTechBook/SciTechBook.cfm?force_external=0)
- [107] H. Carrere, A. Arnoult, A. Ricard, X. Marie, T. Amand, and E. Bedel-Pereira, “Nitrogen-plasma study for plasma-assisted MBE growth of 1.3  $\mu\text{m}$  laser diodes,” *Solid-State Electronics*, vol. 47, no. 3, pp. 419–423, 2003. [Online]. Available: <http://www.sciencedirect.com/science/article/pii/S0038110102003829>
- [108] E. Iliopoulos, A. Adikimenakis, E. Dimakis, K. Tsagaraki, G. Konstantinidis, and A. Georgakilas, “Active nitrogen species dependence on radiofrequency plasma source operating parameters and their role in GaN growth,” *Journal of Crystal Growth*, vol. 278, no. 1-4, pp. 426–430, May 2005. [Online]. Available: <http://linkinghub.elsevier.com/retrieve/pii/S0022024805000151>
- [109] S. Agarwal, B. Hoex, M. C. M. van de Sanden, D. Maroudas, and E. S. Aydil, “Absolute densities of N and excited N<sub>2</sub> in a N<sub>2</sub> plasma,” *Applied Physics Letters*, vol. 83, no. 24, pp. 4918–4920, 2003. [Online]. Available: <http://link.aip.org/link/APPLAB/v83/i24/p4918/s1&Agg=doi>
- [110] W. C. Hughes, W. H. Rowland Jr., M. A. L. Johnson, S. Fujita, J. W. Cook Jr., and J. F. Schetzina, “Molecular beam epitaxy growth and properties of GaN films on GaN/SiC substrates,” *J. Vac. Sci. Technol. B*, vol. 13, no. 4, pp. 1571–1577, 1995. [Online]. Available: [http://csma31.csm.jmu.edu/physics/hughes/JVST\\_B13\\_1571.pdf](http://csma31.csm.jmu.edu/physics/hughes/JVST_B13_1571.pdf)
- [111] A. N. Wright and C. A. Winkler, *Active Nitrogen*. New York: Academic Press, 1968.
- [112] N. Newman, “The energetics of the GaN MBE reaction: a case study of meta-stable growth,” *Journal of Crystal Growth*, vol. 178, pp. 102–112, 1997. [Online]. Available: <http://www.sciencedirect.com/science/article/pii/S0022024897000833>
- [113] B. V. Lvov, “Kinetics and mechanism of thermal decomposition of GaN,” *Thermochimica Acta*, vol. 360, no. 1, pp. 85–91, 2000. [Online]. Available: <http://www.sciencedirect.com/science/article/pii/S004060310000558X>
- [114] H. J. Kunze, *Introduction to Plasma Spectroscopy*. Berlin, Heidelberg: Springer, 2009.
- [115] U. Fantz, “Basics of plasma spectroscopy,” *Plasma Sources Science and Technology*, vol. 15, no. 4, pp. S137–S147, Nov. 2006. [Online]. Available: <http://stacks.iop.org/0963-0252/15/i=4/a=S01?key=crossref.55c2687ff5694740c0db81c4b07cacd0>
- [116] NIST, “Strong lines of Gallium (Ga).” [Online]. Available: <http://physics.nist.gov/PhysRefData/Handbook/Tables/galliumtable2.htm>
- [117] G. Herzberg, *Molecular Spectra and Molecular Structure: Spectra of Diatomic Molecules*. Krieger Pub Co, 1989.
- [118] R. W. B. Pearse and A. G. Gaydon, *The Identification of Molecular Spectra*, 4th ed. London: Chapman and Hall, 1976.

- [119] M. Keidar and I. I. Beilis, *Plasma Engineering Plasma Engineering Applications from Aerospace to Bio- and Nanotechnology*. Academic Press, 2013. [Online]. Available: <http://www.sciencedirect.com/science/article/pii/B9780123859778000081>
- [120] H. R. Griem, *Principles of Plasma Spectroscopy*. Cambridge University Press, 2005.
- [121] L. T. Ueno, O. Roberto-Neto, S. Canuto, and F. B. Machado, “The low-lying electronic states of the GaN molecule,” *Chemical Physics Letters*, vol. 413, no. 1-3, pp. 65–70, Sep. 2005. [Online]. Available: <http://linkinghub.elsevier.com/retrieve/pii/S0009261405006858>
- [122] Dr. Yang Xian, “Introduction to Molecular QM,” in *Quantum Mechanics of Atoms and Molecules. Lectures available online.*, 2008, ch. 4 Introduc. [Online]. Available: [http://theory.physics.manchester.ac.uk/~sim\\$Xian/qm/chapter4.pdf](http://theory.physics.manchester.ac.uk/~sim$Xian/qm/chapter4.pdf)
- [123] Georgia State University, “Hyperphysics web page.” [Online]. Available: <http://hyperphysics.phy-astr.gsu.edu/hbase/hframe.html>
- [124] “Hyperphysics web page. Rotational spectra.” [Online]. Available: <http://hyperphysics.phy-astr.gsu.edu/hbase/molecule/rotrig.html>
- [125] Dr. Stuart R. Mackenzie, “Molecular Electronic Spectroscopy. Lectures available online.” [Online]. Available: <http://mackenzie.chem.ox.ac.uk/teaching/MolecularElectronicSpectroscopy.pdf>
- [126] O. Dutuit, N. Carrasco, R. Thissen, V. Vuitton, C. Alcaraz, P. Pernot, N. Balucani, P. Casavecchia, A. Canosa, S. Le Picard, J.-C. Loison, Z. Herman, J. Zabka, D. Ascenzi, P. Tosi, P. Franceschi, S. D. Price, and P. Lavvas, “Critical Review of N, N+, N+ 2, N++, and N++ 2 Main Production Processes and Reactions of Relevance to Titan’s Atmosphere,” *The Astrophysical Journal Supplement Series*, vol. 204, no. 2, 2013. [Online]. Available: <http://iopscience.iop.org/0067-0049/204/2/20/article>
- [127] A. Cho, *MRS Bulletin, Mater. Res. Soc.*, p. 21, 1995.
- [128] J. Tsao, *Materials Fundamentals of Molecular Beam Epitaxy*. New York: Academic Press, 1993.
- [129] M. J. Manfra, K. W. Baldwin, a. M. Sergent, K. W. West, R. J. Molnar, and J. Caissie, “Electron mobility exceeding 160 000 cm<sup>2</sup> V s in AlGa<sub>0.15</sub>N GaN heterostructures grown by molecular-beam epitaxy,” *Applied Physics Letters*, vol. 85, no. 22, p. 5394, 2004. [Online]. Available: <http://link.aip.org/link/APPLAB/v85/i22/p5394/s1&Agg=doi>
- [130] M. J. Manfra, N. G. Weimann, J. W. P. Hsu, L. N. Pfeiffer, K. W. West, and S. N. G. Chu, “Dislocation and morphology control during molecular-beam epitaxy of AlGa<sub>0.15</sub>N/GaN heterostructures directly on sapphire substrates,” *Applied Physics Letters*, vol. 81, no. 8, p. 1456, 2002. [Online]. Available: <http://link.aip.org/link/APPLAB/v81/i8/p1456/s1&Agg=doi>
- [131] C. Skierbiszewski, Z. Wasilewski, I. Grzegory, and S. Porowski, “Nitride-based laser diodes by plasma-assisted MBE. From violet to green emission,” *Journal of Crystal Growth*, vol. 311, no. 7, pp. 1632–1639, Mar. 2009. [Online]. Available: <http://linkinghub.elsevier.com/retrieve/pii/S0022024808014085>

- [132] C. Skierbiszewski, M. Siekacz, H. Turski, G. Muzioł, M. Sawicka, A. Feduniewicz-Zmuda, J. Smalc-Koziorowska, P. Perlin, S. Grzanka, Z. R. Wasilewski, R. Kucharski, and S. Porowski, “InGaN laser diodes operating at 450–460 nm grown by rf-plasma MBE,” *Journal of Vacuum Science & Technology B: Microelectronics and Nanometer Structures*, vol. 30, no. 2, p. 02B102, Dec. 2012. [Online]. Available: <http://scitation.aip.org/content/avs/journal/jvstb/30/2/10.1116/1.3665223>
- [133] T. D. Moustakas, T. Lei, and R. J. Molnar, “Growth of GaN by ECR-assisted MBE,” *Physica B: Condensed Matter*, vol. 185, no. 1-4, pp. 36–49, 1993. [Online]. Available: <http://www.sciencedirect.com/science/article/pii/092145269390213P>
- [134] H. Amano, N. Sawaki, I. Akasaki, and Y. Toyoda, “Metalorganic vapor phase epitaxial growth of a high quality GaN film using an AlN buffer layer,” *Applied Physics Letters*, vol. 48, no. 5, p. 353, 1986. [Online]. Available: <http://link.aip.org/link/APPLAB/v48/i5/p353/s1&Agg=doi>
- [135] S. Nakamura, T. Mukai, and M. Senoh, “High-Power GaN P-N Junction Blue-Light-Emitting Diodes,” *Japanese Journal of Applied Physics*, vol. 30, no. 12A, pp. 1998–2001, 1991. [Online]. Available: <http://jjap.jsap.jp/link?JJAP/30/L1998/>
- [136] M. Rudziński, R. Kudrawiec, L. Janicki, J. Serafinczuk, R. Kucharski, M. Zając, J. Misiewicz, R. Doradziński, R. Dwiliński, and W. Strupiński, “Growth of GaN epilayers on c-, m-, a-, and (20.1)-plane GaN bulk substrates obtained by ammonothermal method,” *Journal of Crystal Growth*, vol. 328, no. 1, pp. 5–12, Aug. 2011. [Online]. Available: <http://linkinghub.elsevier.com/retrieve/pii/S0022024811005379>
- [137] Z. Hassan, Y. Lee, F. Yam, K. Ibrahim, M. Kordesch, W. Halverson, and P. Colter, “Characteristics of low-temperature-grown GaN films on Si(111),” *Solid State Communications*, vol. 133, no. 5, pp. 283–287, Feb. 2005. [Online]. Available: <http://linkinghub.elsevier.com/retrieve/pii/S0038109804009706>
- [138] Y. Lee, Z. Hassan, F. Yam, M. Abdullah, K. Ibrahim, M. Barmawi, M. Budiman, and P. Arifin, “A comparative study of the electrical characteristics of metal-semiconductor-metal (MSM) photodiodes based on GaN grown on silicon,” *Applied Surface Science*, vol. 249, no. 1-4, pp. 91–96, Aug. 2005. [Online]. Available: <http://linkinghub.elsevier.com/retrieve/pii/S0169433204016423>
- [139] N. Ihashi, K. Itoh, and O. Matsumoto, “Deposition of Gallium Nitride Thin Films by MOCVD in Microwave Plasma,” *Plasma Chemistry and Plasma Processing*, vol. 17, no. 4, pp. 453–465, 1997. [Online]. Available: <http://link.springer.com/article/10.1023%2FA%3A1021851214864>
- [140] S. W. Choi, K. J. Bachmann, and G. Lucovsky, “Growth kinetics and characterizations of gallium nitride thin films by remote PECVD,” *J. Mater. Res.*, vol. 8, no. 4, pp. 847–854, 1993.
- [141] T. Nagata, Y. Sakuma, T. Uehara, and T. Chikyow, “GaN Film Fabrication by Near-Atmospheric Plasma-Assisted Chemical Vapor Deposition,” *Japanese Journal of Applied Physics*, vol. 46, no. No. 2, pp. L43–L45, Jan. 2007. [Online]. Available: <http://jjap.ipap.jp/link?JJAP/46/L43/>

- 
- [142] T. Ozawa, M. Dohi, T. Matsuura, and Y. Hayakawa, "Synthesis of GaN bulk crystals and melt growth of GaN layers under nitrogen plasma," *Journal of Crystal Growth*, vol. 310, no. 7-9, pp. 1785–1789, Apr. 2008. [Online]. Available: <http://linkinghub.elsevier.com/retrieve/pii/S0022024807010548>
- [143] K. D. Sattler, Ed., *Handbook of Nanophysics: Nanotubes and Nanowires*. CRC Press, 2010. [Online]. Available: <http://www.taylorandfrancis.com/books/details/9781420075427/>
- [144] S. Porowski and I. Grzegory, "Thermodynamical properties of III-V nitrides and crystal growth of GaN at high N<sub>2</sub> pressure," *Journal of Crystal Growth*, vol. 178, pp. 174–188, 1997. [Online]. Available: <http://www.sciencedirect.com/science/article/pii/S0022024897000729>
- [145] D. Liedtke, *Wärmebehandlung von Eisenwerkstoffen II*. Expert-Verlag GmbH, 2010.
- [146] U. Kogelschatz, B. Eliasson, and W. Egli, "From ozone generators to flat television screens: history and future potential of dielectric-barrier discharges," *Pure and Applied Chemistry*, vol. 71, no. 10, pp. 1819–1828, 1999. [Online]. Available: <http://iupac.org/publications/pac/71/10/1819/>
- [147] W. Siemens, "Ueber die elektrostatische induction und die verzögerung des stroms in flaschendrähnten," *Poggendorffs Ann. Phys. Chem.*, vol. 102, no. 66, 1857.
- [148] U. Kogelschatz, "Dielectric-barrier Discharges: Their History, Discharge Physics, and Industrial Applications," *Plasma Chemistry and Plasma Processing*, vol. 23, no. 1, pp. 1–46, 2003.
- [149] Systec, "Betriebsanleitung, Kristallzüchtungsanlage GaN," pp. Dok-ID Syst-6446-DE, 2008.
- [150] H.-J. Rost, D. Siche, J. Dolle, W. Eiserbeck, T. Mueller, D. Schulz, G. Wagner, and J. Wollweber, "Influence of different growth parameters and related conditions on 6H-SiC crystals grown by the modified Lely method," *Materials Science and Engineering: B*, vol. 61-62, pp. 68–72, 1999.
- [151] H.-J. Rost, M. Schmidbauer, D. Siche, and R. Fornari, "Polarity- and orientation-related defect distribution in 4H-SiC single crystals," *Journal of Crystal Growth*, vol. 290, no. 1, pp. 137–143, Apr. 2006. [Online]. Available: <http://linkinghub.elsevier.com/retrieve/pii/S0022024805016453>
- [152] Mersen, "Materials parameters of graphite felt insulation. CBCF 15 - 2000."
- [153] RATH, "Altraform, RATH. Datasheet." [Online]. Available: <http://www.rath-group.com/en/products/vaccum-formed-shapes/altraform/>
- [154] HC-STARCK, "SSN Si<sub>3</sub>N<sub>4</sub>, HC-STARCK, datasheet."
- [155] HP, "8753C Network Analyzer Reference, HP, 1989."
- [156] Agilent, "Network Analyzer Basics. Agilent." [Online]. Available: <http://cp.literature.agilent.com/litweb/pdf/5965-7917E.pdf>

- [157] IBF Electronic, “PGEN2450/3-4KW2AIW, IBF Electronic, User manual, rev. 0.2, 09-08-2010.”
- [158] S-TEAM, “Homer Hot Measurement and Tuning System, S-TEAM Lab, User’s Handbook.” [Online]. Available: <http://www.s-team.sk/download/HomerHbook5001.pdf>
- [159] Plansee, “Material properties of molybdenum. Plansee catalogue.” [Online]. Available: [http://www.plansee.com/en/Materials-Molybdenum-402.htm#Eigenschaften\\_Molybdaen](http://www.plansee.com/en/Materials-Molybdenum-402.htm#Eigenschaften_Molybdaen)
- [160] Y. P. Raizer, *Gas Discharge Physics*. Springer, 1991.
- [161] Lumasenseinc, “Pyrometer IS 5, IGA 5. Datasheet.” [Online]. Available: [http://www.lumasenseinc.com/uploads/Products/Impac/pdf/Datenblaetter/Pyrometer/Serie\\_5/IS5\\_IGA5\\_Datenblatt.pdf](http://www.lumasenseinc.com/uploads/Products/Impac/pdf/Datenblaetter/Pyrometer/Serie_5/IS5_IGA5_Datenblatt.pdf)
- [162] Plansee, “Material properties of tungsten. Plansee catalogue.” [Online]. Available: [http://www.plansee.com/en/Materials-Tungsten-403.htm#Eigenschaften\\_Wolfram](http://www.plansee.com/en/Materials-Tungsten-403.htm#Eigenschaften_Wolfram)
- [163] TGI, “Borosilicate glass I-420.” [Online]. Available: <http://www.tgi-glas.com/data-sheets.html>
- [164] K. Koski, J. Hoelsae, and P. Juliet, “Surface defects and arc generation in reactive magnetron sputtering of aluminium oxide thin films,” *Surface and Coatings Technology*, vol. 115, pp. 163–171, 1999. [Online]. Available: <http://www.sciencedirect.com/science/article/pii/S0257897299001723>
- [165] M. Laux, W. Schneider, P. Wienhold, B. Jüttner, A. Huber, M. Balden, J. Linke, M. Rubel, D. Hildebrandt, M. Mayer, A. Pospieszczyk, H. Kostial, S. Jachmich, A. Herrmann, B. Schweer, H. Bolt, and B. Jüttner, “Arcing at B4C-covered limiters exposed to a SOL-plasma,” *Journal of Nuclear Materials*, vol. 313-316, pp. 62–66, 2003. [Online]. Available: <http://www.sciencedirect.com/science/article/pii/S0022311502013338>
- [166] D. Siche, “Abschlussbericht zum Verbundprojekt Grundlagenuntersuchungen zur Sublimationszüchtung von GaN-Halbleitkristallen,” Leibniz Institute for Crystal Growth, Berlin, Tech. Rep., 2009.
- [167] H. Shin, E. Arkun, D. Thomson, P. Miraglia, E. Preble, R. Schlessner, S. Wolter, Z. Sitar, and R. Davis, “Growth and decomposition of bulk GaN: role of the ammonia/nitrogen ratio,” *Journal of Crystal Growth*, vol. 236, no. 4, pp. 529–537, Mar. 2002. [Online]. Available: <http://linkinghub.elsevier.com/retrieve/pii/S0022024802008254>
- [168] P. Harteck, “Measurements of the vapor pressure of silver, gold, copper, lead, gallium, tin and calculation of the chemical constants,” *Zeitschrift für Physikalische Chemie*, vol. 134, pp. 1–20, 1928.
- [169] R. Speiser and H. L. Johnston, *J. Am. Chem. Soc.*, vol. 75, p. 1469, 1953.
- [170] C. N. Cochran and L. M. Foster, *J. Electrochem. Soc.*, vol. 109, no. 144, 1962.

- [171] S. Antkiw and V. H. Dibeler, "Mass spectrum of gallium vapor," *J. Chem. Phys.*, vol. 21, p. 1890, 1953.
- [172] D. Siche, D. Gogova, S. Lehmann, T. Fizia, R. Fornari, M. Andrasch, A. V. Pipa, and J. Ehlbeck, "PVT growth of GaN bulk crystals," *Journal of Crystal Growth*, vol. 318, no. 1, pp. 406–410, Mar. 2011. [Online]. Available: <http://linkinghub.elsevier.com/retrieve/pii/S0022024810007608>
- [173] N. Greenwood and A. Earnshaw, *Chemistry of the Elements*. Weinheim: VCH Wiley, 1990.
- [174] T. A. Fizia, "Study of the gallium evaporation in the GaN growth system," Master's Thesis, Brandenburg Technical University Cottbus, 2010.
- [175] I. V. Markov, *Crystal Growth for Beginners Fundamentals of Nucleation, Crystal Growth and Epitaxy*. World Scientific, 1995.
- [176] R. Fornari and C. Paorici, Eds., *Theoretical and Technological Aspects of Crystal Growth*. Rimini: Trans Tech Publications LTD, 1998.
- [177] P. G. Baranov, E. N. Mokhov, A. O. Ostroumov, M. G. Ramm, M. S. Ramm, V. V. Ratnikov, A. D. Roenkov, Y. A. Vodakov, A. A. Wolfson, G. V. Saporin, S. Y. Karpov, D. V. Zimina, Y. N. Makarov, and H. Juergensen, "Current status of GaN crystal growth by sublimation sandwich technique," *MRS Internet J. Nitride Semicond. Res.* 3, vol. 50, pp. 1–17, 1998.
- [178] S. C. Hardy, "The surface tension of liquid gallium," *Journal of Crystal Growth*, vol. 71, no. 3, pp. 602–606, 1985. [Online]. Available: <http://www.sciencedirect.com/science/article/pii/0022024885903677>
- [179] M. J. Assael, I. J. Armyra, S. V. Stankus, J. Wu, and W. A. Wakeham, "Reference Data for the Density and Viscosity of Liquid Cadmium, Cobalt, Gallium, Indium, Mercury, Silicon, Thallium, and Zinc," *J. Phys. Chem. Ref. Data*, vol. 41, no. 3, p. 33101, 2012.
- [180] C. M. Ferreira and M. Moisan, *Microwave Discharges: Fundamentals and Applications (Nato Science Series B: (closed))*. Springer, 1993.
- [181] M. Moisan and J. Pelletier, Eds., *Microwave Excited Plasmas, Volume 4 (Plasma Technology)*. Elsevier Science, 1992.
- [182] E. Tatarova and V. Guerra, "Nitrogen dissociation in low-pressure microwave plasmas," *Journal of Physics: Conference Series*, vol. 71, no. 012010, 2007. [Online]. Available: <http://iopscience.iop.org/1742-6596/71/1/012010>
- [183] J. Hubert, M. Moisan, and A. Ricard, "A new microwave plasma at atmospheric pressure," *Spectrochimica Acta Part B*, vol. 34, no. 1, pp. 1–10, 1979. [Online]. Available: <http://www.sciencedirect.com/science/article/pii/0584854779800166>
- [184] C. Beenakker, "A cavity for microwave induced plasmas operated in Helium and argon at atmospheric pressure," *Spectrochim. Acta Part B*, vol. 31, pp. 483–486, 1976. [Online]. Available: <http://www.sciencedirect.com/science/article/pii/058485477680047X>

- [185] L. Bardos, H. Barankova, T. Welzel, I. Dani, S. Peter, and F. Richter, "Comparison of the radio frequency hollow cathode to the microwave antenna discharge for plasma processing," *Journal of Applied Physics*, vol. 90, no. 4, p. 1703, 2001. [Online]. Available: <http://link.aip.org/link/JAPIAU/v90/i4/p1703/s1&Agg=doi>
- [186] M. Moisan and M. Wertheimer, "Comparison of microwave and r.f. plasmas: fundamentals and applications," *Surface and Coatings Technology*, vol. 59, no. 1-3, pp. 1–13, Oct. 1993. [Online]. Available: <http://linkinghub.elsevier.com/retrieve/pii/025789729390047R>
- [187] C. Corr, R. Boswell, and R. Carman, "Gas phase optical emission spectroscopy during remote plasma chemical vapour deposition of GaN and relation to the growth dynamics," *Journal of Physics D: Applied Physics*, vol. 44, no. 4, p. 045201, Feb. 2011. [Online]. Available: <http://stacks.iop.org/0022-3727/44/i=4/a=045201?key=crossref.0030418d7c5e4420952a409e12983727>
- [188] R. M. Twyman, *Atomic Emission Spectroscopy*. York: University of York, 2005.
- [189] Dr. J. Ehlbeck, "Personal communication, February 21, 2013."
- [190] A. Lofthus and P. H. Krupenie, "The spectrum of molecular nitrogen," *Journal of Physical and Chemical Reference Data*, vol. 6, no. 1, p. 113, 1977. [Online]. Available: <http://link.aip.org/link/JPCRBU/v6/i1/p113/s1&Agg=doi>
- [191] Z. Rappoport, Ed., *The chemistry of the cyano group*. Jerusalem: Wiley & Sons, 1970.
- [192] G. Provencher and D. Mckenney, "CN emission in active nitrogen," *Chemical Physics Letters*, vol. 10, no. 4, pp. 3–6, 1971. [Online]. Available: <http://www.sciencedirect.com/science/article/pii/000926147180310X>
- [193] G. Hatem, C. Colon, and J. Campos, "Study of CN emission from a laser induced plasma of graphite in air," *Spectrochimica Acta*, vol. 49A, no. 4, pp. 509–516, 1993. [Online]. Available: <http://www.sciencedirect.com/science/article/pii/058485399380193E>
- [194] T. Shirai, J. Reader, a. E. Kramida, and J. Sugar, "Spectral Data for Gallium: Ga I through Ga XXXI," *Journal of Physical and Chemical Reference Data*, vol. 36, no. 2, p. 509, 2007. [Online]. Available: <http://link.aip.org/link/JPCRBU/v36/i2/p509/s1&Agg=doi>
- [195] D. C. Frost and C. A. McDowell, "The Dissociation Energy of the Nitrogen Molecule," *Proceedings of the Royal Society A: Mathematical, Physical and Engineering Sciences*, vol. 236, no. 1205, pp. 278–284, Aug. 1956. [Online]. Available: <http://rspa.royalsocietypublishing.org/cgi/doi/10.1098/rspa.1956.0135>
- [196] A. Ellahi and S. Ahmad, "Formation of CN in N<sub>2</sub> + He discharges in graphite hollow cathodes," *Journal of Physics D: Applied Physics*, vol. 38, no. 10, pp. 1565–1570, May 2005. [Online]. Available: <http://stacks.iop.org/0022-3727/38/i=10/a=011?key=crossref.aee3fc5452e80765fde5817e8c39af6d>
- [197] Dr. A. V. Pipa, "Personal communication, November 21, 2012."



- [198] PR Hoffman, "Sapphire processing." [Online]. Available: <http://www.prhoffman.com/sapphire-processing.html>
- [199] A. Abid, R. Bensalem, and B. Sealy, "The thermal stability of AlN," *Journal of Materials Science*, vol. 21, pp. 1301–1304, 1986. [Online]. Available: <http://link.springer.com/article/10.1007%2F00553267>
- [200] Plansee, "Material properties of tantalum. Plansee catalogue." [Online]. Available: [http://www.plansee.com/en/Materials-Tantalum-404.htm#Eigenschaften\\_Tantal](http://www.plansee.com/en/Materials-Tantalum-404.htm#Eigenschaften_Tantal)
- [201] H. Wang, Y. Amijima, Y. Ishihama, and S. Sakai, "Influence of carrier gas on the morphology and structure of GaN layers grown on sapphire substrate by six-wafer metal organic chemical vapor deposition system," *Journal of Crystal Growth*, vol. 233, no. 4, pp. 681–686, 2001. [Online]. Available: <http://www.sciencedirect.com/science/article/pii/S0022024801016311>
- [202] G. Lukin, C. Röder, E. Niederschlag, Y. Shashev, U. Mühle, O. Pätzold, J. Kortus, D. Rafaja, and M. Stelter, "Nucleation of GaN on sapphire substrates at intermediate temperatures by Hydride Vapor Phase Epitaxy," *Crystal Research and Technology*, vol. 47, no. 2, pp. 121–130, Feb. 2012. [Online]. Available: <http://doi.wiley.com/10.1002/crat.201100461>
- [203] M. Hermann, D. Gogova, D. Siche, M. Schmidbauer, B. Monemar, M. Stutzmann, and M. Eickhoff, "Nearly stress-free substrates for GaN homoepitaxy," *Journal of Crystal Growth*, vol. 293, no. 2, pp. 462–468, 2006. [Online]. Available: <http://www.sciencedirect.com/science/article/pii/S0022024806005252>
- [204] Y. Mochizuki and K. Tanaka, "Theoretical spectroscopic constants of the GaN molecule," *Theoretical Chemistry Accounts*, vol. 101, no. 4, pp. 292–296, 1999. [Online]. Available: <http://link.springer.com/article/10.1007%2Fs002140050443>
- [205] P. A. Denis and K. Balasubramanian, "Spectroscopic constants and potential energy curves of gallium nitride (GaN) and ions: GaN<sup>+</sup> and GaN<sup>−</sup>," *Chemical Physics Letters*, vol. 423, no. 1-3, pp. 247–253, May 2006. [Online]. Available: <http://linkinghub.elsevier.com/retrieve/pii/S0009261406004349>
- [206] A. Hirako, K. Kusakabe, and K. Ohkawa, "Modeling of Reaction Pathways of GaN Growth by Metalorganic Vapor-Phase Epitaxy Using TMGa/NH<sub>3</sub>/H<sub>2</sub> System: A Computational Fluid Dynamics Simulation Study," *Japanese Journal of Applied Physics*, vol. 44, no. 2, pp. 874–879, Feb. 2005. [Online]. Available: <http://jjap.jsap.jp/link?JJAP/44/874/>
- [207] SpectralFit S.A.S., "Specair." [Online]. Available: <http://www.specair-radiation.net/>
- [208] R. Zwierz, S. Golka, K. Kachel, D. Siche, R. Fornari, P. Sennikov, A. Vodopyanov, and A. V. Pipa, "Plasma enhanced growth of GaN single crystalline layers from Ga vapour," *Crystal Research and Technology*, vol. 48, no. 4, pp. 186–192, Apr. 2013. [Online]. Available: <http://doi.wiley.com/10.1002/crat.201200481>
- [209] NIST, "Strong Lines of Magnesium ( Mg )." [Online]. Available: <http://physics.nist.gov/PhysRefData/Handbook/Tables/magnesiumtable2.htm>

- [210] D. Cai, L. Zheng, H. Zhang, D. Zhuang, Z. Herro, R. Schlessler, and Z. Sitar, “Effect of thermal environment evolution on AlN bulk sublimation crystal growth,” *Journal of Crystal Growth*, vol. 306, no. 1, pp. 39–46, Aug. 2007. [Online]. Available: <http://linkinghub.elsevier.com/retrieve/pii/S0022024807004186>
- [211] S. Veprek, “Chemical evaporation and deposition of solids in a non-isothermal plasma; chemical transport of carbon,” *Journal of Crystal Growth*, vol. 17, pp. 101–116, 1972. [Online]. Available: <http://www.sciencedirect.com/science/article/pii/0022024872902369>
- [212] Y. Mori, M. Imade, M. Maruyama, and M. Yoshimura, “Growth of GaN Crystals by Na Flux Method,” *ECS Journal of Solid State Science and Technology*, vol. 2, no. 8, pp. N3068–N3071, Jul. 2013. [Online]. Available: <http://jss.ecsdl.org/cgi/doi/10.1149/2.015308jss>
- [213] J. F. Shackelford and W. Alexander, *CRC Practical Handbook of Materials Selection*. CRC Press, 1995.
- [214] E. S. Lukin, “Modern high-density oxide-based ceramics with a controlled microstructure. Part V. Chemical-resistant high-density yttrium-, scandium-, and alumina-based ceramics,” *Refractories and Industrial Ceramics*, vol. 38, no. 2, pp. 47–51, Feb. 1997. [Online]. Available: <http://link.springer.com/10.1007/BF02767832>
- [215] Plansee, “Material properties of niobium. Plansee catalogue.” [Online]. Available: [http://www.plansee.com/en/Materials-Niobium-405.htm#Niob\\_Eigenschaften](http://www.plansee.com/en/Materials-Niobium-405.htm#Niob_Eigenschaften)
- [216] SPECS, “Useful Information and Facts about the Practice of Sputtering.” [Online]. Available: <http://www.specs.de/cms/upload/PDFs/IQE11-35/sputter-info.pdf>

# List of Figures

1.1. Band gap energy in the function of lattice constant. III-nitrides at RT [8]	2
1.2. Ideal wurtzite GaN structure: a and c - lattice constants, b - bond length, $\alpha = \beta = 109.47^\circ$ - bond angles, $b'_1, b'_2, b'_3$ - three types of second nearest neighbour distances. Adapted from [11]	3
2.1. Equilibrium curve for GaN [12]	6
2.2. Ammonobasic [30] (a) and ammonoacidic [27] (b) growth setups	9
2.3. Na flux growth setup [35]	10
2.4. The reaction between $N_2$ and Ga, catalyst action of Na [36]	11
2.5. HVPE growth setup [27]	13
2.6. GaN bulk crystal grown by HVPE [56]	14
2.7. Scheme of the inductively heated reactor: (1) – position of seed, (2) – quartz vessel, (3) – seed-holder, (4) – ring shower, (5) – diaphragm, (6) – source crucible, (7) – graphite susceptor, (8) – graphite isolation felt [58]	15
2.8. Vapour pressure of Ga in function of temperature [59]	16
2.9. Polycrystalline GaN layer on the seed [60]	17
2.10. CVT grown single crystalline GaN layer, 160 $\mu\text{m}$ thick with C inclusions [60]	19
3.1. Breakdown electric field of air against pressure [101]	24
3.2. Temperature of plasma against pressure [102]	27
3.3. Energy levels of excited nitrogen and energy barrier for GaN synthesis [112]	31
3.4. Diatomic molecule - degrees of freedom	33
3.5. Quantum harmonic oscillator [123]	34
3.6. Rotational transitions [124]	35
3.7. Electronic, vibrational and rotational transitions [123]	35

3.8. Meaning of a) subscripts g/u, b) superscripts +/- and c) quantum numbers [125] . . . . .	36
3.9. Energy levels of nitrogen, based on [190] . . . . .	37
4.1. Schematic drawing of a typical PAMBE system [132] . . . . .	41
4.2. ECR plasma-assisted MOCVD system [138] . . . . .	42
4.3. MW plasma enhanced MOCVD setup [139] . . . . .	42
4.4. RPECVD setup [61] . . . . .	43
4.5. Modified MOCVD setup. Barrier discharge as a source of reactive nitrogen [141] . . . . .	44
4.6. Schematic drawing of the growth setup [142] . . . . .	44
4.7. a) Coplanar discharge in Si <sub>3</sub> N <sub>4</sub> (Si <sub>3</sub> N <sub>4</sub> becomes conductive at 1400 °C), b) DBD with Cu-wires in Al <sub>2</sub> O <sub>3</sub> at RT, c) Test structure after operation at 1100 °C . . . . .	47
4.8. DBD source mounted into the growth setup . . . . .	47
5.1. A - configuration nr 1, B - configuration nr 2 . . . . .	50
5.2. Main system components a) outside the reactor and b) inside the reactor	51
5.3. Growth setup . . . . .	54
5.4. Mo radiation shield . . . . .	55
5.5. Coil position y = 20 mm . . . . .	56
5.6. Height of the upper susceptor: a) 0 mm, T <sub>source</sub> = 1418 °C, b) 15 mm, T <sub>source</sub> = 1370 °C, c) 30 mm, T <sub>source</sub> = 1360 °C . . . . .	57
5.7. a) Coil position 50 mm, T <sub>source</sub> = 1175 °C, b) Coil position 100 mm, T <sub>source</sub> = 1070 °C . . . . .	58
5.8. Two-port network . . . . .	60
5.9. Electric field distribution in the resonant cavity . . . . .	61
5.10. a) cylindrical resonant cavity made of molybdenum foil, b) aluminium resonant cavity in operation at RT, p = 8 mbar . . . . .	62
5.11. Vapour pressure of refractory metals [159] . . . . .	63

5.12. Evaporation rates of refractory metals [159] . . . . .	64
5.13. $S_{11}$ parameter vs frequency . . . . .	65
5.14. Distances in the cavity . . . . .	65
5.15. Burning plasma in a Ti test-cavity, at 8 mbar . . . . .	67
5.16. The cross section of the auto-tuner. Stubs denoted as 1, 2, 3 are at absolute, mechanical zero position . . . . .	68
5.17. Thermal expansion coefficient for molybdenum and tungsten [162] . . . . .	69
5.18. Resonant frequency of the cavity vs $T_{source}$ . . . . .	71
5.19. $T_{seed}$ vs t. Plasma ignited in the cavity . . . . .	72
5.20. $T_{seed}$ vs t. Plasma started burning outside the cavity . . . . .	72
5.21. $T_{seed}$ vs t. After turning the induction heating off . . . . .	72
5.22. $T_{seed}$ vs t. Unstable plasma operation . . . . .	73
5.23. Ga source after 4 h growth experiment with: a) ammonia, b) microwave plasma . . . . .	74
5.24. Ga droplets in the Ga source . . . . .	75
5.25. Graphite susceptor a) attacked by $NH_3$ b) after microwave plasma enhan- ced experiment . . . . .	76
5.26. Ga loss vs $T_{source}$ . Nitrogen carrier gas flow set to 200 sccm [174] . . . . .	78
5.27. Ga loss vs $T_{source}$ for $p = 200$ mbar [172] . . . . .	79
5.28. Change of the Gibbs free energy vs radius of the droplet [176] . . . . .	80
5.29. Polycrystalline GaN grown on the $Al_2O_3$ seed . . . . .	82
5.30. Ga droplets on GaN template on $Al_2O_3$ . . . . .	82
5.31. Schematic growth window for sublimation sandwich technique [177] . . . . .	83
5.32. Ga droplets on the seed-holder because of plasma instability . . . . .	84
5.33. Parasitic deposition of GaN on the top flange . . . . .	84
5.34. OE spectrum recorded at RT, $p = 400$ mbar, MW power $\approx 400$ W, carrier gas flow = 0.1 slm $N_2$ . . . . .	86
5.35. OE spectrum recorded at a) $T_{source} = 1000$ °C and b) $T_{source} = 1200$ °C ( $p = 400$ mbar, MW power $\approx 400$ W, carrier gas flow = 0.1 slm $N_2$ ) . . . . .	86

5.36. Ga atom: a) electron configuration, b) energy levels . . . . .	87
5.37. OE spectrum recorded at a) RT, b) $T_{source} = 1200\text{ }^{\circ}\text{C}$ , $T_{seed} = 1000\text{ }^{\circ}\text{C}$ .	89
5.38. OE spectrum recorded at $T_{source} = 1100\text{ }^{\circ}\text{C}$ , $T_{flange} = 700\text{ }^{\circ}\text{C}$ (temp. of the flange covering the resonance cavity from the top) . . . . .	91
5.39. GaN crystallites . . . . .	94
5.40. The first version of seed-holder . . . . .	95
5.41. a) arc discharge, b) the operation of arcs as a function of pressure [98] . .	95
5.42. a) locally etched AlN template, b) decomposed GaN template . . . . .	96
5.43. Ta melted during the experiment: a) SEM picture, b) EDX scan . . . . .	97
5.44. Seed-holder . . . . .	97
5.45. Titanium cavity after few experiments . . . . .	98
5.46. GaN needles grown on a) $\text{Al}_2\text{O}_3$ and b) GaN template on $\text{Al}_2\text{O}_3$ . . . . .	99
5.47. GaN crystallites grown on AlGaN template . . . . .	99
5.48. Sample surfaces of GaN crystallites on sapphire grown with a) Ga excess b) and without visible Ga excess (SEM image). Both images were taken after etching the sample in $\text{HCl}:\text{H}_2\text{O}$ (1:2) . . . . .	103
5.49. Single crystalline GaN grown on sapphire . . . . .	103
5.50. SE image and EDS maps for gallium, nitrogen, aluminium, oxygen and carbon (incident electron energy of 5 keV) . . . . .	104
5.51. HRXRD rocking curve of GaN (0002), sample on sapphire . . . . .	105
5.52. GaN on GaN. GaN crystallites grown on GaN template: a) SEM picture, b) EDS maps. Incident electron energy of 5 keV . . . . .	105
5.53. Routes of GaN synthesis . . . . .	106
5.54. Plasma temperature, MW power $\approx 400\text{ W}$ [197] . . . . .	107
5.55. OE spectrum of nitrogen plasma and Ga vapour under growth conditions ( $T_s = 1300\text{ }^{\circ}\text{C}$ , $p_{N_2} = 400\text{ mbar}$ ), insert: violet system of CN molecule in higher resolution. Published in [208] . . . . .	108
5.56. OES recorded at RT, $p = 200\text{ mbar}$ , MW power: a) $\approx 280\text{ W}$ b) $\approx 345\text{ W}$ . Published in [208] . . . . .	110

5.57. OE spectrum recorded at RT, MW power  $\approx 400$  W, a)  $p = 200$  mbar b)  
     $p = 400$  mbar . . . . . 111

5.58. OE spectrum recorded at RT, MW power  $\approx 400$  W,  $p = 600$  mbar . . . . 111

5.59. C content in GaN layers grown by Na-flux: a [37] and b [212], PHVPE  
    [grown by our group in IKZ, not published], and MWVPE. Measured by  
    SIMS . . . . . 112





# List of Tables

1.	Properties of wurtzite GaN [9] . . . . .	3
2.	The gas-specific constants A and C of Townsend's first ionization coefficient. Valid in the range $C/2 \leq E/p \leq 3C$ [98] . . . . .	67
3.	Persistent lines of Ga [116] . . . . .	88
4.	Ceramics . . . . .	xiii
5.	Refractory metals [159, 162, 200, 215, 216] . . . . .	xiv
6.	Refractory metals [159, 162, 200, 215, 216] . . . . .	xiv
7.	Experiments described in the thesis - parameters . . . . .	xvii
8.	Second Positive System of N <sub>2</sub> , in the range of 280 - 450 nm . . . . .	xix



# List of symbols

$e$	electron charge	$1.602 \times 10^{-19} C$
$m_e$	mass of an electron	$9.109 \times 10^{-31} kg$
$A_{ki}$	Einstein coefficient for spontaneous emission	
$\alpha_{th}$	thermal conductivity	
$c$	speed of light	$2.998 \times 10^8 m s^{-1}$
$\delta_s$	skin depth	
$E_0$	electric field amplitude	
$E_b$	breakdown electric field	
$E_d$	interface distortion energy	
$E_{eff}$	effective electric field	
$E_{el}$	electronic energy	
$\tilde{E}$	root mean square electric field	
$E_{rot}$	rotational energy	
$E_{trans}$	translational energy	
$E_v$	evaporation energy	
$E_{vib}$	vibrational energy	
$\varepsilon$	emissivity	
$\varepsilon_0$	permittivity of vacuum	$8.854 \times 10^{-12} F m^{-1}$
$f_c$	cut-off frequency	
$f_r$	resonance frequency	
$G$	Gibbs free energy	
$\gamma$	secondary electron emission coefficient	
$\gamma$	change of the surface energy	
$\gamma_i$	surface energy of the interface	

## List of Symbols

---

$\gamma_L$	surface free energy of the layer	
$\gamma_S$	surface free energy of the substrate	
$h$	Planck constant	$6.626 \times 10^{-34} \text{ J s}$
$\hbar$	reduced Planck constant	
I	moment of inertia	
$J$	rotational quantum number	
$k_B$	Boltzmann constant	$1.381 \times 10^{-23} \text{ kg s}^{-2} \text{ K}^{-1}$
L	orbital angular momentum	
$\Lambda$	projection of the orbital angular momentum L along the internuclear axis	
$\lambda$	mean free path	
$\lambda'$	wavelength	
$\lambda_D$	Debye length	
$\Lambda_{dif}$	characteristic diffusion length	
$M_{Ga}$	molar mass of Ga	$69.72 \text{ g mol}^{-1}$
$M_N$	molar mass of N	$14.007 \text{ g mol}^{-1}$
$v_l$	molecular volume	
$\mu$	chemical potential	
$n$	density of charged particles	
$n_e$	electron density	
$n_g$	neutral particle density	
$n_{vib}$	vibrational quantum number	
$\omega$	angular frequency of the EM field	
$\omega_{osc}$	angular frequency of harmonic oscillator	
$\omega_{pe}$	plasma frequency	
$P_{abs}$	absorbed power	
R	universal gas constant	$8.314 \text{ J mol}^{-1} \text{ K}^{-1}$

$\rho$	density
$S$	total spin angular quantum number
$\sigma$	surface energy
$\sigma_c$	collision cross section
$\sigma_{VPE}^*$	relative supersaturation
$T_e$	temperature of electrons
$T_{flange}$	flange temperature
$T_g$	temperature of heavy particles in plasma
$T_i$	temperature describing translational energy distribution among charged species in plasma
$T_m$	melting temperature
$T_{rot}$	rotational temperature
$T_{seed}$	seed temperature
$T_{source}$	source temperature
$T_{vib}$	vibrational temperature
$\tau$	mean time between collisions
$\Theta$	wetting angle
$\nu_c$	electron-neutral collision frequency
$V$	volume
$V_b$	breakdown voltage
$x$	degree of ionization



# List of Abbreviations

1S-ELO	one-step epitaxial lateral over-growth
2DEG	two-dimensional electron gas
2S-ELO	two-step epitaxial lateral over-growth
CAN	controller area network
CBCF	carbon-bonded carbon fiber
CVD	chemical vapour deposition
CVT	chemical vapour transport
CW	continuous wave
DBD	dielectric barrier discharge
DC	direct current
DSP	double side polished
ECR	electron cyclotron resonance
EDX	energy-dispersive X-ray spectroscopy
EM	electromagnetic
EPD	etch pit density
FPS	first positive system of molecular nitrogen
FWHM	full width at half maximum

## *List of Abbreviations*

---

HEMT	high-electron-mobility transistor
HPSG	high pressure solution growth
HRXRD	high resolution X-ray diffraction
HT	high temperature
HVPE	halide vapour phase epitaxy
ICP	inductively coupled plasma
IKZ	Leibniz Institute for Crystal Growth
IR	infrared
LD	laser diode
LED	light-emitting diode
LT	low temperature
LTE	local thermal equilibrium
MBE	molecular beam epitaxy
MOCVD	metal organic chemical vapour de- position
MOVPE	metalorganic vapor phase epitaxy
MW	microwave
MWVPE	microwave plasma enhanced vapour phase epitaxy
NA	network analyzer
OES	optical emission spectroscopy



PA-MOVPE	plasma assisted metalorganic vapour phase epitaxy
PAEE	plasma-assisted electroepitaxy
PAMBE	plasma-assisted molecular beam epitaxy
pBN	pyrolytic boron nitride
PCAN	programmable controller area network
PHVPE	pseudohalide vapour phase epitaxy
PVT	physical vapour transport
RF	radio frequency
RHEED	reflection high energy electron diffraction
rms	root mean square
RPECVD	remote plasma enhanced chemical vapour deposition
RT	room temperature
SCAAT	Super Critical Acidic Ammonia Technology
SCoRA	Scalable Compact Rapid Ammonothermal
SEM	scanning electron microscopy
SIMS	secondary ion mass spectrometry
SPS	second positive system of molecular nitrogen
SSD	synthesis solute diffusion
SSM	sublimation sandwich method

SSN	sintered silicon nitride
TDD	threading dislocation density
TE	transverse electric
TMG	trimethylgallium
UV	ultraviolet
VIS	visual

# Acknowledgements

This work would not be possible without help from great number of people, to whom I would like to express my gratitude.

Prof. Dietmar Siche for supervising this thesis, his engagement, wisdom, time and patience while introducing me to the world of crystal growth.

Prof. Roberto Fornari and Prof. Matthias Bickermann for giving me the opportunity to work in the Leibniz Institute for Crystal Growth in Berlin and supporting my research.

Dr. Sebastian Golka for his constant support in every aspect of scientific work, priceless words of advice and sense of humour.

Dr. Alexander Vodopyanov for the fruitful cooperation, design of the MW plasma source and explaining peculiarities of MW plasma.

Dr. Andrei Pipa for his assistance in spectra analysis, calculating temperature of plasma and flawless collaboration.

Mr. Krzysztof Kachel and Mr. Mattia Capriotti for their problem solving attitude, optimism and thrilling lab meetings.

Mr. Reiner Nitschke, Mr. Gerd Schadow and Mr. Adrian Wagner for introducing me to all the deposition and vacuum equipment, and sharing their technical knowledge with me.

Dr. Daniela Gogova for making me familiar with the sublimation growth technique, SEM and EDX measurements. For her care and assist.

Mr. Albert Kwasniewski for performing HRXRD measurements.

Mr. Bernd Spotowitz, Mr. Uwe Kupfer and Mr. Kevin Reinhold for fast and accurate manufacture of the growth setup parts, their creativity and readiness to help.

Mr. Uwe Jendritzki and Ms. Petra Krause for design the growth setup and solving numerous technological problems.

Prof. Peter Sennikov for thought provoking discussions and ideas.

Dr. Jan Schmidtbauer for his assistance with LaTeX.

All the people, whose commitment and professionalism facilitated my every day work: Ms. Andrea Lepper, Ms. Birgit Ruthenberg, Dr. Maike Schröder, Ms. Elvira Thiede, Mr. Münter Friedemann, Dr. Carsten Hartmann, Mr. Sven Heron, Mr. Jens Klose, Mr. Uwe Rehse, Dr. Jürgen Wollweber, Mr. Mario Ziem.

Prof. Leszek Golonka for giving me the opportunity to gain my first international research experience and supervising my master's thesis.

Members of the First Berlin Toastmasters Club for their positive energy and contagious enthusiasm.

My Friends (especially Dr. Michele Baldini, Tomasz Fizia, Błażej Sadowski, Carmine Somma, Jakub Sukiennik) I can always count on.

My Parents and my Family for their unconditional love and continuous support.